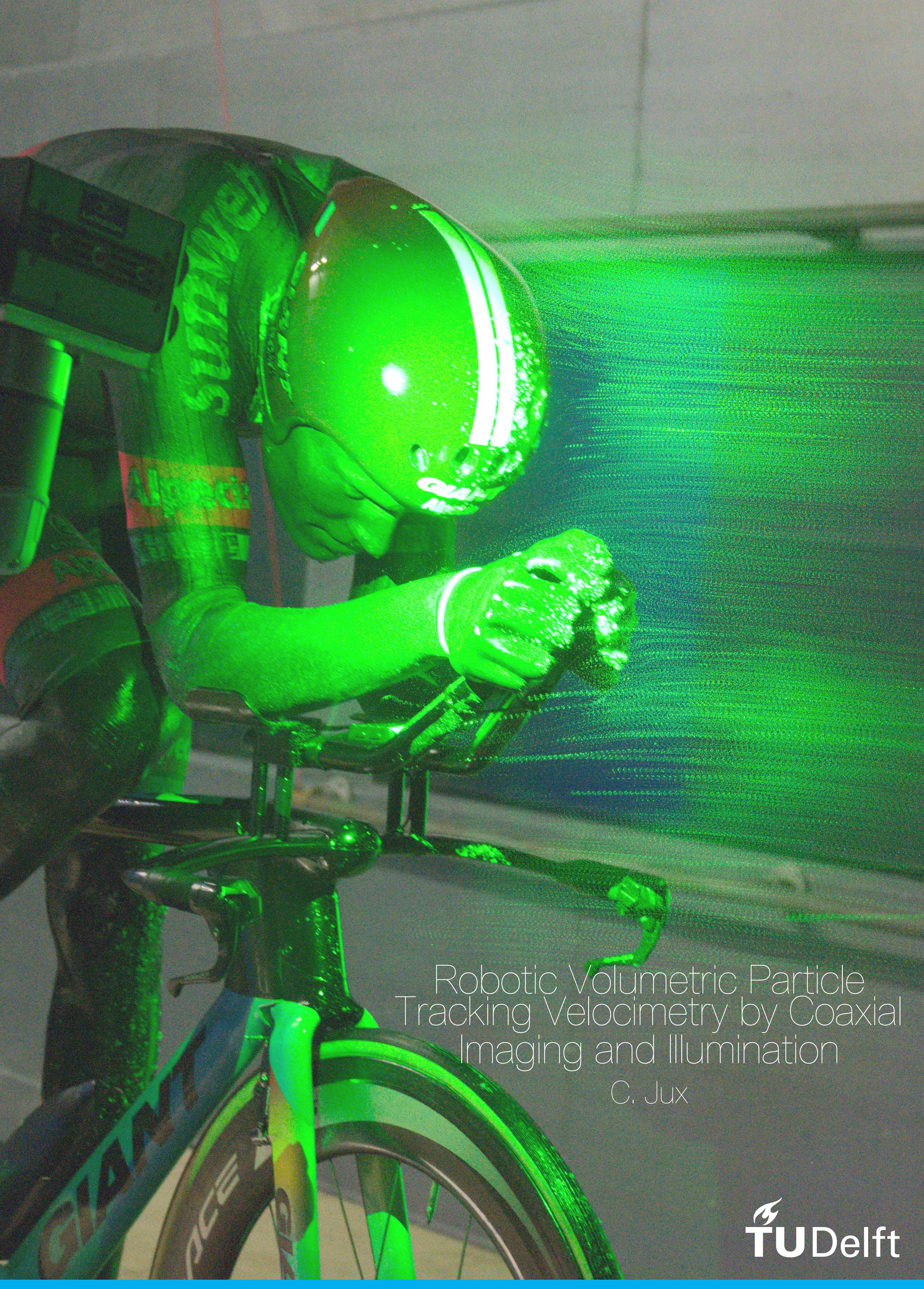

Robotic Volumetric Particle Tracking Velocimetry by Coaxial Imaging and Illumination

C. Jux

Robotic Volumetric Particle Tracking Velocimetry by Coaxial Imaging and Illumination

by

C. Jux

to obtain the degree of Master of Science
at the Delft University of Technology,
and the Technical University of Denmark,
to be defended on Wednesday July 5th, 2017 at 9:30 AM

Student number:	4160592	
Project duration:	November 1st, 2016 – July 5th, 2017	
Thesis committee:	Prof. Dr. F. Scarano	TU Delft, chair of assessment committee
	Dr. A. Sciacchitano	TU Delft, supervisor
	Ir. J. F. G. Schneiders	TU Delft, daily supervisor
	Dr. Ir. C. Simao Ferreira	TU Delft, committee member
	Dr. K. E. Meyer	DTU, supervisor

Preface

"Keep challenging"

The maxim of Team Sunweb, and at the same time a great catchphrase representing my personal ambitions throughout my studies and especially during my MSc thesis project presented in this work. Each of the overcome challenges during my studies and my graduation project contributed to my personal and professional development in its own way. Yet, as an individual you always need to rely on a strong supporting team to reach your targets and to keep challenging.

This thesis project provided the unique opportunity to challenge current limitations in flow measurement techniques, to develop cutting-edge technology and to apply it to the field of sports aerodynamics, thereby combining my studies with my personal interests. I am grateful for this opportunity, and I would like to thank Prof. Dr. Fulvio Scarano for letting me participate in this project. Further, I like to thank Bernd Wieneke and his colleagues at LaVision for the realisation of the project. Reaching our targets would not have been possible without the great support of Dr. Andrea Sciacchitano and Jan Schneiders either - thank you both for your contributions. Additionally, I would like to express my gratitude for the supervision of my project by Knud Erik Meyer on behalf of DTU.

Working successfully as a team, we shared some of the study's key findings at the *12th International Symposium on Particle Image Velocimetry* in Busan, Korea. I would like to thank Prof. Dr. Fulvio Scarano, Andrea Sciacchitano and Jan Schneiders for giving me the honour to present our work as well as for the inspiring discussions throughout the project and especially in the build up to the conference.

Next to the core team, I like to thank the colleagues in the aerodynamics department who have always been happy to help. Amongst these, I want to point out the role of Wouter Terra and Yash Shah who shared their experimental setup with us. Alexander Spoelstra and Andrea Rubino played an important role in manufacturing the seeding generator in time. Likewise, Beppe Caridi was never shy of providing his technical expertise when needed.

In the EWEM department I would like to mention Qasim Manzoor, Marcos Jerez Venegas and Nikolaos Frouzakis for their hospitality. Without your support I could not have completed my MSc project in the way I did - thank you for this great experience.

Furthermore, despite not being strictly related to this thesis project, a special thanks goes to Jasmijn Mansvelder, Ivar van Teeseling and Vincent van't Laar for tackling the challenges in designing and analysing composite structures together.

Lastly, and most importantly I would like to thank my family and friends for their continuous support. Thanks to my parents for letting me follow my dreams and for supporting me in all the challenges along the way. Thanks to my girlfriend for so many encouragements and for being there when most needed. I am further grateful for the personal advise, support and the trust received from my brother and my grand parents. Lots of colleagues have become close friends during the studies and you have enriched my experience in the past few years in your own and individual way. Thank you, Matthieu, David, Lukas, Arwin, Marco, Max and Max. And let us remind ourselves to keep challenging in the future.

C. Jux
Delft, July 2017

Abstract

A literature survey of particle image velocimetry applications in industrial facilities shows that there is a demand for large-scale and volumetric flow field measurements by the industry. Typical applications of interest include aeronautics with both, air- and rotor-craft flows, rotor aerodynamics including wind energy applications, the automotive industry encompassing motorsports as well as the flow around human athletes in sports aerodynamics. The turbulent nature of the described large-scale flows requires fully volumetric experimental techniques.

It is observed that most industrial studies exploit 2D PIV techniques however, with system components often mounted on traversing systems to slice a volume of interest by repeated 2D measurements. Two reasons are identified explaining the apparent preference for two-dimensional techniques: the achievable measurement volumes by tomographic PIV, which is considered the state-of-the-art volumetric PIV technique, are still relatively limited. At the same time, the complexity of a tomographic PIV configuration and the processing burden of tomographic reconstruction make the technique less suitable for large-scale industrial studies.

To address the identified need of large-scale volumetric flow field measurements, a novel robotic PIV system is proposed. The proposed configuration takes advantage of both, a newly introduced coaxial volumetric velocimetry probe and the light scattering efficient Helium Filled Soap Bubbles for particle tracing. The principles of coaxial volumetric velocimetry are studied theoretically and experimentally. It is shown that the low-aperture system features superior optical access as compared to classical PIV configurations. The compactness of the system yields high versatility and it gives rise to a universal system calibration, meaning that the studied velocimeter is well suited for robotic manipulations.

Albeit the application of HFSB tracers, the deep measurement volumes realised with the proposed CVV system do not exceed a size of $\mathcal{O}(25\,\mathrm{l})$. The size of individual measurement volumes is thus comparable to state-of-the-art tomographic PIV systems. To study larger domains the region of interest is partitioned and the time-averaged flow field is reconstructed from a multitude of PIV measurements. The proposed robotic PIV concept leverages the versatility of the introduced CVV probe and it presents an efficient approach to partition a desired measurement domain.

The feasibility of the proposed measurement concept is demonstrated in the flow field study of a time-trialling, full-scale cyclist replica of Dutch Olympic silver medallist and winner of the 2017 Giro d'Italia, Tom Dumoulin. 450 time-resolved volumetric PIV measurements are acquired, to compound the time-averaged flow field on a measurement domain of $2\,\mathrm{m}^3$ at $14\,\mathrm{m/s}$ freestream velocity. For swift processing of the PIV images the Lagrangian particle tracking algorithm 'Shake-the-Box' is employed. The individual measurements are combined by means of a purposely designed data stitching routine, yielding ensemble averaged data on a structured grid. The main flow features developing around the cyclist are briefly characterised, including stagnation and separation lines, shear layers, vortices, and the interaction of the observed structures.

The conducted flow field measurements highlight the feasibility of large-scale, quantitative and volumetric flow field measurements at the cubic meter scale by the application of the proposed robotic PIV method. In the current manual operation approach, subsequent measurements could be acquired at approximately two minute intervals. It is foreseen that the data acquisition process can be streamlined further yielding more efficient system operations, for instance by pre-programming observation positions or by the design of dedicated object scanning algorithms.

Contents

List of Tables

List of Figures

Nomenclature

α	Light-sheet-imager aperture	[°]
α	Roll angle	[°]
β	Pitch angle	[°]
β	Tomographic aperture angle	[°]
ΔX_{px}	Particle displacement in pixel units	[px]
δz	Focal depth	[mm]
Δ_p	Maximum search radius for particle pairing	[vox]
Δ_S	Shake delta in STB parameters	[px]
$\Delta_{\Delta_p abs}$	Maximum allowed absolute change in Δ_p	[vox]
$\Delta_{\Delta_p rel}$	Maximum allowed relative change in Δ_p	[%]
$\dot{N}$	HFSB production rate	[bubbles/s]
$\dot{V}$	Volume flow rate	[cm^3/s]
ϵ	Minimum acceptable fluctuation level for median filter	[m/s]
ϵ_u	Uncertainty of velocity u	[–]
ϵ_V	Freestream velocity deviation	[–]
ϵ_Δ	Triangulation error	[px]
γ	Yaw angle	[°]
λ	Light wavelength	[nm]
μ	Dynamic viscosity	[kg/(s·m)]
ν	Kinematic viscosity	[m^2/s]
ρ	Material density	[kg/m^3]
σ_u	Velocity standard deviation	[m/s]
σ_X	Positioning uncertainty	[mm]
τ	Autocorrelation coefficient	[–]
θ	Crank angle	[°]
$\vec{\omega}$	Vorticity vector	[s^{-1}]
$\vec{x}_t$	Robot arm tool-head translation	[mm]
$\vec{x}_{cor}$	Relative distance between origins of $\vec{x}_{rh}$ and $\vec{x}_c$	[mm]
$\vec{x}_c$	Camera (CVV) reference system	[–]
$\vec{x}_g$	Absolute reference frame	[–]

$\vec{x}_{Pb}$	Robot base position in absolute reference frame	[m]
$\vec{x}_{rh}$	Robot hand (tool head) reference system	[–]
a_i	Acceleration in direction i	[m/s^2]
A_n	Streamtube cross section fed by a single nozzle	[cm^2]
c_τ	Particle tracing ability constant	[–]
C_{HFSB}	HFSB seeding concentration	[bubbles/cm^3]
D_a	Aperture diameter, lens	[mm]
d_i	Image distance	[m]
d_o	Object distance	[m]
d_p	Particle diameter	[μm]
d_τ	Particle image diameter	[μm]
d_{def}	Particle image diameter due to defocussing	[mm]
d_{diff}	Particle image diameter due to diffraction	[mm]
d_{geo}	Geometric particle image diameter	[mm]
d_{i_n}	Nozzle pitch in direction i	[cm]
D_{ij}	Velocity gradient tensor	[s^{-1}]
DOF	Depth of field	[mm]
DSR	Dynamic spatial range	[–]
DVR	Dynamic velocity range	[–]
E	3D light intensity distribution	[counts]
f	Focal length	[mm]
f_I	Characteristic frequency, corresponding to T_I	[Hz]
$f_\#$	Relative aperture	[–]
$f_{I_{abs}}$	Absolute coefficient for weak intensity particle removal in STB parameters	[–]
$f_{I_{OTF}}$	Intensity factor for Optical Transfer Function	[–]
$f_{I_{rel}}$	Relative coefficient for weak intensity particle removal in STB parameters	[–]
$f_{r_{OTF}}$	Size factor for Optical Transfer Function scaling	[–]
hip_x	Hip location in x	[mm]
hip_y	Hip location in y	[mm]
HW	Hip width	[mm]
I	Light intensity	[W/m^2]
k	Coverage factor, normal distribution	[–]
L	Length scale, measurement domain	[m]
l_z	Length of reconstructed particle	[mm]

l_{min}	Minimum track length for STB particle tracks	[–]
l_{vox}	Characteristic voxel length	[mm]
M	Magnification factor	[–]
m	Polynomial fit order	[–]
m_{add}	Number of ‘add particles’ iterations in STB	[–]
m_{ref}	Number of ‘refine particles’ iterations in STB	[–]
N	Number of samples	[–]
n	Polynomial fit length	[–]
N_{eff}	Number of independent samples	[–]
P_b	Robot base location	[m]
Q	Second invariant of velocity gradient tensor	[–]
R	Sphere radius	[m]
r_0^*	Normalised residual for median filter	[–]
r_i	Residual for median filter	[m/s]
r_m	Median of residual for median filter	[m/s]
r_{thr}	Residual threshold, universal outlier detection	[–]
r_{vox}	Radius of close distance particle removal for overlapping particles in STB	[vox]
Re	Reynolds number	[–]
St	Strouhal number	[–]
SW	Shoulder width	[mm]
T_a	Acquisition period	[s]
T_I	Integral time scale	[s]
u	Velocity component along x-direction	[m/s]
u_i	Velocity vector	[m/s]
u_i'	Velocity fluctuation vector	[m/s]
u_{i_m}	Median velocity vector	[m/s]
U_{slip}	Slip velocity	[m/s]
v	Velocity component along y-direction	[m/s]
V_r	Radial velocity component	[m/s]
V_Φ	Tangential, out-of-plane velocity component	[m/s]
V_θ	Tangential, in-plane velocity component	[m/s]
w	Velocity component along z-direction	[m/s]
z_f	Focus plane location	[mm]
z_o	Object distance to focus plane	[mm]
z_{max}	Maximum attainable object distance for valid CVV measurement	[mm]
z_{min}	Minimum object distance for valid CVV measurement	[mm]

1

Introduction

Turbulence, a phenomenon reported by Leonardo da Vinci more than five hundred years ago and yet a subject that defines one of the well known, nonetheless unsolved, Millennium problems. It shows the complexity of its nature, which is inherently three-dimensional while involving wide ranges of temporal and spatial scales. At the same time, knowledge about turbulent flows can provide the foundation for performance gains in many engineering applications, ranging from noise emissions, over drag reductions up to heat transfer processes and many more. Boundary layers, from atmospheric to microscopic scale, vortex flows as generated on the tip of a finite wing, wake flows downstream of objects such as wind turbines, airplanes and athletes – turbulent flows are omnipresent, even in the limited scope of aerodynamics. Understandably, researchers are obsessed to study turbulent flows in all its manifestations.

Watching closely, the majority of flow examples listed above involve large-scale flows. Yet, despite the continuous increase in computational power, solving turbulent flows numerically is limited to relatively low Reynolds numbers, and thus, small objects and low speeds unless simplifying turbulence models are applied. This provides the necessity for quantitative experimental methods to investigate turbulent flows on large, industrial scales.

One of the most promising techniques in this aspect is Particle Image Velocimetry[1], an optical and therefore, non-intrusive flow field measurement technique. The principles of PIV and its modern day use in industrial wind tunnel facilities are reviewed in Chapter 2. This builds the foundation and motivation for the presented thesis project. Whilst PIV is a sophisticated, high-tech measurement technique, its key principles are understood by children: they throw a stick into a stream or they place a rubber duck in the bathtub and open the drain, to observe how the stick respectively the rubber duck are moving and thereby, assessing how the water is streaming. The application of tracer particles in fluid streams to quantify the fluid motion is understood. Instead of following tracers by eye, PIV is based on images recorded at a high repetition rate, from which the particle motion can be evoked. For a tracer to truly follow the flow however, Stokes drag law prescribes the use of extremely small, and ideally neutrally buoyant particles. The small tracers consequently require powerful light illumination, such that a high contrast image of the particles in the flow can be recorded. In fact, the strict illumination requirements remain one of the main limiting factors preventing industrial-scale PIV measurements, especially when considering three dimensional measurements which, as explained, are highly desirable for most engineering flow investigations.

Focusing on volumetric PIV, tomographic Particle Image Velocimetry as introduced by Elsinga et al. (2006) has developed to the state-of-the-art flow field measurement method. In its initial stages the fluid volumes which could be studied with tomographic PIV were still limited to the order of $\mathcal{O}\left(10\,\mathrm{cm}^3\right)$. The introduction of light scattering efficient Helium Filled Soap Bubbles[2] for wind tunnel applications by Scarano et al. (2015) however, caused a rapid expansion of the measurable volumes to the order of $\mathcal{O}\left(50\,\mathrm{l}\right)$ as the requirement for illumination intensity could be reduced by some orders of magnitude. A remaining limitation of tomographic PIV is its complexity, calling for a minimum of three cameras at

---

[1] hereafter referred to as PIV

[2] hereafter referred to as HFSB

large tomographic aperture while illumination shall ideally occur from a near perpendicular direction. This makes studies of flows around geometrically complex bodies particularly challenging as optical access is limited, whereas a rapid re-orientation of the measurement system is prohibited by a rather lengthy calibration procedure. Therefore, several attempts have been made to develop more simple and consequently more versatile volumetric PIV systems. The most prominent of these developments, as well as tomographic PIV, are discussed in more detail in Chapter 3 as these developments indicate the need for a compact volumetric velocimetry probe as studied in the presented work.

It can be argued that the scale of tomographic PIV with HFSB is still insufficient for many applications. This, together with the desire to measure flows also around complex bodies leads to the idea of partitioning the measurement domain into a set of adjacent fluid volumes. The individual data acquisitions may subsequently be merged together, allowing to resemble the time averaged flow field around the geometry of interest. The approach of partitioning a fluid domain is not new. Brücker (1995) already suggested to slice a 3D volume rapidly by a multitude of planar measurements in an attempt to gain 3D flow field data using PIV. Other researches (Lignarolo et al., 2014) have employed the idea of domain partitioning to study a turbine wake for several diameters downstream of a Horizontal Axis Wind Turbine[3]. One of the industry players, the *Intelligent Laser Applications GmbH*, has made an effort to offer an electronically controlled four-axis traversing system dedicated to PIV systems allowing for automated measurement campaigns (Intelligent Laser Applications GmbH, 2017). This idea is taken one step further, and the control of a compact volumetric velocimetry probe by a six degree of freedom robotic arm is proposed, referenced as a ‘robotic approach to large scale volumetric PIV’. Details on the compact velocimetry probe, which is driven by the principles of tomographic PIV, as well as the robotic manipulation are discussed in Chapter 4.

The desire to accomplish industrial scale volumetric PIV measurements, by partitioning of the fluid domain into adjacent volumes which can rapidly be scanned by utilisation of a robotic arm to control a novel coaxial velocimetry probe delivers the ingredients for the research objective of the presented master’s thesis:

> *“Assess the feasibility of quantitative, industrial scale, volumetric flow measurements, by characterising a robotic PIV approach based on a compact coaxial velocimetry system in a wind tunnel environment.”*

To successfully fulfil the research objective, a set of experimental campaigns is designed and executed. In detail, three main experiments are carried out, successively increasing the level of complexity towards a large-scale demonstration experiment which is presented in Chapters 6 and 7.

The large-scale demonstration features the near flow analysis on a full-scale replica of Dutch Olympic silver medallist and winner of the 100th edition of the Giro d’Italia Tom Dumoulin. This flow is deemed a suitable test case for the proposed PIV system, given that it features complex geometry with restricted optical access for the measurement system, it is on the cubic meter scale and it involves complex flow features including vortices of various scales as well as highly turbulent flow in the athlete’s wake.

The first two tests are instead designed to establish the working parameters and the interaction of the coaxial measurement system together with the robotic arm. Conclusions on the fundamental operational characteristics are reported in Chapter 4 which therefore, provides the groundwork for the following demonstration experiment.

In essence, the boundaries of the proposed robotic PIV measurement approach for large-scale complex flows are determined in this work. Therefore, it can be seen as the foundation for a novel measurement approach for industrial scale PIV studies. Bottlenecks are identified, conclusions on the feasibility of the proposed technique are drawn, and recommendations are given to further improve the application in Chapter 8.

---

[3] hereafter referred to as HAWT

2

Particle Velocimetry and its Applications in Industrial Wind Tunnels

Particle Image Velocimetry has become a mature flow measurement technology which has found its path into industrial applications. The basic principles as well as a brief historical review on key developments in PIV are discussed in the first part of this chapter. Section 2.2 then focuses on applications of the measurement technique in various industries, underlining the wide range of applications but more importantly, identifying the current limitations of the technology. This survey will ultimately provide a need for the development of the measurement system that is proposed in this thesis work.

2.1. Particle Image Velocimetry

Particle Image Velocimetry is a well known quantitative flow field measurement technique which was first explored in the late 1980s and has rapidly developed from a laboratory and research based measurement tool to an industrial scale measurement technique. In essence, the velocity field is determined by tracing of particle displacements in time. An analogy of the particle tracing principle, alluding to children observing floating objects in water, is given in the introduction of this thesis.

The dominant advantages of PIV over other techniques, such as Laser-Doppler anemometry and Hot-wire probes, are its non-intrusiveness as well as its potential to provide instantaneous and time-resolved field measurements rather than point measurements. The basic principles are briefly discussed in this section, alongside a schematic PIV setup sketched in Figure 2.1. Detailed aspects relevant for this thesis are elaborated in the subsequent chapters. For a detailed description of the specific working principles the reader is referred to literature, for instance the book by Raffel et al. (2007).

In its initial stages, PIV has been a planar (2D) technique measuring the in-plane velocity components (2C) in a thin light sheet from recordings of a single camera, as indicated in Figure 2.1. The light sheet is typically generated using a pulsed light source. The use of a laser[1] can be regarded as the standard, whereas recent research is exploring the applicability of LEDs[2] for illumination in PIV (Buchmann et al., 2012; Schanz et al., 2016b). Tracer particles in the flow scatter the light when passing the illuminated area. The scattered light can then be recorded by a Charge Coupled Device[3]. Evaluating the particle position at two subsequent time instances separated by a finite time, the instantaneous velocity is obtained as the fraction of particle displacement over time separation.

Adding a second camera to the system, resulting in a stereoscopic setup, all three velocity components can be measured in a plane. Utilising such planar systems to slice volumes in depth, scanning PIV provides 3D measurements by multiple planar samples (Brücker, 1995). The breakthrough to volumetric measurements can be seen in the development of tomographic PIV by Elsinga et al. (2006). Using three or more cameras the particle distribution in a volume is reconstructed from its two-dimensional images in a tomographic reconstruction problem, such that the motion analysis can be carried out in

---

[1] abbreviation used for ‘Light Amplification by Stimulated Emission of Radiation’

[2] abbreviation used for ‘Light-Emitting Diode’

[3] hereafter referred to as CCD

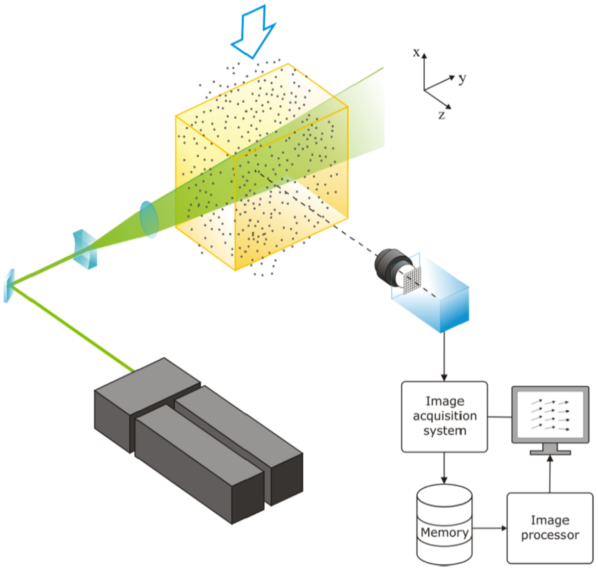

Figure 2.1: Sketch of generic planar PIV system, duplicated from (Scarano, 2013b).

a three-dimensional space. While tomographic PIV can be regarded as the state-of-the-art volumetric PIV technique, it still shows limitations in the maximum achievable measurement volumes, its required processing time as well as the complexity of the setup which in turn limits accessibility around complex geometries. These are the specific features addressed by the proposed robotic PIV approach.

2.1.1. Advances in PIV - Planar to 3D Time Resolved Measurements

The history of quantitative PIV spans three decades now, and as such several review articles can be found in literature. Adrian (2005) provides an overview on the first twenty years of PIV, which started as Laser Speckle Velocimetry[4]. Again, Raffel et al. (2007) points out several milestones in the development of PIV technology in his book. The early developments of volumetric PIV are captured in the review of Arroyo and Hinsch (2008), which also reflects on the initial stages of tomographic PIV as introduced by Elsinga et al. (2006).

The first reported modern PIV recordings date more than 30 years back. Several researchers applied Laser Speckle Velocimetry to measure the laminar flow in a tube, yielding a quantitative vector field representing the parabolic flow field (Barker and Fourney, 1977; Dudderar and Simpkins, 1977; Grousson and Mallick, 1977).

The technology was further studied at the von Karman institute, where Meynart (1983) accomplished first instantaneous turbulent flow investigations. In 1984 the term ‘Particle Image Velocimetry’ was established through the work of Adrian (1984) who recognised that for typical PIV recordings the source density in the images is insufficient to cause a speckle pattern, but instead individual particles are visible.

The next boost of the technology was accomplished by the introduction of digital imaging through Willert and Gharib (1991) as well as Westerweel (1993). This development allowed for much faster processing and thereby, for acquisition and analysis of significantly more data. In fact one can argue that the continuous increase of computational power, even nowadays, generally allows for acquisition of more data alongside increased processing speeds. At the same time, efforts are made to make the image data processing more efficient. A great example for the latter is the development of Lagrangian Particle Tracking algorithms for PIV images. This specific topic is addressed in more detail in Section 2.1.3 as it provides one of the necessities for acquisition and evaluation of PIV data on domains of several cubic meters in a timely manner.

A step in the dimensionality of the recordings was realised with the introduction of stereoscopic PIV which added the ability to measure the third velocity component in a thin light sheet. One of the early works in stereoscopic PIV is written by Arroyo and Greated (1991). Employing this technique on multiple

---

[4] hereafter referred to as LSV

light sheets forms the basis for scanning PIV, an early approach to realise volumetric measurements (Brücker, 1995). Some more details on this strategy are given in Section 3.1.

An alternative branch pushing towards volumetric measurements is found in holographic imaging, as described by Meng et al. (2004). The complexity and expense of a holographic PIV system however, did not allow its breakthrough towards volumetric velocimetry.

The latter was realised by the introduction of tomographic PIV through Elsinga et al. (2006). While this technology was initially still limited in the measurement volume due to the strict illumination requirements, the advent of Helium Filled Soap Bubbles for wind tunnel applications (Scarano et al., 2015) allowed for large-scale volumetric PIV measurements in air flows[5]. A discussion on requirements for tracer particles is presented in Section 2.1.2 as HFSB is considered one of the major developments allowing for the coaxial measurement system proposed in this work.

A very recent development on the processing technology was realised by Schanz et al. (2016a). This work establishes a reliable and highly efficient particle tracking algorithm, which enhances spatial resolution in time-resolved, volumetric recordings. More details on tomographic reconstruction and Lagrangian particle tracking are presented in Sections 2.1.3 and 4.1.5, respectively.

While this short review is by no means an extensive summary of the PIV history, it points out the milestones which led to the realisation of the proposed volumetric measurement system under investigation. In particular the introduction of tomographic PIV together with the scattering efficient HFSB tracers as well as the cost efficient Shake-the-Box particle tracking algorithm are key ingredients for the proposed coaxial volumetric measurement system. A more detailed review of alternative volumetric measurement approaches is presented in Chapter 3.

2.1.2. Tracer Particles

As indicated in Section 2.1, flow tracer particles are seeded in the flow of interest. The light scattering properties of the tracers allow to capture the instantaneous positions of the particles in a high contrast image. Evaluation of the change in particle position in subsequent particle images provides information about the particle motion in time. Generalising the particle motion to be indicative of the overall flow dynamics assumes that the disparity between fluid and tracer motion is negligible. For spherical particles in fluids, the ability to follow the flow is often evaluated in terms of the slip velocity, U_{slip} of the tracer, (Raffel et al., 2007).

$$U_{slip} = -\frac{d_p^2}{18}\frac{\left(\rho_p - \rho_f\right)}{\mu}\frac{dU}{dt} \tag{2.1}$$

Where ρ_p and ρ_f represent tracer particle and fluid density, respectively. It is important to note that the above equation is derived from the Stokes drag which assumes the particles motion is dominated by viscous forces and therefore, it is only valid for small particles. Given that the fluid acceleration $\frac{dU}{dt}$, and kinematic viscosity in terms of density ρ_f and dynamic viscosity μ are properties of the flow of interest, the remaining adjustable parameters are the particle size d_p, and the particle density ρ_p. Consequently, the slip velocity in Equation (2.1) can be minimised by selecting particles of minimum size, or by choosing neutrally buoyant tracers with particle density equivalent to the fluid density.

Intuitively, the tracer size will affect the scattering properties of the particles. The smaller the tracer, the less light will be scattered and vice versa. An in depth study of this subject was carried out by Melling (1997). For volumetric particle velocimetry applications where illumination intensity is critical (Scarano, 2013a), employing particles with small scattering cross section is not feasible. Instead, tracers with relatively large d_p but density equivalent to the fluid density are preferred in volumetric measurements.

For applications in air flows, Helium Filled Soap Bubbles have emerged as neutrally buoyant particles with both, great fluid mechanical properties to follow the air flow and sufficient size to provide great light scattering potential. To provide quantitative data, the response time of a nominal 300 µm diameter HFSB tracer is reported within $10-30$ µs by Scarano et al. (2015). The importance of scattering efficient tracer particles in the context of a coaxial imaging and illumination system cannot be stressed enough: Section 4.1.2 elaborates on the details of light scattering intensity as function of the object distance. This analysis creates evidence that HFSB is a keystone of coaxial volumetric velocimetry.

---

[5] The potential of HFSB as tracer particles for large scale PIV measurements in a closed volume, convective flow was demonstrated earlier by Bosbach et al. (2009).

2.1.3. Velocity Field Evaluation - Correlation versus Particle Based Approaches

Particle images provide the means to evaluate a velocity field of interest. A variety of methods is available to retrieve the velocity information from the recorded images. For volumetric PIV approaches, reconstruction of the 3D particle distribution from the 2D images is inevitable prior to the velocity field evaluation. Thus, the first part of this section focuses on available reconstruction methods. Once the particle distribution in space is obtained, the velocity field can be evaluated. This is the subject of the latter discussion in this section.

Volumetric Particle Reconstruction

Unless imaging with special cameras, such as plenoptic cameras (Section 3.6) or holographic imaging (Section 3.4), a conventional PIV camera records the light intensity distribution of a 3D volume in a planar, 2D image. This poses the problem of reconstructing the 3D intensity distribution from the 2D images. Algorithms designed for this particular exercise can be classified by two main properties: first, the final representation of the particles in space can either be particle- or voxel-based. In the former case, particle information is stored in terms of position and intensity only. In the latter case, the full reconstruction volume is discretised in an array of voxels. The resulting voxel array is then used to represent the light intensity and thereby, the particle distribution, in space. Second, a distinction is made between direct and iterative methods.

The most intuitive approach to particle reconstruction is perhaps the combination of 2D-particle detection in the images and the subsequent 3D-triangulation by intersection of the lines of sight. This method, which is often referred to as 3D-PTV, results in a direct computation of a particle distribution in space. Though, the success of the approach is strongly dependent on the allowed triangulation error ϵ_Δ. As the accepted triangulation error is increased, the triangulation procedure tends to produce more so called 'ghost particles', which later on prevent reliable particle tracking.

One of the most widely used methods in the initial stages of tomographic PIV was instead the Multiplicative Algebraic Reconstruction Technique[6] (Herman and Lent, 1976). The MART algorithm attempts to iteratively solve the tomographic reconstruction problem of finding the 3D intensity distribution E in the measurement volume as function of the 2D image intensities I. Since the described reconstruction problem is under determined, different initial conditions may converge to different solutions. Nonetheless, MART is know to work accurately at relatively high information densities, with typical particle image concentrations of up to 0.05 ppp (Wieneke, 2012). Thus, MART is typically used as a reference technique when new reconstruction methods are assessed, see for instance the comparison of particle reconstruction techniques by Michaelis et al. (2010).

A handicap of the iterative MART reconstruction is its computational burden. Several approaches have been presented that attempt to compute the volumetric intensity distribution directly instead. Worth and Nickels (2008) suggest an improved first guess of intensity distribution resulting in the so called Multiplicative First Guess[7] MART approach. A similar procedure is presented in the Multiplicative Line of Sight[8] method by Atkinson and Soria (2009). While such direct methods are computationally more efficient, they can suffer accuracy penalties as well as high ghost particle contents.

The remaining category covers the iterative particle based reconstruction approaches. The pioneering step in this branch was made by the introduction of the Iterative Particle Reconstruction[9] technique (Wieneke, 2012). In this approach, the 3D particle distribution obtained from particle triangulation is back projected onto the 2D images to compute residual images. Nonzero residual images then provide information about the actual particle position, thereby increasing accuracy. Furthermore, if a portion of particles is matched well, the information density in the residual images reduces whereby more particles can be reliably triangulated. Thus, the IPR algorithm yields more accurate 3D particle positions while being able to treat images with high information density. The latter aspect is key in PIV as high spatial resolution is obtained by dense seeding. The recent introduction of the Lagrangian particle tracking algorithm 'Shake the Box' (Schanz et al., 2016a), takes the concept of IPR one step further by predicting particle locations in a subsequent particle image through extrapolation of time resolved particle tracks.

---

[6] hereafter referred to as MART

[7] hereafter referred to as MFG

[8] hereafter referred to as MLOS

[9] hereafter referred to as IPR

It is worth pointing out that typical particle image densities, measured in the number of particles imaged per pixel (ppp), in volumetric PIV are on the order of $\mathcal{O}\,(1-5\%)$ (Scarano, 2013a; Wieneke, 2012). Consequently, tracer particle distribution in the measurement domain can be considered sparse. The advantage of particle based approaches over voxel based approaches is its storage of information in the particle locations only. The voxel discretisation instead yields significant content of cells that do not carry particle information and thus, it makes the reconstruction procedure computationally expensive.

Vector Field Evaluation

The volumetric particle reconstruction described above yields information on the spatial tracer distribution in each snapshot. Extracting information about the fluid motion requires analysis of image sequences. The type of analysis is typically classified in two branches: particle based approaches and correlation based methods.

Common in particle image velocimetry are correlation based velocity evaluation methods. The measurement domain is discretised into small interrogation volumes (windows in 2D PIV), such that $\mathcal{O}\,(10$ tracers) are contained in each interrogation volume, see Figure 2.2(a). For each volume a cross-correlation map is computed, indicating the best match of an interrogation window in the image taken at time t_i with the subsequent image at t_{i+1} (Figures 2.2(b) and 2.2(c)). The peak in the resulting correlation map indicates the most likely particle shift, and thus, it presents a measure of the mean motion within the interrogation volume. This process is illustrated in Figure 2.2 for a planar case.

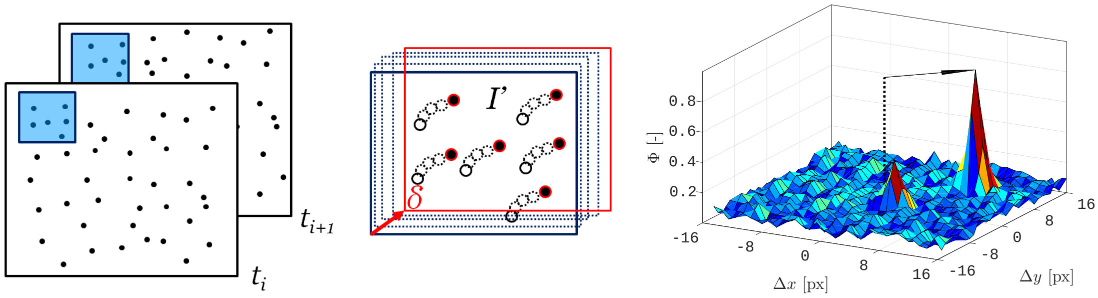

(a) Image pair with interrogation window

(b) Cross-correlation of interrogation window

(c) Correlation map with arrow indicating particle displacement

Figure 2.2: Illustration of a common cross-correlation analysis approach for planar PIV images.

The advantages of the correlation based evaluation approaches are manifold: reliable tracking can be guaranteed at relatively high particle image densities, yielding good spatial resolution. The resulting velocity vector field is well structured, making computations of gradients straight forward. The method is further easily adjusted from planar (pixel based) to volumetric (voxel based) correlation.

Yet, the requirement for multiple tracers in a single interrogation volume implies that data is spatially averaged, while the spatial resolution is also reduced. For maximum spatial resolution at a given particle image density, individual particle tracking is required instead.

Particle tracking methods on the other side are limited in the maximum information density as tracking reliability rapidly reduces with increasing particle image density. The previously outlined advances of both, IPR and STB algorithms, pushed the allowable seeding concentrations for volumetric PTV approaches to comparable levels of tomographic PIV. For a given tracer particle concentration, individual particle tracking yields higher spatial resolution and is thus beneficial.

Classically, pairing of particles in PTV was achieved by finding the nearest neighbour in two subsequent particle images and requiring the particle displacement to be smaller than the inter particle distance. Lagrangian particle tracking algorithms such as STB make use of the temporal information in time-resolved acquisitions to predict the subsequent particle locations. This allows tracking at higher seeding concentrations, while positional uncertainty can further be reduced by fitting particle tracks through the estimated particle locations. More details on Shake the Box are presented in Section 4.1.5.

A disadvantage of particle tracking approaches is however the resulting randomly distributed velocity data at the locations of the tracers. This complicates the evaluation of spatial gradients and thus, specific averaging and interpolation techniques are developed to map the sparse data onto structured grids. A recent work addressing this particular subject is presented by Agüera et al. (2016).

2.2. Industrial Scale Measurements

Section 2.1 highlights the working principles and the advances in PIV. Despite the technological developments over the past decades, PIV is still predominantly used in research laboratories and academia. Nonetheless, the application of PIV in industrial facilities is also broadly documented, as indicated by the selection of published measurements in Table 2.1. The collection of examples in Table 2.1 indicates that PIV measurements play an important role across various industries, such as the aerospace and wind energy industry which are often interested in rotor flows (Section 2.2.1), the automotive industry as detailed in Section 2.2.2 as well as the investigations into sports aerodynamics (Section 2.2.3).

Noticeably, the majority of studies listed in Table 2.1 consider stereoscopic or even planar PIV setups. Often, traversing systems are used to allow for multiple plane measurements. In some cases, such as the study by Wendt and Fürll (2001), multiple measurements are taken to combine results in a single plane which exceeds the attainable field of view of a single measurement. In other cases, for instance in the wake study of Nakagawa et al. (2015), several planes are scanned to gather knowledge in the third, the out-of-plane volume component.

It is no surprise that the PIV community feeds the industries demand by supplying sophisticated tools, such as automatic four-axis traversing systems (e.g. Intelligent Laser Applications GmbH). These type of tools allow for fast and sometimes automated repositioning of PIV cameras and illumination sources.

Perhaps it is more interesting to understand the industries apparent preference for multiple 2D measurements instead of a full volumetric approach. Two principle reasons can be identified and will be shown in more detail in the following subsections: first, the achievable measurement volumes with state-of-the-art tomographic PIV systems are still relatively limited. Secondly, the measurement system complexity and the data processing charge present obstacles in the deployment of tomographic PIV at industrial scale in its current form.

The survey of studies presented in this chapter goes to show that there is a strong desire for 3D measurement capability at industrial scales. Chapter 3 subsequently focuses on different attempts that have been realised to address this desire.

2.2.1. Rotor Flows

Rotor flows provide a great example for complex and highly turbulent flows and therefore, rotor flows remain a vivid topic of research. Typical applications are helicopters and propeller engines in the aerospace industry. Efficient lift and thrust generation at low noise levels are sought. Understanding the complexity of rotor aerodynamics helps reaching these goals.

More fitting are however wind engineering examples where kinetic energy is draught from the environment. Wind turbine wake studies provide knowledge for potential performance improvements of individual rotor designs. At the same time the industry shows interest in the interaction of wind turbine wakes in wind farms, given that smart positioning of the turbines can not only accelerate the energy yield of a farm, but it may also extend the anticipated lifetime of the turbines by reducing fatigue loads.

Two prominent industry examples of helicopter rotor wake studies by PIV are presented by the groups of Raffel et al. (2004) and Jenkins et al. (2009). Raffel et al. (2004) designed a stereoscopic PIV system to study a helicopter model with $4\,\mathrm{m}$ rotor diameter at the Large Low-speed Facility (LLF) of the German-Dutch Wind Tunnels (DNW). The impressive setup contained five digital PIV cameras as well as three double-pulsed Nd:YAG lasers, all mounted on large traversing systems, yielding a field of view of $360 \times 460\,\mathrm{mm}^2$.

The more recent work by Jenkins et al. (2009) achieved an even larger measurement domain of $\mathcal{O}\left(1\,\mathrm{m}^2\right)$ with the design of a large-scale stereoscopic PIV system at NASA. An illustration of the experimental setup is shown in Figure 2.3. Seeing the system complexity it is no surprise that the group specifically recommends to dedicate future resources towards a scanning capability of large-scale PIV systems given the time consuming process of system installation and calibration. Besides the faster data acquisition, such ability makes it simpler to capture flow features whose exact location is unknown prior to wind tunnel testing.

For wind energy applications a range of studies have been published recently at TU Delft. While these studies have been conducted at an academic research facility, present limitations of PIV in industrial scale wind engineering applications are highlighted. At the same time, potential applications of interest are demonstrated.

Table 2.1: Industrial scale PIV applications.

Industry	Reference	Setup	Facility	Scale
Aerospace	Aircraft half-model Pengel et al. (1997)	Planar	DNW (LLF) Marknesse (NL)	NA
	Aircraft half-model Coustols et al. (2004)	10 camera system with purpose built support	ONERA (B10) Lille (FR)	$1390 \times 920\,\mathrm{mm}^2$ $1.28\,\mathrm{m}^2$
	Rotor trailing vortices Raffel et al. (2004)	Stereoscopic 4-axis traverse	DNW (LLF) Marknesse (NL)	$460 \times 360\,\mathrm{mm}^2$ $0.17\,\mathrm{m}^2$
	Helicopter rotor wake Jenkins et al. (2009)	Stereoscopic	NASA (14×22) Langley (USA)	$1524 \times 914\,\mathrm{mm}^2$ $1.39\,\mathrm{m}^2$
	Coaxial jet flow, Noise prediction model validation Mead et al. (2015)	Stereoscopic Purpose made gantry traversing system	QinetiQ (NTF) Farnborough (GB)	$350 \times 200\,\mathrm{mm}^2$ $(10\times)\ 0.07\,\mathrm{m}^2$
Wind Energy	VAWT near wake Tescione et al. (2014)	Stereoscopic Traversing system	TU Delft (OJF) Delft (NL)	$350 \times 240\,\mathrm{mm}^2$ $(> 30\times)\ 0.08\,\mathrm{m}^2$
	HAWT near wake Lignarolo et al. (2014)	Stereoscopic Traversing system	TU Delft (OJF) Delft (NL)	$365 \times 430\,\mathrm{mm}^2$ $(> 30\times)\ 0.16\,\mathrm{m}^2$
	VAWT tip vortex Caridi et al. (2015)	Tomographic PIV HFSB tracers Static system	TU Delft (OJF) Delft (NL)	$0.4 \times 0.2 \times 0.2\,\mathrm{m}^3$ $0.02\,\mathrm{m}^3$
Automotive	Full-scale car model Wendt and Fürll (2001)	Stereoscopic In-plane traverse	Audi Ingolstadt (DE)	$540 \times 1600\,\mathrm{mm}^2$ $(3\times)\ 0.86\,\mathrm{m}^2$
	Full-scale car testing Cardano et al. (2008)	Stereoscopic Traversing system	Pininfarina Wind tunnel Turin (IT)	$\mathcal{O}\left(1\,\mathrm{m}^2\right)$
	25%-scale car wake Strangfeld et al. (2013)	Planar	TU Berlin Berlin (DE)	$425 \times 425\,\mathrm{mm}^2$ $0.18\,\mathrm{m}^2$
	28%-scale car wake Nakagawa et al. (2015)	Planar Light source on manual traverse	Toyota R&D Aichi (JPN)	$540 \times 405\,\mathrm{mm}^2$ $(16\times)\ 0.22\,\mathrm{m}^2$
	Full-scale car wake Casper et al. (2016)	Tomographic PIV HFSB tracers Static system	Volkswagen Wolfsburg (DE)	$2.0 \times 1.6 \times 0.2\,\mathrm{m}^3$ $0.64\,\mathrm{m}^3$
	General application in motorsports Toyota Motorsport GmbH (TMG)	Stereoscopic Traversing system	TMG Cologne (DE)	$350 \times 350\,\mathrm{mm}^2$ $0.12\,\mathrm{m}^2$
Sports	Full-scale cycling aerodynamics Flander's Bike Valley	Planar Traversing system	Flander's Bike Valley Beringen (BE)	NA
	Cycling helmet wake Chabroux et al. (2010)	Stereoscopic Traversing system	ISM wind tunnel University of Mediterranee Marseille (FR)	$320 \times 190\,\mathrm{mm}^2$ $(7\times)\ 0.06\,\mathrm{m}^2$
	Full-scale cyclist wake Terra et al. (2016a)	Tomographic PIV HFSB tracers Static system	TU Delft (OJF) Delft (NL)	$100 \times 170 \times 3\,\mathrm{cm}^3$ $0.05\,\mathrm{m}^3$

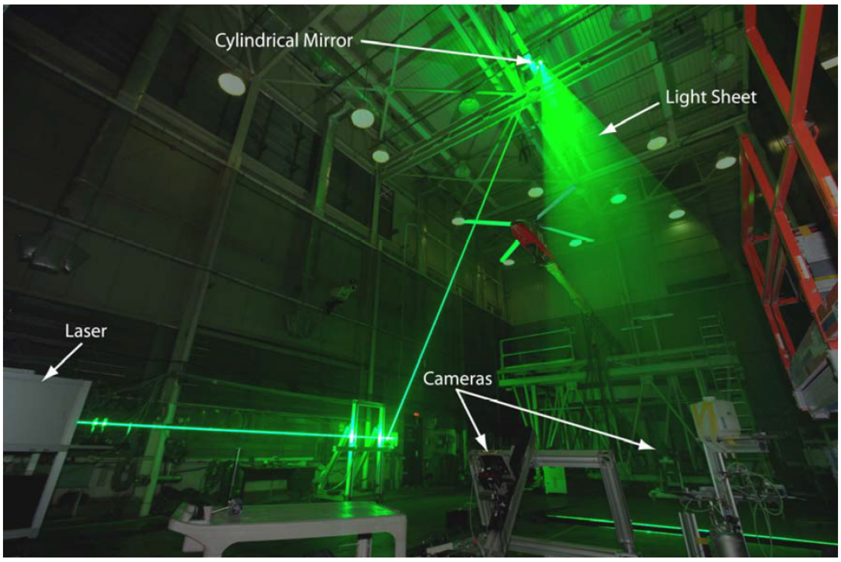

Figure 2.3: Experimental large-scale stereoscopic PIV setup developed by Jenkins et al. (2009). Shown setup is designed to carry out rotor wake studies of a hovering helicopter model.

Lignarolo et al. (2014) studied the wake of a 0.6 m diameter horizontal axis wind turbine, by a multitude of phase-locked stereoscopic PIV measurements. The wake study covers a domain of five rotor diameters downstream of the HAWT, which is obtained by merging of measurements with 0.35×0.24 m^2 field of view each. The measurement data is utilised to assess wake instabilities such as the tip-vortex breakdown and the consequences on the momentum recovery of the wake. An illustration of the specific measurement setup is shown in Figure 2.4.

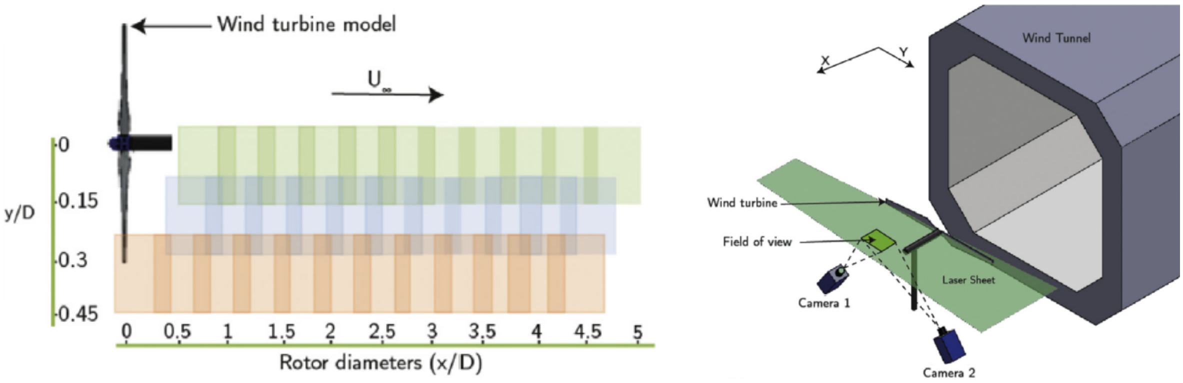

(a) Field of views of the phase-locked stereoscopic PIV measurements (b) Schematic of system arrangement

Figure 2.4: Illustration of measurement setup and resulting PIV measurement domain from Lignarolo et al. (2014).

A similar study on a vertical axis wind turbine[10] was presented by Tescione et al. (2014). Again, the field of view (300×400 mm^2) did not suffice to capture the full area of interest. As such, the group chose to pursue phase-locked measurements at the mid-span of the 1.0 m tall and 1.0 m diameter VAWT rotor model.

While both, Lignarolo et al. (2014) and Tescione et al. (2014) made use of conventional diethyl glycol based fog particles, the study carried out by Caridi et al. (2015) investigated the potential of Helium filled soap bubbles in tomographic PIV applications. The group of Caridi et al. (2015) used the same VAWT model as Tescione et al. (2014), focusing on the tip vortex characteristics in a $40 \times 20 \times 20$ cm^3 volume. The measurement setup is illustrated in Figure 2.5[11].

---

[10] hereafter referred to as VAWT

[11] A video of the operational measurement system can be found here: `https://www.youtube.com/watch?v=C0Nj8skn858`

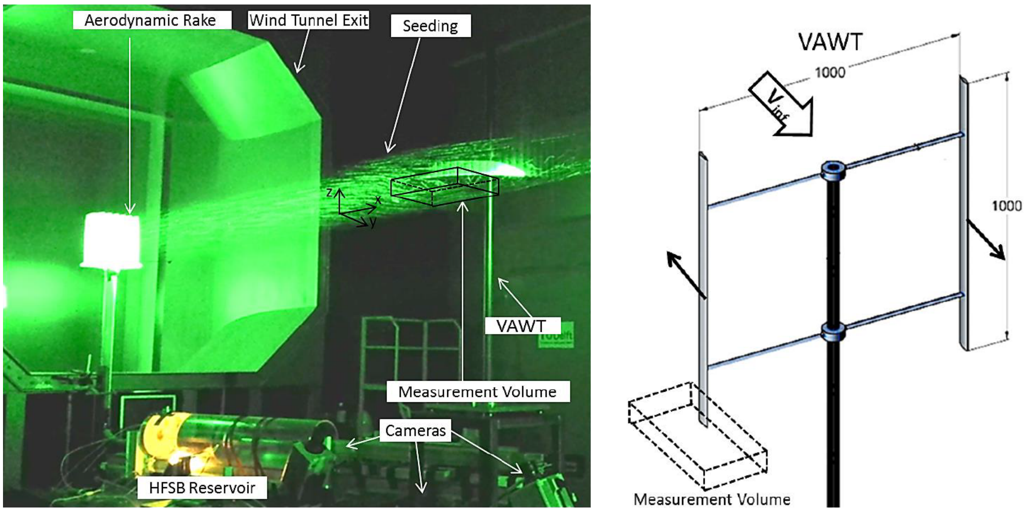

(a) Tomographic PIV setup

(b) VAWT model of the experiments carried out by Caridi et al. (2015) and Tescione et al. (2014)

Figure 2.5: Illustration of measurement setup and tomographic PIV measurement volume from Caridi et al. (2015).

The setup shown in Figure 2.5(a) highlights the current limitations of tomographic PIV measurements in wind tunnel environments. The complexity of the measurement system provides little flexibility. Yet, the achieved measurement domain of $16\,\mathrm{l}$ is small when compared to the scale of the wind turbine model.

The dilemma of researchers and engineers is recognised when comparing the studies of Lignarolo et al. (2014) and Tescione et al. (2014) to the work of Caridi et al. (2015). While the former groups opt for large observation areas, at the expense of the third volume component, Caridi et al. (2015) choose to study the full three-dimensional flow feature of the tip vortex in a rather confined measurement domain. This comparison shows that there is a need for large-scale volumetric PIV measurements, allowing to study complete aerodynamic structures at a reasonable scale.

2.2.2. Automotive Industry

Wind tunnel testing in the automotive industry is still very common. Drag reductions, noise emissions, aerodynamic stability and its effect on the vehicle dynamics are typical topics of interest. PIV is a tool of choice to gather knowledge on the flow features driving the individual characteristics. The studies listed in Table 2.1 indicate that there is a wish for large-scale volumetric PIV measurements in the automotive industry.

A general study of PIV applications and requirements for full-scale measurements in the car industry is presented by Cardano et al. (2008). The work is supported by experimental studies carried out at the Pininfarina Wind Tunnel facilities in Turin. Requirements which are identified are improved optical access, high spatial resolution for large observation volumes as well as ease of system handling for PIV equipment. Specifically, the ability of a system calibration outside the test-section is quoted as favourable, given the economical aspects of wind tunnel testing and the requirement of quick operations. These aspects are in-line with the motivation of the study presented in this thesis.

Some of these aspects are also recognised by Nakagawa et al. (2015). This work contains wake measurements on a 28% passenger car model at the research and development facilities of Toyota in Japan. The wake measurements are expected to provide insight on the aerodynamic stability and its effect on the vehicle dynamics, such as the steering response of the vehicle. The PIV setup comprises a stereoscopic system which can measure planes of $320 \times 320\,\mathrm{mm}^2$. The light source is supported on a manual traverse, such that multiple 2D measurements can be repeated at different height levels. Following this procedure, flow data is gathered in all three volume dimensions by composition of multiple planar measurements, indicating the wish for a fully volumetric measurement capability. Both, an illustration of the setup along with a qualitative representation of the results, are shown in Figure 2.6.

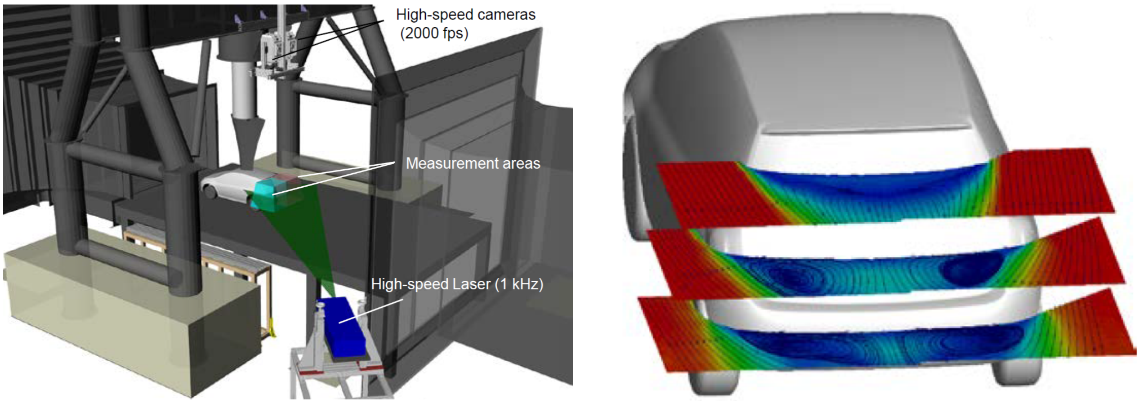

(a) Schematic of the experimental setup with the laser head on a manual traversing system

(b) Resulting velocity magnitude measurements in the wake of the car model

Figure 2.6: Illustration of measurement setup and corresponding results presented by Nakagawa et al. (2015).

Within the automotive industry, the motorsports sector shows perhaps an even stronger focus on aerodynamics. Despite missing publications, it is a well known secret that also PIV testing is common in motorsports. The Toyota Motorsports GmbH[12], which is currently running the aerodynamic development of Toyota's LMP1[13] contender and which was responsible for the Formula One chassis development of Toyota between 2002 and 2009, publish some limited information on their PIV testing procedures in the wind tunnel facilities in Cologne (Toyota Motorsport GmbH, 2017). It is evident that a traversable stereoscopic PIV system is installed (Figure 2.7), which shows once more the desire of volumetric flow field measurements that cannot be achieved at the desired scales. The illustration in Figure 2.7 further indicates that optical access can be critical for measurements e.g. close to the front suspension, between the front wheel and the chassis.

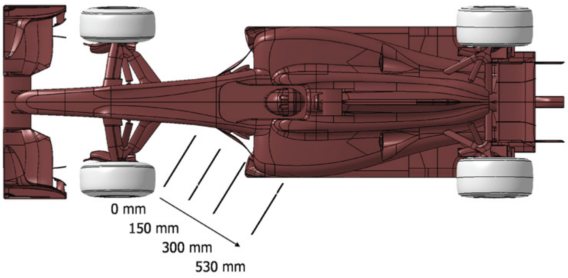

Figure 2.7: Illustration of typical PIV measurement planes in Formula One wind tunnel testing. Example shown is presented by Toyota Motorsport GmbH (2017). Scale wind tunnel models in Formula One are limited to a maximum of 60% of the full-size car and a velocity of 50 m/s.

A very recent study involving the application of tomographic PIV together with Helium Filled Soap Bubbles has been presented by Casper et al. (2016). In this demonstration LaVision indicated the potential of full-scale volumetric particle tracking velocimetry at the Volkswagen wind tunnel facilities in Wolfsburg. The measurements in the car wake captured a fluid domain of $2.0 \times 1.6 \times 0.2\,\mathrm{m}^3$ which is analysed using Lagrangian particle tracking. This study shows the advantages of light scattering efficient particles such as HFSB and the potential of large-scale measurements.

2.2.3. Sports Aerodynamics

Sports aerodynamics, and in specific 'speed sports', typically involve humans and the flow around athletes. May this be a runner, cyclist, speed-skater, skier, or any other sports athlete - all the samples involve airflows around the human body which are large-scale flows, that can hardly be studied in its full detail with conventional quantitative flow measurement techniques. Scaled tests eventually suffer from Reynolds effects, whereas full-scale tests are mostly limited to studies on local flow features.

An athlete's body can further be considered as a highly complex geometry. Attaining optical access to all regions of interest can prove to be difficult with conventional PIV configurations. The following samples are indicative for these observations, and they provide further motivation for the development of the proposed measurement approach. Note that all examples are referring to cycling aerodynamics,

---

[12] hereafter referred to as TMG

[13] abbreviation for 'Le Mans Prototype 1' category in the FIA world endurance championship

which are deemed suitable references for the demonstration experiment presented in Chapters 6 and 7.

Barry et al. (2014) acquired planar PIV data to investigate the aerodynamics of slipstreaming cyclists. Placing two full-scale cyclist models in a wind tunnel proved infeasible. Instead the group opted for scaled $1:7$ water channel measurements, at a Reynolds number which was an order of magnitude below the real case of a cyclist in air. This example indicates the need for systems that allow measurements at larger scales and thus, at realistic Reynolds numbers.

The group of Chabroux et al. (2010) opted for full-scale measurements instead, but limiting themselves to local stereoscopic PIV measurements in the helmet-wake of a time-trialling cyclist replica. The experimental setup of this study is shown in Figure 2.8.

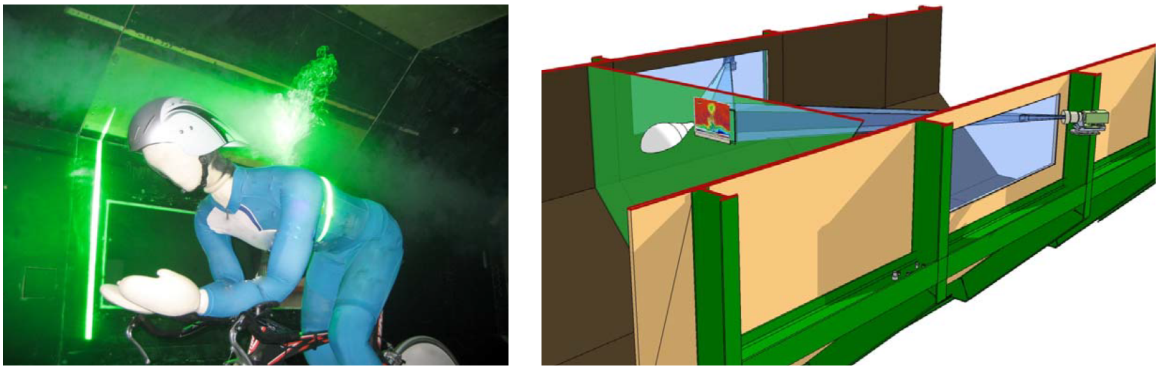

(a) Image of the test setup

(b) Schematic illustration of the system arrangement including sketch of measurement plane

Figure 2.8: Illustration of measurement setup presented by Chabroux et al. (2010).

Once more, the work presented by Chabroux et al. (2010) contains multiple planar measurements, offset by relatively small distances of 50 mm in the out-of-plane direction. It shows the desire of 3D PIV systems in the application to sports aerodynamics.

A significant advancement in the measurement volume was realised in the wake measurements presented by Terra et al. (2016a). By application of HFSB tracers the group of Terra managed to scan a 3 cm thick sheet spanning $1.0 \times 1.7\,\mathrm{m}^2$ downstream of a full-scale cyclist replica. The measurements presented in the referenced work are conducted at 4 m/s, however, the same group confirmed measurements at more realistic speeds of 50 km/h which will be published soon.

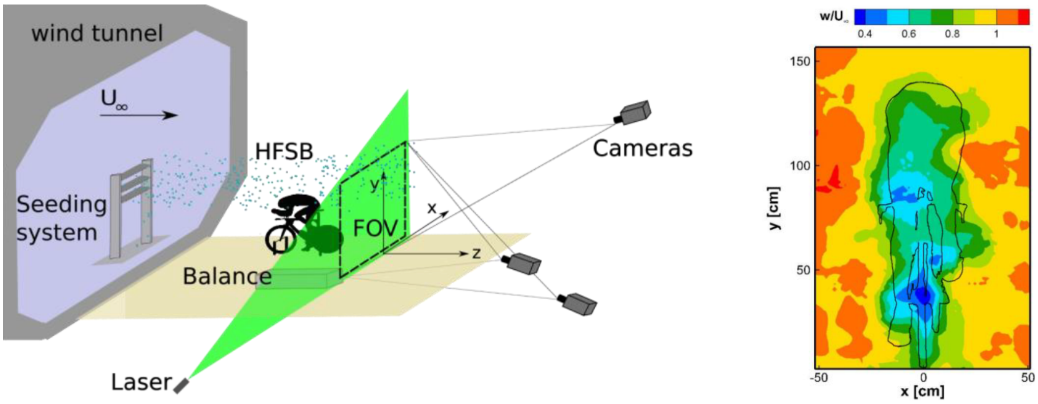

(a) Illustration of the test setup

(b) Wake measurements showing (normalised) streamwise velocity

Figure 2.9: Illustration of measurement setup and results presented by Terra et al. (2016a).

While the impressive three dimensional measurement domain stresses the advances of tomographic PIV, it still suffers some shortcomings: the test setup shown in Figure 2.9(a) is complicated, preventing fast readjustments of the measurement domain with respect to the model as well as optical access to near body regions close to the cyclist. Further, the results shown in Figure 2.9(b) are still composed of multiple individual PIV acquisitions, given that the full measurement domain cannot be seeded with sufficient HFSB concentration at the same time.

2.2.4. Other Applications

The previous examples present different applications of Particle Image Velocimetry across several industries. This survey is clearly not exhaustive, and many more examples can be found in other industries. This section pinpoints some recent studies which illustrate current capabilities and limitations of state-of-the art PIV measurements.

The work presented by Schanz et al. (2016b) considers the development towards large-scale PIV. Two experiments are contained in the work, both incorporating HFSB tracers as well as LED-illumination. Whereas the first experiment is conducted in a confined vessel with speeds $\ll 1$ m/s and therefore, it cannot be compared to wind tunnel experiments, its measurement volume of 550 l is beyond any current expectations of large-scale volumetric PIV. The second experiment, the recording of an impinging jet flow, is limited to 50 l only, but it is conducted at much higher speeds (16 m/s) and therefore, at higher Reynolds number. The examples in this study show the potential of large-scale tomographic PIV using Helium Filled Soap Bubbles. Yet, acquiring data in a confined vessel hides the challenge of attaining sufficient seeding concentration in such large volumes when applied in wind tunnel environments.

Another study that has been published in December 2016 is the analysis of the wake stability downstream of a frigate ship in a collaboration of the German-Dutch Wind Tunnels together with TU Delft (Rius Vidales, 2016). An illustration of the measurement setup as well as a sample wake visualisation are shown in Figure 2.10. The fluid volume scanned by tomographic PIV in this study spans $482 \times 168 \times 290\,\mathrm{mm}^3$.

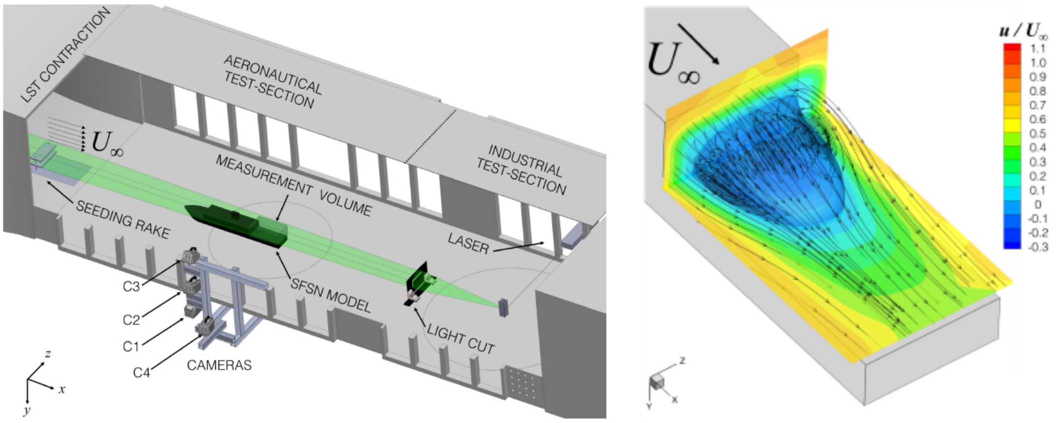

(a) Illustration of the test setup

(b) Sample result of the wake measurements showing (normalised) streamwise velocity

Figure 2.10: Illustration of measurement setup and results presented by Rius Vidales (2016).

3

Volumetric Particle Image Velocimetry Systems

Chapter 2 provides an overview of PIV applications at industrial scale. A wish for volumetric measurements can be derived, which is primarily addressed in the following sections. Furthermore, Chapter 2 indicates that for a range of applications the achievable measurement volumes remain insufficient. Consequently, a versatile and therefore, compact imaging system is desirable which allows for rapid partitioning of a fluid domain. As such, Sections 3.4 to 3.6 focus on single-camera, volumetric PIV systems that have been developed in the past. The review of the available methods and tools finally identifies shortcomings which are addressed by the proposed coaxial volumetric velocimetry system which is discussed in detail in Chapter 4.

3.1. Stereoscopic and Scanning PIV

The survey of large scale PIV studies in Section 2.2 contains a handful of examples where planar and stereoscopic measurements are repeated in several planes to gather flow data in the out-of-plane direction (Chabroux et al., 2010; Jenkins et al., 2009; Nakagawa et al., 2015). This is perhaps the most simple form of volumetric PIV, sometimes referred to as (2+1)D PIV.

This approach proves challenging when high temporal and spatial resolution are required. The distance between two subsequent measurement planes must be small for good spatial resolution, while the plane shift must occur fast if temporally resolved measurements are desired. Especially the latter requirement can yield complex setups in terms of imaging and particularly illumination. This explains why some studies, such as the presented example of Nakagawa et al. (2015) for instance, acquire time averaged data only allowing for timely separated measurements of individual planes.

The temporally resolved method featuring fast scanning was first introduced by Brücker (1995). In this study, the potential of the technique is demonstrated on a short finite cylinder in a water channel. The Reynolds number was however as low as 300, indicating the difficulty of achieving sufficiently quick plane shifts for acquisition of temporally resolved data for fast flows.

The technique suggested by Brücker has been used in several studies, such as for instance the analysis of a laminar separation bubble in the work of Burgmann et al. (2006). The study on a $20\,\mathrm{cm}$ chord airfoil in a water tunnel at Reynolds numbers of $20,000 - 60,000$ required ten individually controlled laser diodes to manage a temporally resolved acquisition. A schematic of Burgmann's setup and some qualitative results are indicated in Figure 3.1.

The group of Hoyer et al. (2005) adapted the scanning approach to 3D-PTV measurements, claiming that illumination requirements and particle image density limitations restrict the achievable spatial resolution in volumetric PTV measurements. Instead, the group suggests a rapid partitioning of the desired fluid domain, reducing illumination requirements while increasing the absolute seeding concentration in each partitioned volume. The setup of Hoyer et al. (2005) was however tailored to homogeneous turbulence measurements, at a full observation volume of $20 \times 20 \times 20\,\mathrm{mm}^3$. An extension of the technology to the desired industrial scales is questionable. Yet, the principle of domain partitioning is common with the proposed measurement approach in this thesis work.

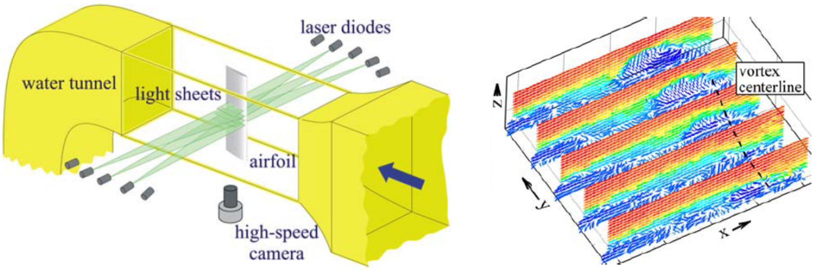

(a) Illustration of the test setup

(b) Sample result of vortical structures developing on the airfoil surface

Figure 3.1: Sample of scanning PIV on the suction surface of an airfoil with laminar separation bubble studied by Burgmann et al. (2006). Freestream along x, airfoil span along y.

3.2. Tomographic PIV

Tomographic PIV represents the current state-of-the-art volumetric PIV technique. PIV recordings of three or more cameras are treated with tomographic reconstruction algorithms (see discussion in Section 2.1.3) to obtain the tracer particle distribution in space. Evaluation of these reconstructions yields the velocity vector field in a 3D volume. The introduction of Helium Filled Soap Bubbles for wind tunnel applications (Scarano et al., 2015) pushed the maximum measurable volumes by tomographic PIV to $\mathcal{O}\,(50\,\mathrm{l})$. The technique is further suited for instantaneous measurements in high speed flows as well as for time resolved measurements at lower velocities.

A specific tomographic PIV setup was shown in Figure 2.5 in Section 2.2.1. Figure 3.2 shows a simplified schematic of a tomographic PIV configuration. Standard features are a powerful laser to guarantee sufficient illumination over the full measurement domain. Typically, measurements are conducted in a volume whose width and height are much greater than the volume depth. In such cases, cameras are arranged at a near-perpendicular observation angle with respect to the thick illumination volume. The tomographic aperture angles between the individual cameras are relatively large. Elsinga et al. (2006) recommend a tomographic aperture of $\mathcal{O}\,(30°)$, with excessive aperture angles promoting the appearance of ghost particles and lower tomographic aperture causing a loss of reconstruction accuracy in the depth direction.

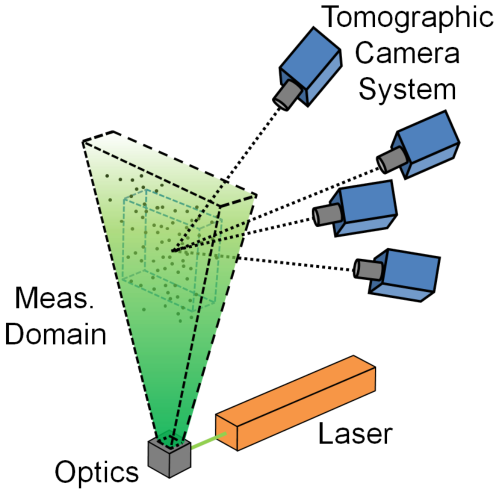

Figure 3.2: Schematic of a tomographic PIV setup. Orange body illustrates the light source, emitting light into an array of lenses and knife edge filters, yielding an expanding thick light sheet. Blue bodies illustrate cameras with grey objectives fitted and lines of sight indicated. The actual prismatic measurement volume is outlined within the illuminated region. Illustration replicated from Elsinga et al. (2006).

The effect of illumination direction and tomographic aperture on the observation domain is discussed in more detail: the study of complex flows often involves complex bodies. Yet, the effect of optical access can be illustrated with an object as simple as a sphere or a cylinder. Assuming a sphere is placed in the measurement domain of the tomographic PIV configuration shown in Figure 3.2, a shadowed region will occur as the light cannot pass the object. In this region, particles will not scatter light, and therefore, the shadowed region does not yield flow measurements. Furthermore, each camera will feature a blocked region behind the sphere, along its optical axis. Thus, also these regions are lost in the measurement field. This effect is illustrated in a simplified 2D drawing in Figure 3.3, which corresponds to a side view of the configuration shown in Figure 3.2.

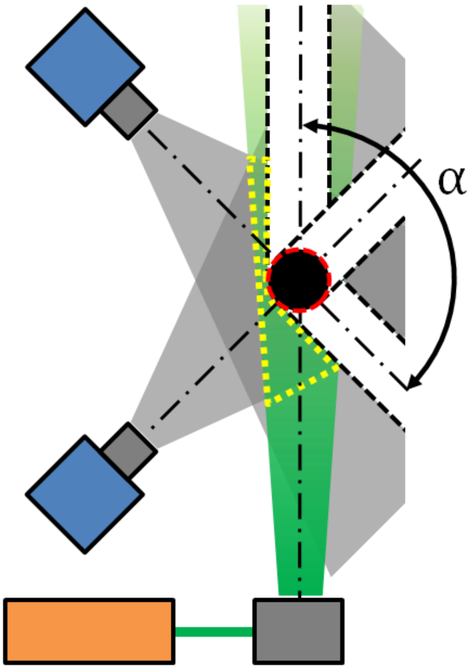

Figure 3.3: Side view of the tomographic setup in Figure 3.2 including a sphere as an object of interest to illustrate the concept of optical access for tomographic PIV.

In fact, for typical tomographic PIV configurations, the aperture spanned by the thick light sheet and the imaging system, indicated by α in Figure 3.3, corresponds to the extent of the region which does not possess sufficient optical access. The simple case shown here is used to illustrate this aspect. In more complex configurations, such as multiple bodies near each other, objects close to a wall, or for concave geometries, the effect can become even more pronounced. The proposed coaxial velocimeter minimises the indicated light-sheet-imager aperture (α), thereby maximising optical access. The specific case is discussed in detail in Chapter 4.

The range of examples for studies employing tomographic PIV given in Section 2.2 stress the capabilities of the technology (Caridi et al., 2015; Casper et al., 2016; Rius Vidales, 2016; Schanz et al., 2016b; Terra et al., 2016a). Significant fluid volumes can be analysed with high measurement accuracy. Yet, the complex measurement setup along with the strict calibration requirements for tomographic reconstruction limit the versatility of the method. In fact, system installation including both, geometrical and self-calibration (Soloff et al., 1997; Wieneke, 2008), can take up several hours. Therefore, partitioning of a larger measurement domain by several tomographic PIV acquisition is not feasible with the current state-of-the art configuration, but more compact systems are needed.

The latter aspect motivates the work presented in this thesis as well as the research and development carried out in the past to launch compact volumetric PIV systems. Some promising candidates are discussed in more detail in the following sections.

3.3. Volumetric 3-Component Velocimetry

Another multi-camera, volumetric flow measurement technique is the Volumetric 3-Component Velocimetry[1] system developed by TSI. The system relies on three cameras arranged in a triangular formation as shown in Figure 3.4(a). The overlay of simultaneously acquired particle images by the three cameras yields triplet patterns of the tracer particles. The triplet centre determines the in-plane location of a tracer particle, whereas the triplet size provides information about the depth location. Thus, a fully three-dimensional reconstruction of the particle locations in space can be obtained, giving rise to the application of 3D PTV algorithms in order to evaluate the velocity field of interest. The V3V™ velocimeter is shown alongside a schematic experimental setup of a jet flow study in Figure 3.4.

The compact system can record flows in a fluid volume of $14 \times 14 \times 10\,\mathrm{cm}^3$. The reconstruction accuracy of the in-plane position is reported with $20\,\mu\mathrm{m}$ by the manufacturer (TSI Incorporated, 2012), whereas the in-depth positioning is four times less accurate. Similar to tomographic PIV the system relies on perpendicular laser illumination as illustrated in Figure 3.4(b). Therefore, the optical access of the V3V™ system is constrained in a similar manner to tomographic PIV, given that the camera-light aperture is large.

The V3V™ system was first presented at the PIV conference 2007 in Rome. It was awarded as one of the 100 most relevant inventions at the *R&D 100 Award* in 2008 (R&D Magazine, 2010). Thus, it is not surprising that the system has been used in a range of flow studies since its introduction. Examples include the study of a turbulent flow in stirred tank reactors by Hill et al. (2008), the examination of vortex rings formed at inclined exits by Troolin and Longmire (2010) or the wake flow analysis of a miniature water turbine as presented by Chamorro et al. (2013) to name a few examples.

---

[1] also referred to as 'V3V™'

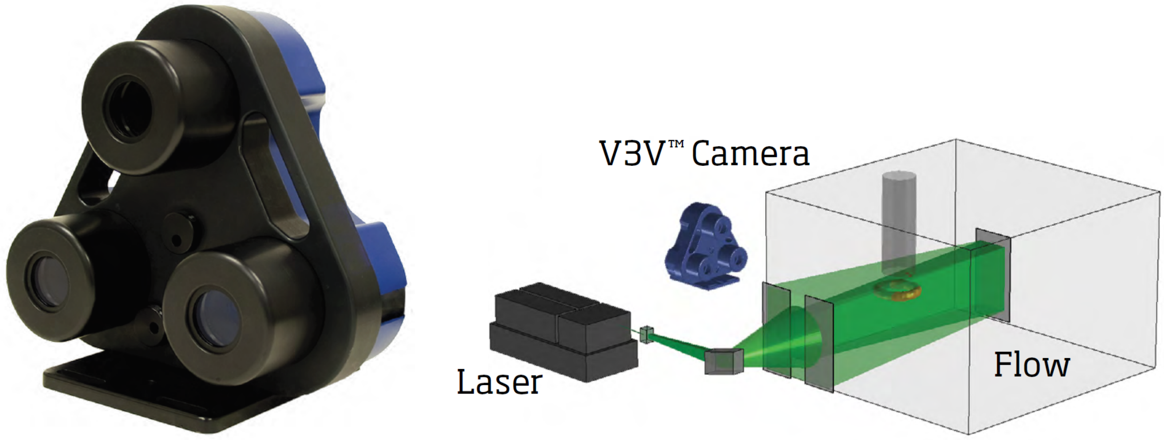

(a) V3V^{TM} camera (b) V3V^{TM} measurement setup

Figure 3.4: The V3V^{TM} system as developed by TSI. Illustrations duplicated from TSI Incorporated (2012).

3.4. In-line Holography

Holography is perhaps the first technology that comes to mind when aiming at 'volumetric imaging' with a single camera, given that a holograph contains the necessary information to locate an object in depth. Hinsch (2002) even describes holography as "the key to three dimensions in particle velocimetry" in his review article on holographic PIV. It is no surprise that researches attempted to make best use of this feature in order to develop volumetric PIV systems. One resulting development is the in-line holography, which in its concept, is close to the proposed coaxial velocimeter in the sense that both, imaging and illumination direction, are aligned as shown in Figure 3.5. Details on digital holography and in-line holography in particular are discussed by Meng et al. (2004).

The capability to record 3D3C particle images with a single digital holographic camera shows the power of holographic imaging. The compactness of the system reduces the setup complexity and thus, it benefits the handling of the components. Yet, a clear downside of holographic images is its limited information capacity and therefore, the constrained spatial resolution that can be achieved. Further, a typical problem of volumetric single-camera imaging systems is the in-depth resolution. This does apply to digital holography as well, as the depth of focus is relatively low.

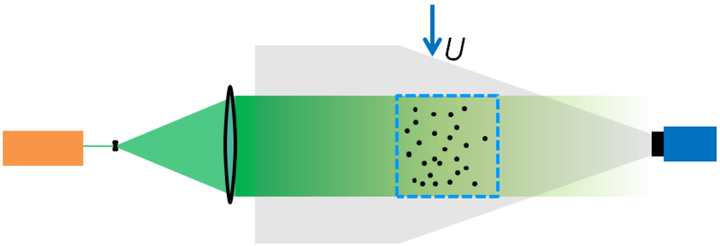

Figure 3.5: Schematic setup of in-line digital Holography. Light source in orange to the left, with optics to yield a beam expansion which is aligned by a converging lens. holographic camera (blue) opposite to the light source on the right. Measurement domain indicated in dashed blue.

The schematic setup of the in-line holography technique in Figure 3.5 considers the light source opposite to the camera. While this results in efficient forward scattering of light by the tracer particles, it strongly limits optical access for complex geometries, especially when considering concave shapes.

The study by Meng et al. (2004) contains some example measurements including results on a cylinder and a jet flow. The observation volumes are small with $\mathcal{O}\left(1\,\mathrm{cm}^3\right)$ and thus, these examples are not suited for the desired industrial scale measurements. This calls for alternative approaches, such as astigmatic and plenoptic PIV, both of which are discussed in the following.

3.5. Astigmatic PIV

Astigmatic PIV presents another single camera volumetric imaging technique. It uses the principle of optical aberrations that are caused if particles are imaged at a distance to the focus plane. Spherical particles take on ellipsoidal shapes, where the relation between semi-major and semi-minor axis length of the imaged particle provides information about the depth location of a tracer. The principles of astigmatic PIV are discussed in detail in the book of Hain et al. (2009).

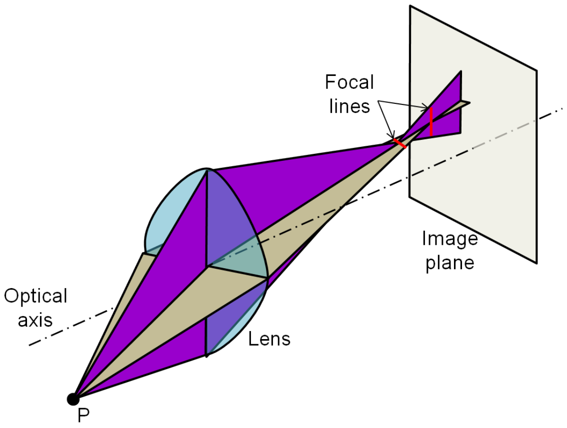

Figure 3.6: Illustration of astigmatic principle with a point *P* imaged off-axis through a lens causing optical aberrations and the formation of two orthogonal focal lines, yielding an ellipsoidal image of the point in the image plane.

The principle of astigmatism is comparable to optical aberrations caused by cylindrical lenses for instance. If a point in space, imaged through the lens, does not lie on the lens' optical axis the image plane will feature two orthogonal focal lines rather than a single focal point. The artefacts of these focal lines cause the point to be imaged as an ellipsoid. Astigmatic PIV applies the knowledge on the shape of these aberrations to obtain the point location in depth. The formation of the astigmatic aberrations is illustrated in a simplified sketch in Figure 3.6.

When the imaging technique is applied in PIV, thick sheet illumination at normal orientation to the imaging axis is suggested, common to planar PIV measurements. As argued before, this limits optical access around complex geometries. Further, the achieved in-depth uncertainties with astigmatic PIV recordings are relatively low while measurement depth is small.

Thus, astigmatic PIV presents another compact PIV system which improves system handling but which still shows weaknesses in terms of optical access, volume depth and measurement uncertainties, making it unsuitable for industrial scale PIV acquisitions in its current form.

3.6. Plenoptic PIV

Another single-camera volumetric imaging technique is presented by plenotic PIV. In plenoptic imaging both, spatial and angular distribution of light, are recorded yielding a four-dimensional light field (x, y, z, θ). Note, that a conventional camera records a 2D field only, given that the angular information of the light field is lost by integration. The higher dimensionality of the light field recording of plenoptic imaging allows to derive the 3D position of an object imaged with a plenoptic camera. Developments of plenoptic imaging dedicated to PIV measurements are presented by Thurow and Fahringer (2013).

The group of Thurow and Fahringer (2013) developed a plenoptic camera specifically dedicated to carry out 3D PIV measurements. Its functionality is demonstrated in an experimental campaign on a incompressible boundary layer flow with adverse pressure gradient at a free stream velocity of $15\,\mathrm{m/s}$. A fluid domain of $67 \times 39 \times 45\,\mathrm{mm}^3$ is analysed. As in conventional PIV configurations, illumination is provided by a laser in a thick light sheet, normal to the imaging axis.

Another experiment by the same group covers a supersonic jet flow, highlighting the potential of the technique also for high speed aerodynamics (Thurow and Fahringer, 2013).

More experiments employing the plenoptic imaging approach are presented by Fahringer et al. (2015). The vortex shedding on a 2D cylinder is studied in a $40 \times 27 \times 20\,\mathrm{mm}^3$ volume. Illustrations of the specific setup and sample results are shown in Figure 3.7.

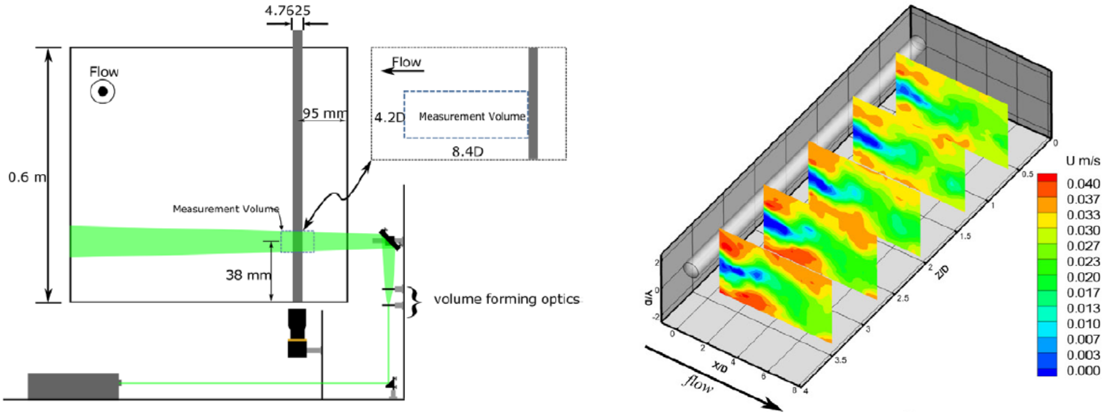

(a) Illustration of the test setup

(b) Fllow visualisation in the cylinder wake by streamwise velocity contours.

Figure 3.7: Schematic setup of plenoptic PIV measurement with a single camera, alongside results of a cylinder flow study by Fahringer et al. (2015).

The referenced studies prove that plenoptic imaging is a candidate for a compact volumetric PIV method. Yet, also plenoptic PIV has some inherent disadvantages, such as its spatial resolution which is traded for angular resolution and vice versa. As such the resulting spatial resolution in 3D is rather limited. To overcome this limitation La Foy and Vlachos (2013) suggest the application of multiple plenoptic cameras. This is however against the desire of a compact measurement system. Next to the resolution constraint, plenoptic imaging requires adaptation of existing tomographic reconstruction algorithms, yielding computationally expensive processing procedures.

3.7. Other Systems

The survey of the different volumetric PIV approaches in the previous sections highlights the challenges of realising a compact volumetric PIV system. It is argued that the need for such a system is the improved system handling as well as better optical access for flows around complex geometries. While these desires were derived for specific applications in the aerodynamics industry, other branches in the greater field of fluid dynamics are pursuing similar developments towards highly flexible, optical flow measurement devices. Some of these examples are briefly discussed in the following, demonstrating that certain features of the proposed measurement system are well suited to a wide range of applications.

An example for such a system is the portable tomographic PIV system for water flows presented by Adhikari et al. (2016). In the specific case the PIV system was designed to study delicate biological organisms (shelled Antarctoc pteropods) in water. The challenge is presented in the short survival times of the organisms in laboratory environments, requiring a measurement close to their natural habitat. The resulting design shown in Figure 3.8 appears as a conventional tomographic PIV configuration. However, the system fits into two standard golf bags and it can therefore be easily transported as flight baggage. As such, the work by Adhikari et al. (2016) stresses the desire for flexible PIV systems.

Another system was developed and demonstrated by Tritico et al. (2007). Similar to the previous study the PIV tool was developed for water applications. The resulting system was not only portable, but also submersible in water as demonstrated in a underwater PIV measurement in a river. The planar PIV system consists of two rigidly connected waterproof cases, one for each, camera and laser system. Therefore, the relative position of imaging and illumination system is fixed, even if the complete system is moved. The latter feature is one of the key aspects of the proposed compact velocimetry probe in this thesis work, given that a compact system can be moved as a whole eliminating the requirement for a recalibration.

While the two referenced examples are designed for very specific applications, they share the common goal of being versatile and rapid to use. This goes to show the common interests of PIV research across different fields of application.

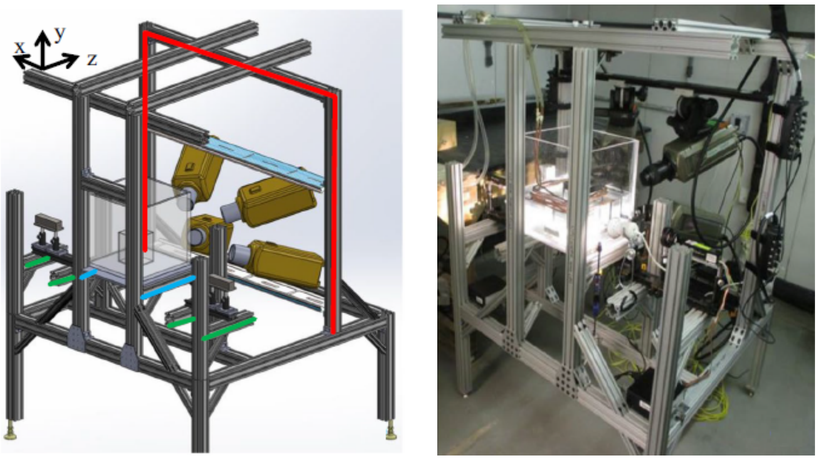

(a) CAD illustration (b) Operating system

Figure 3.8: Portable tomographic PIV system as designed and presented by Adhikari et al. (2016) for the study of organic shell structures in water.

The compact coaxial volumetric velocimeter proposed in this thesis, which in its principles is akin to tomographic PIV as presented in Section 3.2, is a different approach to the common goal. The working principles of the coaxial velocimetry approach are elaborated in the next chapter.

4

Coaxial Volumetric Velocimetry and Robotic Manipulation

The literature review in Chapters 2 and 3 identifies the wishes of the general aerodynamic industries for large-scale flow field measurements and the present limitations in the state-of-the-art particle image velocimetry techniques. The latter are particularly the limitation on the maximum measurable fluid volume of modern 3D PIV techniques, the complexity of the respective systems, and the resulting limited optical access. The Coaxial Volumetric Velocimetry[1] system proposed in this thesis addresses these shortcomings. A compact velocimetry probe based on the principles of coaxial imaging and illumination is characterised in this chapter. Its compactness makes it suitable for robotic applications, which is capitalised to design a robotic PIV approach ideal for partitioning of large fluid domains. The robotic manipulations discussed in Section 4.3 are the second key subject of this chapter. The discussion in this chapter is concluded with a performance assessment of the proposed robotic PIV system.

4.1. Principles

The basic principles of CVV are elaborated in this section. A schematic of the CVV system configuration is illustrated in Figure 4.1. While the working principle of CVV is akin to tomographic PIV (Section 3.2), the clear changes are the low tomographic aperture angles β, as well as the large depth of field. This creates unique imaging characteristics, such as strong variations in magnification and light scattering intensity in depth. These features are investigated in more detail in the subsequent sections, analysing how the system parameters will influence the performance of the PIV system.

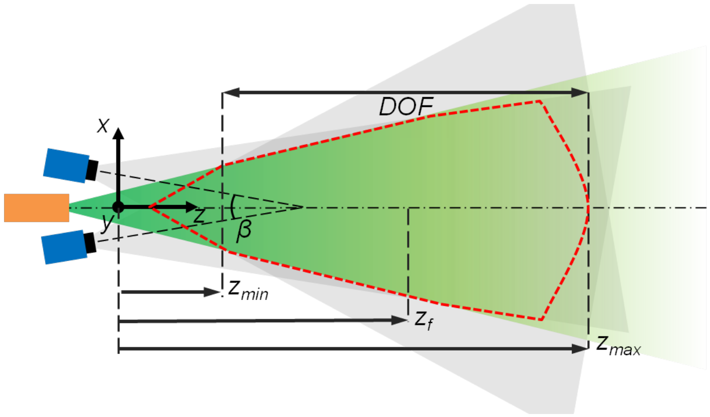

Figure 4.1: Schematic of the coaxial volumetric velocimetry setup, with light source (orange), tomographic cameras (blue) and low aperture lenses (black). Fields of view indicated in grey, whereas illumination volume is green. Measurement volume is outlined in dashed red.

---

[1] hereafter referred to as CVV

Analogous to the analysis of optical access for tomographic PIV in Section 3.2, a spherical object is imagined in the field of view of the sketched coaxial velocimetry configuration in Figure 4.1. The alignment of imaging and illumination direction results in a low tomographic aperture as well as a minimum angle between illumination and imaging direction, previously referenced to as α. Consequently, the shadowed, non-measurable fluid volume is minimised meaning that optical access is enhanced for the proposed configuration. This brief analysis is supported by the sketch in Figure 4.2.

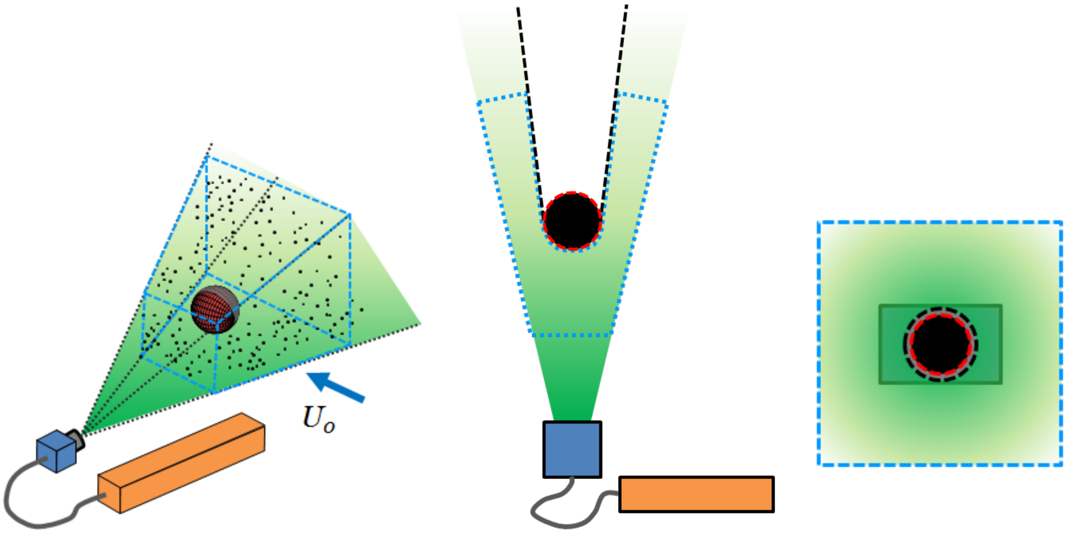

(a) Isometric view (b) Side view (c) Front view

Figure 4.2: Schematic of a coaxial volumetric velocimeter, imaging a spherical body.

Comparing the examples shown in Figures 3.3 and 4.2, it becomes evident that the proposed coaxial velocimetry system outperforms the conventional tomographic PIV configuration in terms of optical access. If the flow passing a geometrically complex body is studied, this means that the CVV configuration has the potential to capture the complete near body flow in less views as compared to a tomographic PIV system. The compactness of a CVV probe adds to the advantage over a classical tomographic imaging system, as the coaxial velocimeter can be handled easily, given that the imaging and illumination system are united in a compact body.

The novel imaging and illumination configuration of the CVV system results however in unique imaging characteristics, effecting the measurement performance. The dominant features are studied in more detail in the subsequent sections.

4.1.1. Imaging with Low Tomographic Aperture

As indicated in the introduction to this section, the CVV probe builds on a small tomographic aperture β. A simple geometric analysis illustrates that the in-depth accuracy in terms of particle positioning is limited by the low aperture. Following the theory outlined by Scarano (2013a), the in-depth uncertainty for such small angles is inversely proportional to the tomographic aperture β, given that the reconstructed particle shape elongates in depth as β is reduced as indicated in Figure 4.3.

The illustrations in Figures 4.3(a) and 4.3(b) assume that a particle is imaged in the CCD sensor centre. In this assumption, trigonometric relations show indeed that the depth of the reconstructed particle is inversely proportional to β for low aperture angles.

$$\tan(\beta) \approx \frac{d_p}{l_z} \quad \rightarrow \quad l_z \propto \frac{1}{\tan(\beta)} \tag{4.1}$$

Assuming instead that a particle is imaged along the edge of the CCD sensor as shown in Figure 4.3(c), the lines of sight are rotated by some magnitude θ which may be as large as the semi-angle spanning the cameras field of view. Consequently, the assumed diamond shape of the reconstructed particle indicated in Figure 4.3 rotates with the lines of sight. The effective depth of the reconstructed particle in the camera reference frame is the projection of l_z as determined in Equation (4.1) onto the

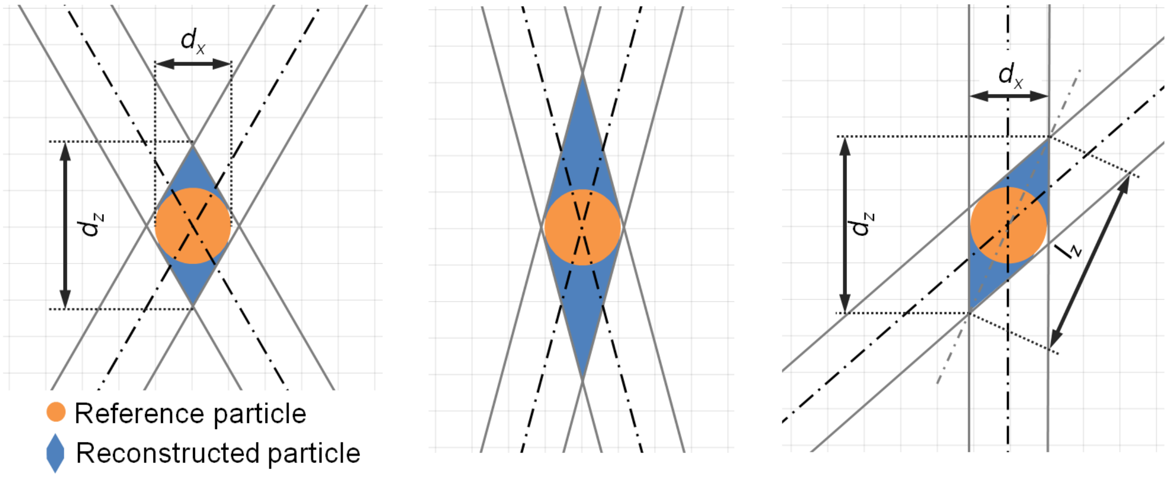

(a) $\beta = 60°$ (b) $\beta = 30°$ (c) $\beta \approx 60°, \theta \approx 25°$

Figure 4.3: The effect of tomographic aperture on the reconstructed particle shape, illustrating the elongation of a particle reconstruction with reduction in β. Figure reproduced from Scarano (2013a).

z-axis. Further assuming that the positional uncertainty in depth is proportional to the depth of the reconstructed particle shape, it follows that the accuracy in the depth-direction is improved if a particle is imaged away from the image centre.

4.1.2. Particle Imaging in Depth

The alignment of imaging and illumination direction allows for a large measurement depth as the illumination depth is only limited by the light source power. In a conventional tomographic PIV setup, the measurement volume is typically constrained by the depth of the (thick) light sheet, see Figure 3.2. Therefore, the variation of selected imaging parameters in depth is analysed in the following. These imaging quantities can subsequently be related to expected measurement uncertainties which characterise a specific PIV system.

Starting with the focal length of the camera lens f, this relates the image and object distance, d_i and d_o, respectively through the thin lens equation.

$$\frac{1}{f} = \frac{1}{d_i} + \frac{1}{d_o} \tag{4.2}$$

Where the ratio of image to object distance defines the magnification factor, M.

$$M = \frac{d_i}{d_o} \tag{4.3}$$

The image distance d_i is fixed for a specific combination of camera and lens. It is then seen that the magnification factor M is inversely proportional to the object distance and therefore, it attains large values close to the lens while it reduces with distance to the camera.

Intuitively, the magnification factor indicates how large a certain object is imaged on the sensor. Additionally to the geometrical particle image size, the actual particle image diameter is further determined by diffraction and defocussing effects (Olsen and Adrian, 2000).

$$d_\tau = \sqrt{d_{geo}^2 + d_{diff}^2 + d_{def}^2} = \sqrt{\left(M \cdot d_p\right)^2 + \left(2.44 \cdot \lambda \cdot f_\# \left(M + 1\right)\right)^2 + \left(\frac{M \cdot z \cdot D_a}{d_o + z_o}\right)^2} \tag{4.4}$$

Where the first square root term describes the geometrical particle image diameter, the second term evaluates the effects of diffraction and the third term accounts for defocused particles. In the case where the object distance is much larger than the image distance, the magnification factor in Equation (4.3) is small. Consequently, the geometric and defocussing terms in Equation (4.4) are small compared to the diffraction term. The particle image is said to be diffraction limited and the particle image diameter approaches a constant size of $2.44 \cdot f_{\#} \cdot \lambda$ as $M \rightarrow 0$. Note however, that close to the camera, the assumption of negligible magnification may not hold true and thus, particles imaged at short object distances will appear larger on the image sensor.

The actual depth in which an object is imaged in focus can be estimated by, (Raffel et al., 2007)

$$\delta z = 4.88 \cdot \lambda \cdot f_{\#}^{2} \left(\frac{M+1}{M} \right)^{2} \tag{4.5}$$

It is seen that the depth of field is increased as the magnification is reduced. Similarly a large $f_{\#}$ yields an increase in depth of field, at the cost of less light received by the CCD. Typically, it is recommended to chose the focal depth δz, such that it is greater than the thickness of the illuminated volume for the PIV measurements. Clearly, in the case of coaxial imaging and illumination this cannot be achieved as the illumination depth is practically infinite. Instead, this rule may be rephrased such that the seeded flow volume in depth shall be covered by the focal depth to ensure all tracer particles are in focus.

4.1.3. Measurement Uncertainty

The question that arises is how the above imaging quantities influence the ability to locate particles in the image accurately. Utilising the hypothesis of Adrian (1986) the accuracy at which a particle position can be determined depends on the size of the particle: The smaller the particle, the easier it is to find its centre. In this assumption, the error in the particle location can be expressed as a constant c_{τ}, which is specific to the imaging system, times the particle image diameter d_{τ}.

$$\sigma_{X} = c_{\tau} d_{\tau} \tag{4.6}$$

Recall, that for diffraction limited imaging the particle image diameter d_{τ} is approximately constant in depth. Subsequently, σ_{X} must be constant in depth. For velocimetry, the uncertainty in the velocity measurement is more insightful than the pure positional error. The velocity uncertainty can be estimated by the behaviour of the positional error relative to the particle displacement in one time step.

$$\sigma_{U} = \frac{\sigma_{X}}{\Delta X_{px}} \tag{4.7}$$

Due to the magnification effect an object displacement close to the lens will result in a larger displacement on the sensor, measured in pixel units, than the same physical displacement at a greater distance from the lens.

$$\Delta X_{px} \propto \frac{\Delta X_{0}}{z} \tag{4.8}$$

Substituting Equations (4.6) and (4.8) into Equation (4.7) it is seen that the uncertainty in the velocity measurement increases linearly with depth at a rate equivalent to the constant positional uncertainty.

$$\sigma_{U} \propto \sigma_{X} \cdot z = c_{\tau} d_{\tau} \cdot z \tag{4.9}$$

It is stressed that the observation in Equation (4.9) is only valid for diffraction limited imaging. Close to the lens, when the magnification is non-negligible any more, this assumption does not hold. Instead the particle image diameter d_{τ}, will be driven by the particle's geometrical size d_{geo}. In the latter case d_{τ} is inversely proportional in depth z and thus, the uncertainty in the velocity estimation is expected to be constant.

4.1.4. Illumination and Scattering

The discussion presented in Section 4.1.3 neglects the effects of particle light scattering properties and light intensities received by the CCD. Generally, the achievable light intensity in a volume is still considered one of the key limiting factors in realising large-scale volumetric PIV measurements. In the application of thick light sheets, the light intensity scales with the inverse of the desirable thickness for the same FOV (Scarano, 2013a).

For the coaxial system studied in this thesis a collimated light source is expanded using a spherical lens. The lens disperses the light into an expanding cone in which the light intensity is obeying the inverse-square law, as observed by (Adrian, 1991).

$$I \propto \frac{I_0}{r^2} \tag{4.10}$$

The inverse-square law is intuitively understood, considering that any energy emitted from a source is conserved while the illuminated area increases with the square of the cone radius. The latter grows linearly with the distance from the source, and thus, the proportionality in Equation (4.10) is obtained. A representation in terms of flux lines works well to visualise the effect, see Figure 4.4, where the count of flux vectors is proportional to the source strength and the density of flux lines is representative of the strength at a distance from the source.

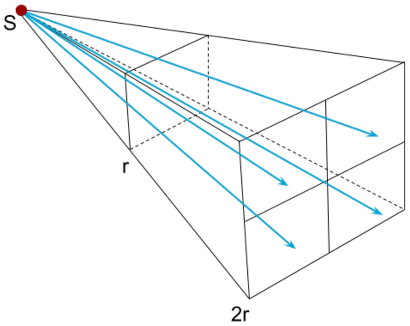

Figure 4.4: Illustration of the inverse-square law with flux vector density proportional to the local strength of illumination.

The previous discussion addresses the light emission from a source, which illuminates a measurement volume. The light received on the CCD sensors is the scattered light from the HFSB particles. Typically, light scattering of small particles is classified in three regimes: Rayleigh scattering for particles much smaller than the wavelength of light, Mie scattering for tracers whose size is on the same order as the light wavelength, and geometrical optics for particles which are significantly larger than the characteristic light wavelength. The characteristic length parameter used in literature is usually the circumference of the scattering cross-section πd_p (Melling, 1997).

Depending on the scattering regime, a particle scatters light with different intensities into all directions. For the present study, HFSB tracers with a nominal diameter of $300\,\mu$m are used as tracer particles. The wavelength of green light, as typically generated by lasers used in PIV, is on the order of $510\,$nm. Thus, the scattering of HFSB particles illuminated by green light is best characterised by geometrical optics. In this case, the inverse-square law in Equation (4.10) also applies to the light scattered by the particles which will be received by the CCD.

Pairing the two discussed contributions, it is expected that the light scattered by the particles will be received on the CCD sensor with intensity inversely proportional to the fourth power of particle distance to the lens. That is,

$$I_p \propto \left(\frac{I_0}{z^2}\right)^2 = \frac{I_0}{z^4} \tag{4.11}$$

This observation is confirmed experimentally as discussed in Section 4.4.

4.1.5. Lagrangian Particle Tracking - Shake the Box

The discussion of the CVV probe's low tomographic aperture angles in Section 4.1.1 concludes that the expected in-depth accuracy in particle positioning is relatively low. Lagrangian particle tracking can be a means to improve this accuracy by reconstruction of particle trajectories in time. In the assumption that the associated depth-error behaves randomly, the error can be reduced by fitting trajectories to the estimated particle locations. The principles of Lagrangian Particle Tracking, and specifically the Shake the Box[2] algorithm introduced by Schanz et al. (2016a) are discussed in this section.

Some of the main advantages of Lagrangian particle tracking are touched upon in the discussion on volume reconstruction from PIV images in Section 2.1.3. Particularly the superior computational

---

[2] hereafter referred to as STB

efficiency as well as higher spatial resolution which can be achieved through Lagrangian particle tracking are identified. An additional advantage is the exploitation of the temporal information to reduce random errors in the particle positioning. Though, it should be noted that also modifications of classical tomographic reconstruction algorithms have been developed that make use of temporal particle data. Examples to mention are Motion Tracking Enhanced MART[3] (Novara et al., 2010) as well as Fluid Trajectory Correlation[4] (Lynch and Scarano, 2013).

The advantage of Lagrangian particle tracking techniques is the utilisation of the temporal information, allowing for a prediction of the particle position in the subsequent image frame. This a priori knowledge of the tracer particle distribution is capitalised in the developed Shake the Box algorithm, and it allows for faster and more reliable particle tracking at comparably high seeding densities. The working principle of the STB algorithm is outlined in the following. For detailed information the reader is referred to the original research by Schanz et al. (2016a).

For the initialisation of the Lagrangian particle tracking method, no temporal information is available. As such, particle candidates are searched for using conventional particle tracking algorithms such as IPR (Section 2.1.3). This is repeated for a small number of time instances, typically four frames, in order to pair particle candidates which can form particle tracks. A simple pairing method can be a nearest neighbour search for instance.

Once initialised, the identified particle tracks are used to predict the new particle locations in the subsequent time step by extrapolation. Assuming continuity of particles in the images and a sufficiently small time step, the predicted location will be in close vicinity to the actual particle locations. A ‘shaking’ process minimises the local residuals to fit the actual particle positions. The conceptual idea of this optimisation procedure is presented in the work of Wieneke (2012). A schematic illustrating the general idea of using the residual information to improve the particle location is given in Figure 4.5.

The residual image after the shaking step contains untracked particles, which are likely to be new particles entering the imaged domain. These are tracked with standard identification algorithms as in the initialisation phase. The benefit of the prediction and shaking procedure is that the information density in the residual images is significantly lower as in the raw particle images. Thus, the STB algorithm is able to treat particle images with seeding concentrations in the same range as conventional, correlation based PIV algorithms. Moreover, the tracking of ghost particles is less likely given that their appearance is unlikely to correlate over multiple image frames such that ghosts make up complete tracks.

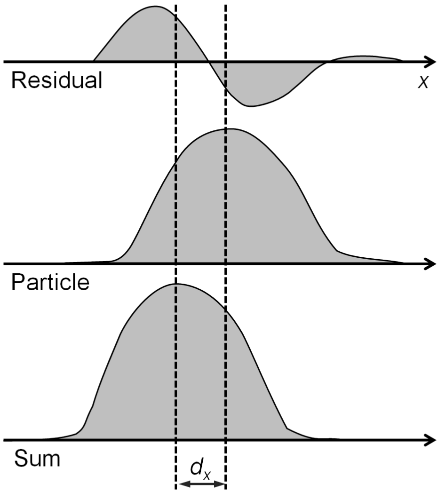

Figure 4.5: Concept of combining particle information with the residual image to approximate a new, more accurate particle position. Figure reproduced from Wieneke (2012).

The rough principle of the STB algorithm is outlined in a schematic of the tracking routine in Figure 4.6.

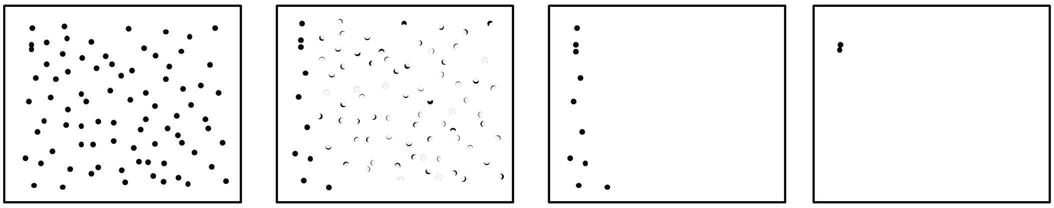

(a) Original image (b) Particle prediction (c) Post shaking (d) Post triangulation

Figure 4.6: Residual particle images in the sequential Shake the Box algorithm in its converged state. Graphic reproduced from Schanz et al. (2016a).

---

[3] hereafter referred to as MTE-MART

[4] hereafter referred to as FTC

4.2. Hardware

So far, the discussion is based on a theoretical PIV system. For all measurements presented in this work a prototype system supplied by LaVision is used. In the studies employing robotic control of the imaging system, a Universal Robots robotic arm is installed. Illumination is provided by a Quantronix Darwin Duo Nd:YLF high speed laser. These three systems are presented in the following. A description of the seeding system is given in the presentation of the experimental apparatus of the demonstration experiment in Chapter 6.

4.2.1. Coaxial Volumetric Velocimeter

The velocimetry probe comprises four *LaVision MiniShaker S* CMOS cameras in a prismatic body, with optical lenses protruding on the front face. An optical fibre runs through the probes centre, guiding the light to the front face where the camera lenses are mounted. A picture of the installed probe is shown in Figure 4.7.

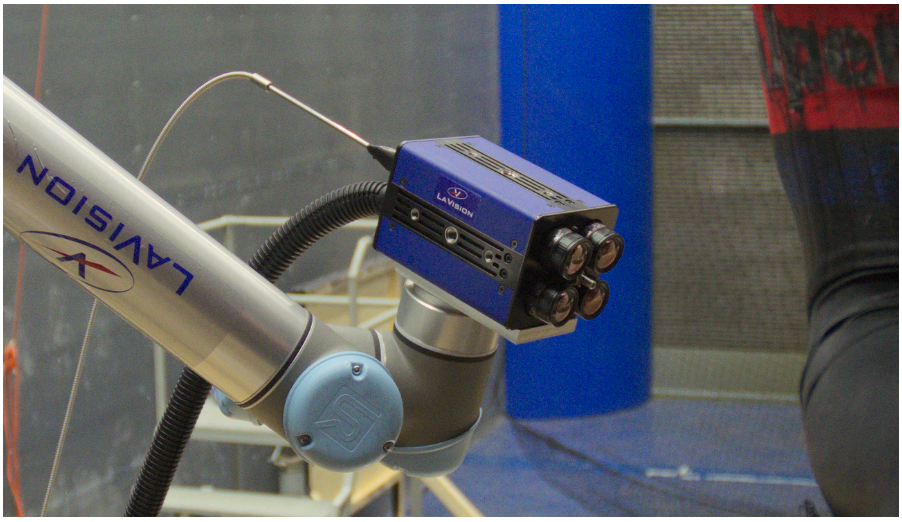

Figure 4.7: The coaxial volumetric velocimetry probe comprising four cameras and an optical fibre, mounted on a robotic arm.

The technical specifications of the velocimetry probe are tabulated in Table 4.1. More details on the illumination system are given in the subsequent section while Section 4.2.3 features the specifications of the robotic arm.

Table 4.1: Technical specifications of the coaxial volumetric velocimetry probe as shown in Figure 4.7.

	Parameter	Symbol	Value	Unit
Housing	Size	$w \times h \times d$	13×9×8	[cm^3]
Optics	Focal length	f_i	4	[mm]
	Relative aperture	$f_\#$	4–11	[–]
Imaging	Tomographic aperture at $z_0 = 40\,\mathrm{cm}$	β	4	[°]
	Sensor size	$S_x \times S_y$	800×600	[px^2]
	Pixel pitch	Δ_{px}	4.8	[µm]
	Bit depth	b	10	[bits]
	Acquisition frequency at full sensor	f	511	[Hz]
Illumination	Pulse energy	E_p	6.2–27.8	[mJ]
	Wavelength	λ	527	[nm]
	Spread angle	Φ	40	[°]

The data presented in Table 4.1 assumes that the full sensor is active. Reducing the number of active pixels allows for higher acquisition frequencies. It is further seen that the lens aperture is adjustable. For the combination of laser settings and optics used in the presented work, a value of $f_{\#} = 8$ is found to be a robust aperture setting suitable for most applications. The 10 bits cameras are powered via four separate `USB 3.0` cables which further manage the data readout.

Aerodynamic Interference Model

Unlike in classical PIV where the imaging system is at a far distance to the measurement volume, the CVV probe may instead be emerged in the flow field of interest posing queries on the intrusiveness of the system. Figure 4.1 indicates that there shall be a minimum distance z_{min} between the velocimeter and the measurement domain such that the perturbation of the flow is guaranteed to be below an acceptable level. To this end the CVV probe shown in Figure 4.7 is modelled as a sphere, such that a simple potential flow model can be considered to quantify the effect of the probe's presence on the passing airflow.

Seeking the 3D potential flow solution as a first approximation of aerodynamic interference provides justification for a minimum distance z_{min}. Defining a free stream V_∞ in spherical coordinates the unperturbed velocity field reads,

$$V_{r_0} = V_\infty \cos(\theta) \tag{4.12a}$$

$$V_{\theta_0} = -V_\infty \sin(\theta) \tag{4.12b}$$

$$V_{\Phi_0} = 0 \tag{4.12c}$$

Adding a doublet to simulate the flow around a sphere of radius R, the potential velocity field encompassing the sphere is described by,

$$V_r = V_\infty \left(1 - \frac{R^3}{r^3}\right) \cos(\theta) \tag{4.13a}$$

$$V_\theta = -V_\infty \left(1 + \frac{R^3}{2r^3}\right) \sin(\theta) \tag{4.13b}$$

$$V_\Phi = 0 \tag{4.13c}$$

Where r is the radial distance to the sphere centre. It is seen that the velocity deviation in the radial velocity component in Equation (4.13a) decays with r^{-3}, whereas the equivalent term in the tangential velocity in Equation (4.13b) is proportional to $0.5r^{-3}$. Thus, the maximum velocity deviation in the tangential velocity component V_θ is less extreme than the equivalent term in radial direction V_r.

To quantify the velocity deviation of the sphere, the norm of the perturbations is normalised by the magnitude of the free stream.

$$\epsilon_V = \frac{\sqrt{\left(V_r - V_{r_0}\right)^2 + \left(V_\theta - V_{\theta_0}\right)^2}}{V_\infty} \tag{4.14}$$

The above equation results in elliptical contours of induced velocity error ϵ_V. The semi major axis of these ellipses is aligned with the free stream, as shown in Figure 4.8. Assuming that the probe is not positioned directly upstream of the region of interest ($\theta \geq 0.5 \cdot \pi$), the velocity perturbation is least significant along the y-axis ($\theta = 0.5 \cdot \pi$). For a constant radial distance r, the error ϵ_V is consequently increasing with θ beyond $\theta = 0.5 \cdot \pi$.

A typical working range of the CVV probe spans $\frac{\pi}{2} \leq \theta \leq \frac{5\pi}{6}$. In the ideal scenario where the probe is aligned with the y-axis ($\theta = 0.5 \cdot \pi$), the velocity error ϵ_V stays within 1% for $r > 3.7\,R$. Likewise, in the opposite extreme of $\theta = \frac{5\pi}{6}$, the same error level is attained at a distance of $r = 4.5\,R$ only.

Based on the mean of the housing width, height and depth a sphere of 5 cm radius R is assumed to model the CVV probe at hand. Further assuming a working range of $\frac{\pi}{2} \leq \theta \leq \frac{5\pi}{6}$ as specified above, the minimum measurement distance to the probe noted by z_{min} shall be no smaller than 17.5 cm to keep the induced velocity error ϵ_V below 1%. The working range of the proposed coaxial velocimeter is established experimentally in the performance assessment in Section 4.4.

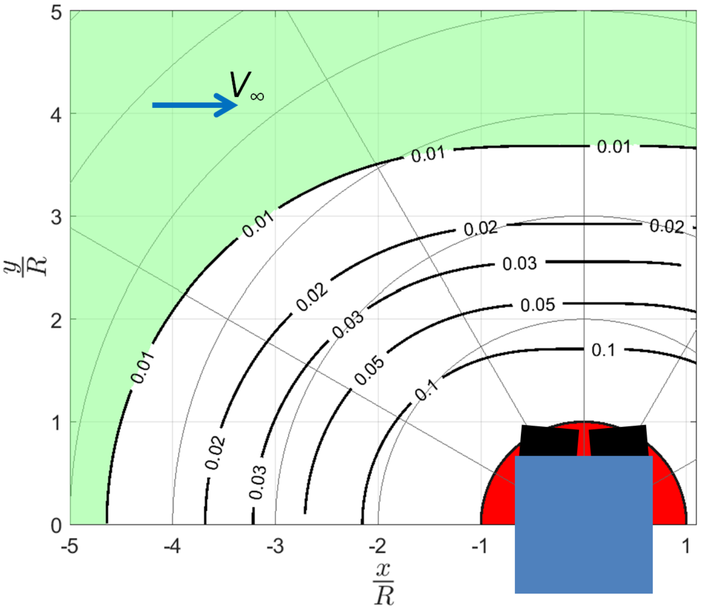

Figure 4.8: Contours of ϵ_V for the flow around a sphere of radius R, modelling the velocimetry probe shown in Figure 4.7. Green shaded regions indicate acceptable error level of $\epsilon_V \leq 1\%$.

4.2.2. Volume Illumination

The light source for all experiments presented in this work is provided by a Quantronix Darwin Duo Nd:YLF high speed laser. The laser is coupled with a spherical, converging lens of 20 mm focal lens to guide the light beam into a 4 m long optical fibre. At the fibre end another 4 mm spherical, expanding lens is attached to reach the desired light spreading angle.

The laser coupler is shown in Figure 4.9, whereas the integrated fibre in the velocimetry probe is presented in Figure 4.7. For operations with Helium Filled Soap Bubbles and acquisitions in time-resolved mode a pulse energy of $\mathcal{O}\,(20\,\text{mJ})$ with both laser cavities operating in parallel is found to be a robust configuration when the lens aperture is maintained at $f_\# = 8$ for all four cameras.

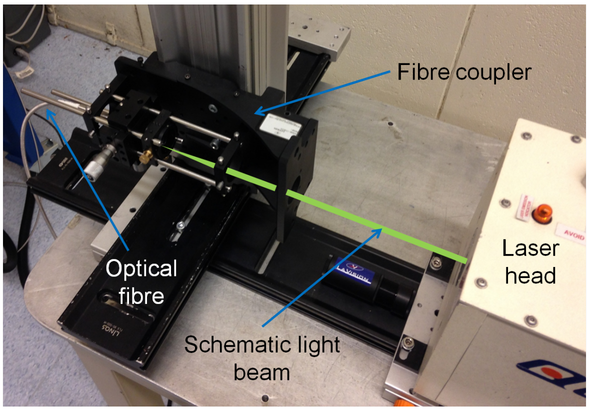

Figure 4.9: Coupling of optical fibre to laser head.

4.2.3. Robot Arm Specifications

In the large-scale experiments the velocimetry probe's position and orientation is controlled using the *Universal Robots - UR5* robotic arm. The arm has a maximum reach of 85 cm radius around its base. The six joints of the robotic arm provide six degrees of freedom, namely three translations as well as three rotations. The joints of the robotic arm allow for similar motions as in the case of a human arm. An illustration of the arm with indications of its range and degrees of freedom is given in Figure 4.10.

Referring to Figure 4.10, two joints can control a yawing (a) and a pitching (b) motion at the base, resulting in a ball and socket type joint which is comparable to the human shoulder. The two individual arms of the robot are connected via a single degree of freedom joint which is analogous to the human elbow (c). Lastly the robot's 'wrist' carries three individual rotary joints which can control a local pitch (d), yaw (f) and roll (e) of the tool head. Each of the six joints allows for a rotation range of $+/-360°$.

The robot is controlled digitally through a tablet, where the tool head translations with respect to the base are specified, as well as the pitch, roll and yaw angles of the tool head with respect to a

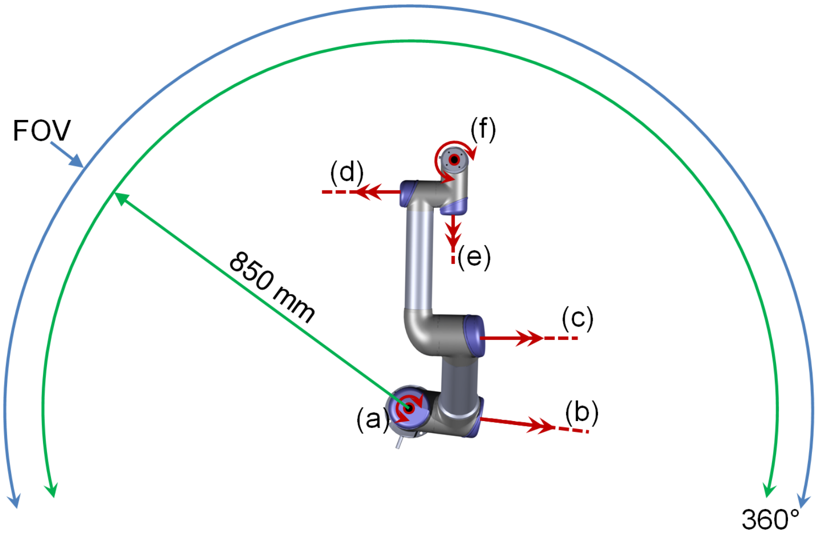

Figure 4.10: Illustration of the *Universal Robots - UR5* robotic arm, with rotary joint axes and range indicated. Outer blue contour indicates extended range, considering the velocimeter's depth of field. CAD render retrieved from the manufactures website.

user specified reference point and axis system. Both, translations and rotations can be specified to one hundredth of a millimetre, respectively of a degree or one thousands of a radians if preferred by the user. The repeatability of the tool head position is reported with $+/-0.1$ mm by the manufacturer (Universal Robots, 2017).

Instead of controlling the robotic arm parametrically, the collaborative robot can be moved manually into a desired position. This feature allows for fast manual positioning of the tool, in this case the velocimetry probe. The manual positioning is particularly useful when the recording positions are not defined a priori to a measurement. Whereas the parametric control is particularly handy to guarantee a minimum degree of overlap between subsequent measurements, the collaborative mode is interesting when scanning complex geometries with limited optical access. It further allows to attain a desired position in a non-intrusive way, meaning that the robotic arm itself is kept out of the fluid flow as much as possible. The latter aspect is important given that any point within the arm's range can be reached by different combinations of joint rotations. Thus, there are more and less suited combinations to attain a desired position when considering aerodynamic intrusiveness.

4.3. Robotic Manipulation

The coaxial velocimetry system presented in the first part of this chapter allows for a robotic approach to large-scale PIV measurements of complex flows. As such, this section focuses on the robotic manipulations of the measurement system. The robotic arm which is used in the presented work is introduced in Section 4.2.3. The introduction of a robotic arm for control of the imaging system poses some challenges and it raises specific questions, ranging from the accuracy of the positional information onto uncertainty involved in the data mapping procedure and selection of coordinate systems for the different components. These topics are addressed here.

Section 4.3.1 starts with a definition of the different coordinate systems which are involved in the measurement procedure. This lays the groundwork for the data mapping procedure, which transfers the measurement data from the camera reference frame onto the desired object domain using the positional information provided by the robotic arm. The data mapping procedures are detailed in Section 4.3.2. Once the data mapping procedures are established, the combined system's performance of CVV probe and robotic arm can be assessed as presented in Section 4.4.

4.3.1. Reference Frames

The robotic arm provides the required information of the velocimeter's position and orientation in order to transfer the measurement data recorded by the CVV probe onto a global reference system. However, the robotic arm works with its individual frames of reference, such that a multitude of reference frames is to be dealt with. These are the frame of reference of the CVV probe which is established through the geometrical calibration of the tomographic imaging system. More details on the calibration procedure are found in Section 6.4.1. The probe is mounted onto the robot's tool head which obeys to its own frame of reference $\vec{x}_{rh}$. The tool head axis system is of particular relevance for any rotations of the CVV probe. The position of the tool head is however referenced back to the base position of the *UR5* arm, which again carries its own frame of reference. Lastly, the user has to specify an axis system that is convenient for the final flow analysis. The latter is referred to as the global or the object frame of reference.

The definition of the camera reference frame is included in the CVV schematic in Figure 4.1. The exact location of the origin results from the geometrical calibration. Therefore, it does not necessarily coincide with the z-plane of the camera lenses as shown in Figure 4.11(b) where the CVV's frame of reference is labelled with subscript 'c'.

The second frame of reference is the tool head's coordinate system, 'rh'. Its origin can be specified by the user and it will define the axes of rotation for the pitch, roll and yaw motions. The relative distance between the origins of these first two frames of reference $\vec{x}_{cor}$ is of particular importance for the data mapping. A sketch of these two systems is included in Figure 4.11(b).

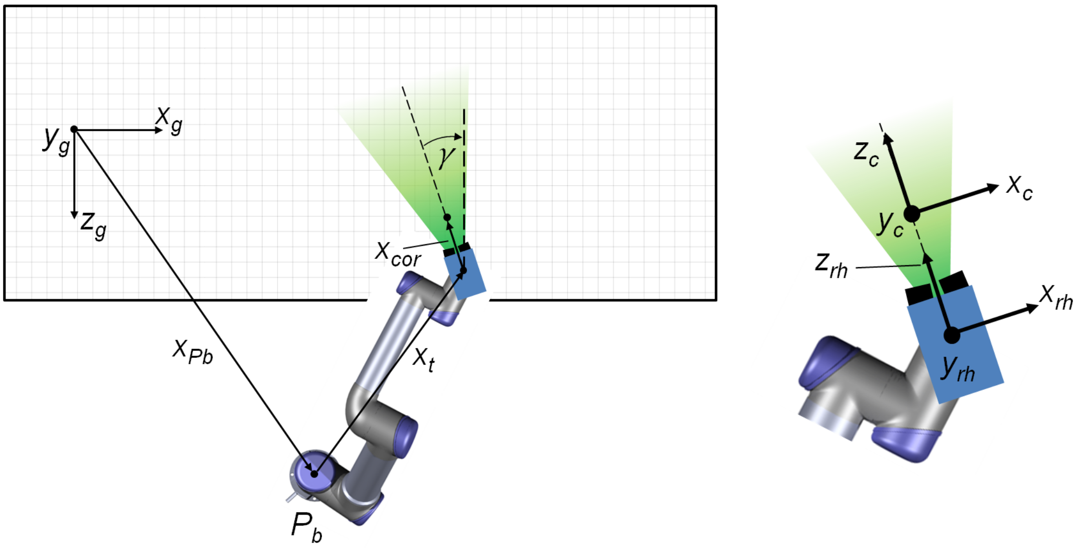

(a) Global overview. Plaid region indicating potential measurement domain of interest.

(b) Robot tool head and CVV probe

Figure 4.11: Fames of reference involved in the measurement and data mapping procedure.

Figure 4.11(a) instead contains a global overview of the measurement system and the respective reference frame. Note, that a reference frame for the robot base is omitted. Instead it is convenient to align the latter with the intended object reference system indicated by subscript 'g' and specify the location of the robot base with respect to the global origin by a vector $\vec{x}_{Pb}$. In this case the translation of the robot head with respect to its base $\vec{x}_t$ can be referenced in the same manner.

With the definition of these reference frames, the data mapping which transfers the measurement data from the velocimeter's reference to the object frame of reference can be defined.

4.3.2. Data Mapping

The previous section details the individual reference frames which are involved in the measurement procedure of the proposed robotic PIV approach. This provides the necessary knowledge to define the actual data mapping, which transfers measurement data acquired in the probe's reference frame 'c' to the object frame 'g'.

For each reconstructed tracer particle, the position $\vec{x}_c$ and velocity vector $\vec{u}_c$ is obtained in the camera frame of reference. Any rotation of the robot tool head is however referenced for rotations around its own origin. Thus, the measurements obtained in the velocimeter's camera reference system first have to be translated by $\vec{x}_{cor}$ to match the robot hand reference frame. Omitting this coordinate translation will yield an incorrect transfer of particle position, whereas velocity vectors are unaffected. Thus, it is of utmost importance to record the relative distance of the reference frame origins. The determination of $\vec{x}_{cor}$ is discussed further in the calibration procedures in Section 6.4.2.

Data which is transferred to the robot hand reference frame can be rotated (yaw, pitch and roll) and translated ($\vec{x}_t$ + $\vec{x}_{Pb}$) to map point data to the object reference frame. The rotations are accomplished by a series of Euler rotations, where the sequence of rotations is important. The latter may change for varying robot software and thus, the equations defining the rotations in this document are specific to the robot at hand and its calibration during the experimental campaigns.

The individual rotation matrices are defined as,

$$M_x = \begin{bmatrix} 1 & 0 & 0 \\ 0 & \cos(\beta) & \sin(\beta) \\ 0 & -\sin(\beta) & \cos(\beta) \end{bmatrix} \tag{4.15a}$$

$$M_y = \begin{bmatrix} \cos(\gamma) & 0 & -\sin(\gamma) \\ 0 & 1 & 0 \\ \sin(\gamma) & 0 & \cos(\gamma) \end{bmatrix} \tag{4.15b}$$

$$M_z = \begin{bmatrix} \cos(\alpha) & \sin(\alpha) & 0 \\ -\sin(\alpha) & \cos(\alpha) & 0 \\ 0 & 0 & 1 \end{bmatrix} \tag{4.15c}$$

Where α corresponds to the roll, β to the pitch and γ to the yaw angles. Combining the rotations specified in Equation (4.15), the particle locations in the robot hand reference frame can be mapped onto the object grid.

$$\vec{x}_g = \vec{x}_{rh}\left(M_x M_z M_y\right) + (\vec{x}_t + \vec{x}_{Pb}) \tag{4.16}$$

With $\vec{x}_{rh} = (\vec{x}_c - \vec{x}_{cor})$. For the mapping of the vector data such as tracer velocity, but also acceleration if recorded, the additional translations are irrelevant. Instead, the rotations only suffice to map the vector data. In the case of velocity, this reads,

$$\vec{u}_g = \left(M_y M_z M_x\right)\vec{u}_c \tag{4.17}$$

This provides the necessary tools to map data onto any desired reference system. The principles of coaxial velocimetry have been addressed beforehand. As such, the system's performance can be assessed as presented in the remainder of this chapter.

4.4. System Performance

Section 4.1 discusses the principles of the coaxial volumetric velocimetry system, whereas Section 4.2 details the specific hardware components. Lastly, Section 4.3 introduces the idea of robotic manipulations which is the tool to attain a rapid partitioning of a large measurement domain. The resulting performance of the velocimetry probe is discussed in this section, including the interaction of the velocimeter and the robotic arm.

Two small-scale experiments are conducted to evaluate the performance of the CVV probe and its interaction with the robotic arm. The first measurement series aims to establish the key characteristics of the individual CVV probe, such as its field of view, illumination and light scattering characteristics, resulting measurement volumes and similar. This first campaign is referred to as the 'flow in a box' experiment and is presented in Section 4.4.1.

The second campaign is conducted in a wind-tunnel environment and it further involves the interaction of the CVV probe with the robotic arm. A sphere flow is studied to understand the behaviour of the velocimeter and to gain experience with the robotic control system. This experiment is further used to validate the developed data merging routine as presented in Section 4.3.2. In the remainder of this document, this second experiment is named as the 'sphere flow experiment'. Details on this campaign are discussed in Section 4.4.2.

4.4.1. Flow in a Box

The first experimental campaign is focused on the coaxial velocimetry system. Thus, the velocimeter is maintained stationary and the inauguration of the robotic manipulation system is delayed to the subsequent campaign. Simple control of the seeding density is achieved by measuring in a confined volume. To this end, a $120 \times 40 \times 40$ cm^3 box is manufactured with one injection spot to seed the volume with Helium Filled Soap Bubbles and a tight window to install the velocimetry probe. A 2D illustration of the setup is presented in Figure 4.12.

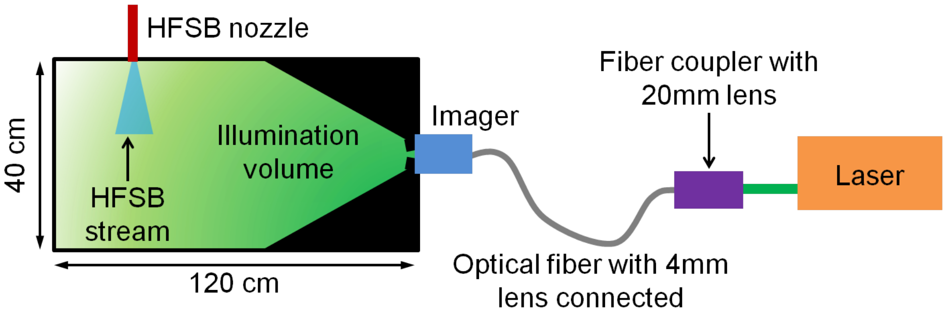

Figure 4.12: Experimental setup of the 'flow in a box' experiment.

As described in Section 4.2, the CVV probe integrates an optical fibre which is coupled to the described Quantronix Darwin Duo Nd:YLF high speed laser.

To establish the field of view, the box is filled sufficiently with tracer particles. Switching of the soap supply while continuously blowing air through the HFSB nozzle creates a circulatory flow inside the box. This provides a slow speed flow which can be reconstructed by means of Lagrangian particle tracking as detailed in Section 4.1.5. Figure 4.13 shows the volume in which particle tracks are reconstructed when using the full 800×600 px^2 sensors at a frame rate of 470 frames/s and a pulse energy of 11.2 mJ.

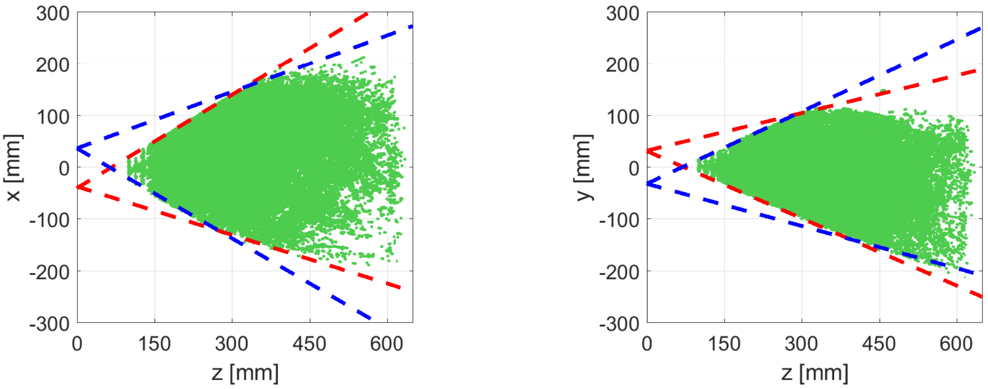

(a) Top view

(b) Side view

Figure 4.13: Indication of the measurement volume of the coaxial velocimetry system as established during the 'flow in a box' experiment by visualisation of reconstructed particle tracks (green) from $1,000$ time-resolved PIV image pairs. Red and blue dashed lines indicate field of views of separate cameras. Empty region in top right of Figure 4.13(a) is due to the box ceiling.

The illustration in Figure 4.13 contains particle tracks from $1,000$ time instances, and thus, the visualisation may not be taken as an indication for the seeding concentration inside the box. Instead, an image source density of 0.016 ppp is observed, while the concentration of reconstructed and tracked particles is measured with 0.15 particles/cm^3.

The approximation of the cameras FOVs in Figure 4.13 highlights that the measurement domain is limited by the overlapping FOVs in x and y. Thus, the laser expansion of the established setup is sufficient and it does not limit the measurement volume in the lateral and vertical directions.

The conical shape of the observation domain further implies, that the suggested minimum distance of $z_{min} = 175$ mm for reasons of flow intrusiveness does not compromise the overall measurement volume significantly, given that the measurement cross section at such low distances to the CVV probe is smallest anyway. At a distance of 200 mm to the CVV probe the observation domain spans 160×115 mm^2 in x and y, respectively. This expands to 410×320 mm^2 at $z = 500$ mm. The maximum measurement distance is $z_{max} = 635$ mm, resulting in a measurement depth in excess of 40 cm when accounting for the previously discussed minimum distance z_{min}. The depth may be further increased by increasing the laser power, if necessary. The volume captured in the presented measurement equates to 20 l, which is among the larger domains when comparing to the survey of tomographic PIV applications presented in Section 3.2.

One of the key challenges which is determined in the theoretical analysis in Section 4.1 is the fourth order light intensity reduction with object distance. To verify these findings, the box in Figure 4.12 is opened and a suction system is installed just opposite to the HFSB nozzle. In this manner a thin, controlled tracer stream is realised, allowing to vary the distance of the CVV probe towards the tracer particles in a controlled fashion.

Recording the peak intensity of imaged particles at varying camera distances and different aperture settings yields the desired trend of light intensity recorded by the velocimetry probe versus object distance as shown in Figure 4.14.

The experimental data agrees well with the expected trend. The only deviation from the theoretical trend is observed at the large aperture setting of $f_{\#} = 4$, at the smallest object distance. Due to the small value of $f_{\#}$, more light is received by the CCDs. In the particular case, the camera is saturated and thus, the true peak intensity cannot be resolved.

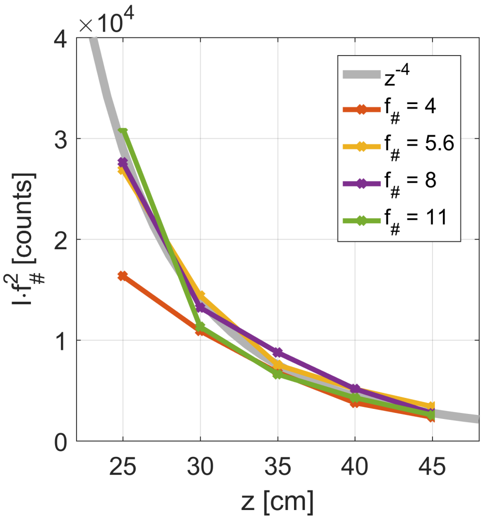

Figure 4.14: Light intensity received by the CCDs scaled by $f_{\#}^2$ as function of object distance. Gray reference indicating the z^{-4} relation established in Equation (4.11).

Nonetheless, the visualisation of the light intensity variation with object distance in Figure 4.14 stresses the rapid decay of recorded particle intensity with object distance. The loss of light intensity with z will ultimately limit the maximum achievable measurement depth and thus, the maximum measurement volume. Yet, the relative aperture cannot be opened excessively to record more light as it will cause the particles close to the CVV probe to be saturated. Further, the full depth of field shall be in focus and thus, the $f_{\#}$ cannot be too low (see Equation (4.5)).

4.4.2. Sphere Flow Experiment

The flow in a box experiment discussed in Section 4.4.1 proves the concept of coaxial volumetric velocimetry. Theoretically expected properties are validated and the measurement domain is characterised for measurements in a confined volume. The sphere flow experiment presented in this section tackles two major steps in pursuit of the proposed robotic PIV approach: the first step herein is the introduction of the robotic control system. Secondly, the complete system is taken to a wind tunnel environment. Assuming a successful system integration, multiple measurements can be acquired to validate the data mapping routine described in Section 4.3.2.

Apparatus

The flow around a 10 cm diameter sphere is deemed as a suitable test case for the robotic PIV system. The measurements are conducted in the W-tunnel at TU Delft. For the measurements at 3.0 m/s a square $1 : 4$ contraction is installed, yielding an open test section of 60×60 cm^2 for the open-return-circuit tunnel. A novel large-scale HFSB seeding system is installed in the settling chamber of the wind tunnel. The seeding system spans 15×47.5 cm^2, containing 80 HFSB nozzles which produce on the order of 2×10^6 bubbles/s in nominal operation. The seeding is controlled via a LaVision fluid supply unit. The complete seeding system is equivalent to the system used in the large scale demonstration experiment and it is discussed in more detail in Section 6.3.1. A schematic of the experimental setup alongside images of the operational seeding system and the actual setup are shown in Figure 4.15.

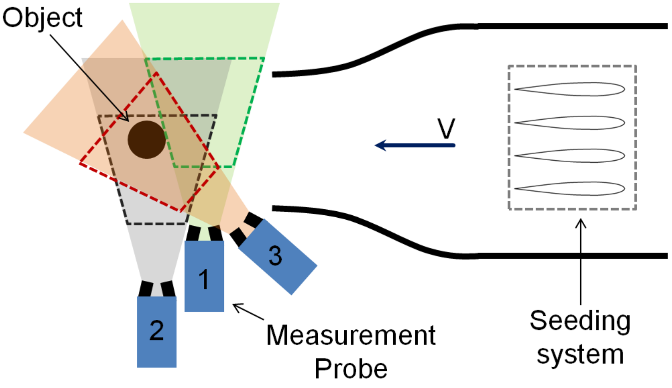

(a) Schematic setup - Top view.

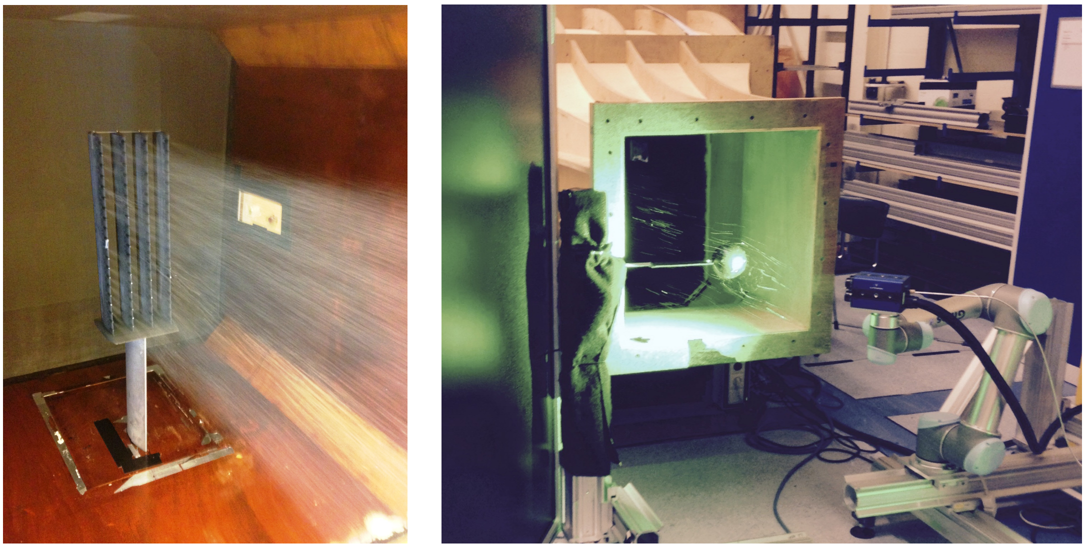

(b) Operational HFSB seeder

(c) Setup including UR5 robot arm.

Figure 4.15: Experimental setup of the sphere flow experiment.

Vibration Assessment

Prior to any flow field measurements the system vibrations with the robotic PIV system exposed in the open test section are assessed. The CVV probe is exposed in the centre of the test section, imaging a stationary speckle pattern at 40 cm distance to the probe. Cross correlation between time-resolved images offers an insight on the vibrations of the velocimetry probe on the robot head. The vibrations are assessed on a velocity range of $2.0 - 30.0$ m/s in increments of 2.0 m/s. Over the complete speed range, the system is found to be stable with vibrations measured in terms of the root-mean-square displacement of the recorded speckle pattern staying within 5% of the pixel size. Note that at the indicated measurement distance, a single pixel covers less than 0.5 mm in physical space. Further, the maximum displacement of the CVV probe with respect to wind-off conditions is observed to be within 2.0 px at the maximum speed of 30.0 m/s. This provides a measure of the elastic displacement of the probe on the robotic arm under aerodynamic loads. The displacement observed is sufficiently small to guarantee the positional information provided by the robotic control software is indicative of the true position. This is a necessity for a successful data mapping.

Velocity Measurements

Flow measurements are taken at three recording positions as indicated in Figure 4.15(a). The first two positions consider the upstream flow, with the CVV probe oriented perpendicular to the free stream direction. The fist view is much closer to the seeded flow region, whereas the second view is taken from a larger distance. This allows for a comparison of data properties at different depth locations with respect to the velocimeter. The third and last view incorporates a yawing motion and it covers a portion of the sphere wake.

Time averaged velocity data of the individual recording positions is presented in Figure 4.16.

It can be seen that the first two views lack data in the wake. Further, given that the first view is much closer to the seeded flow, the measurement domain spans a smaller cross section as compared to the second view. The idea presented in this work is the merging of these individual measurements to one ‘large-scale’ measurement domain. Following the merging routine as defined in Section 4.3.2, a combined velocity field is obtained as shown in Figure 4.17.

The merged velocity field in Figure 4.17 indicates that the data mapping allows for combination of individual measurements based on the positional information of the CVV probe provided by the robotic arm. Clear flow features such as a flow deceleration upstream of the sphere, some acceleration alongside as well as a wake region with reverse flow downstream are well captured. A question that arises however, is how accurate the data is. To this end a error analysis is carried out, addressing the uncertainty in the particle positioning.

Uncertainty Analysis

For quantification of the uncertainty in the particle positions, the temporal information of the particle tracks is utilised. Assuming that any error in the reconstruction of the particle positions is randomly distributed, fitting a polynomial to the estimated locations can be regarded as a true trajectory. The difference between the estimated position and the value of the polynomial at the specific time instant then describes the error estimate for a specific particle.

The trajectories are approximated as functions of time, with one-dimensional functions for each axis component ($x_i = f(t)$). Parameters to be selected are the polynomial order as well as the fit length. The analysis presented here is based on second order polynomials which are fitted to eleven data points. At the sixth point, which is the central data point, the error is evaluated. Basically, the polynomial fitting follows the procedure of a Savitzky-Golay filter (Savitzky and Golay, 1964).

Within a selected volume, the root-mean-square error is computed for the particle positions, yielding maps for the positional uncertainty for the three axis components. A representative result of the analysis is presented in Figure 4.18.

The error maps in Figure 4.18 show significant differences in the positional uncertainty for the in-plane (Figures 4.18(a) and 4.18(b)) and the out-of-plane (Figure 4.18(c)) position. For the lateral and vertical particle positions, the error is within one tenth of a millimetre. In the depth direction instead, the error for the specific plane shown in Figure 4.18(c) reaches up to 0.3 mm. Interestingly, the error is maximal in the plane centre tapering off along the radial direction.

It is hypothesised that the peak error in ϵ_z in the centre of the measurement domain originates from the low tomographic aperture of the coaxial velocimetry probe. As indicated in Figure 4.3, the depth of a reconstructed tracer particle d_z is expected to be maximal when recorded in the image centre. Instead capturing a particle off-centre, the longest dimension of the reconstructed particle l_z will be inclined and its projection onto the z-axis d_z will be reduced. In the assumption that a smaller particle reconstruction yields a more accurate estimate of its location, the reconstructed particle position in depth of a particle imaged along the sensor edges will feature higher accuracy as compared to a tracer imaged in the sensor centre.

Following this hypothesis, the in-plane uncertainties ϵ_x and ϵ_y would need to be increased away from the symmetry axes. This cannot clearly be observed from the error maps in Figures 4.18(a) and 4.18(b), since the error is too small and not well resolved.

To compare the results to well known reconstruction techniques the data presented in Figure 4.18 is treated with a conventional MART reconstruction and Gaussian peak fitting instead of the Lagrangian particle tracking procedure. The resulting error maps are shown in Figure 4.19.

In the case of MART reconstructions the earlier hypothesised trend of increasing uncertainty in-plane and away from the symmetry axis can clearly be seen in Figures 4.19(a) and 4.19(b). Instead,

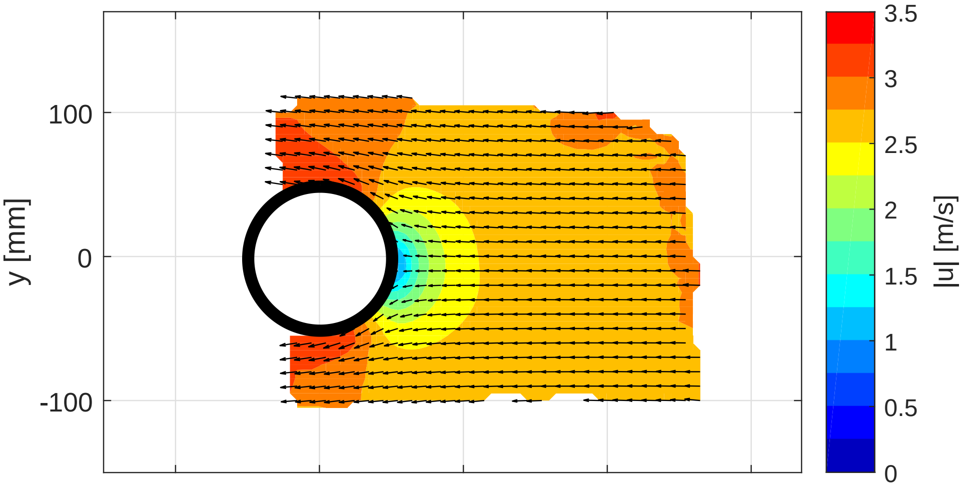

(a) First view

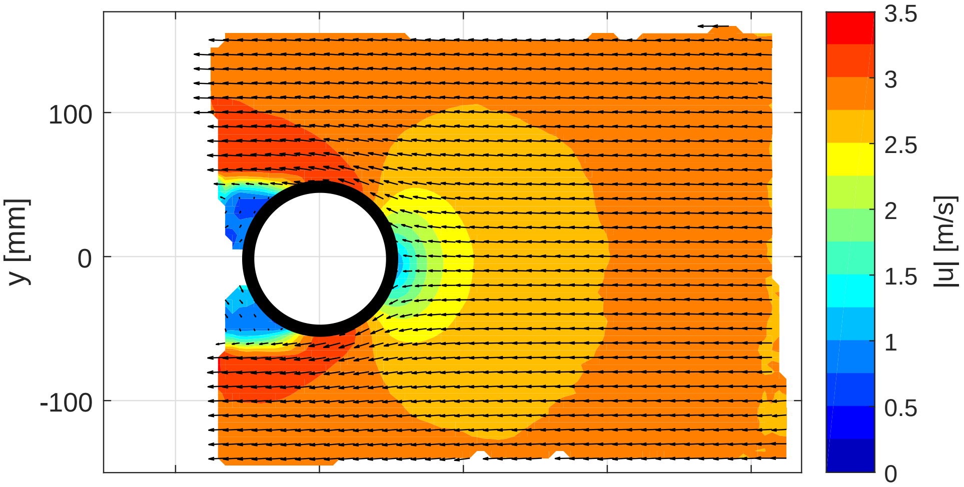

(b) Second view

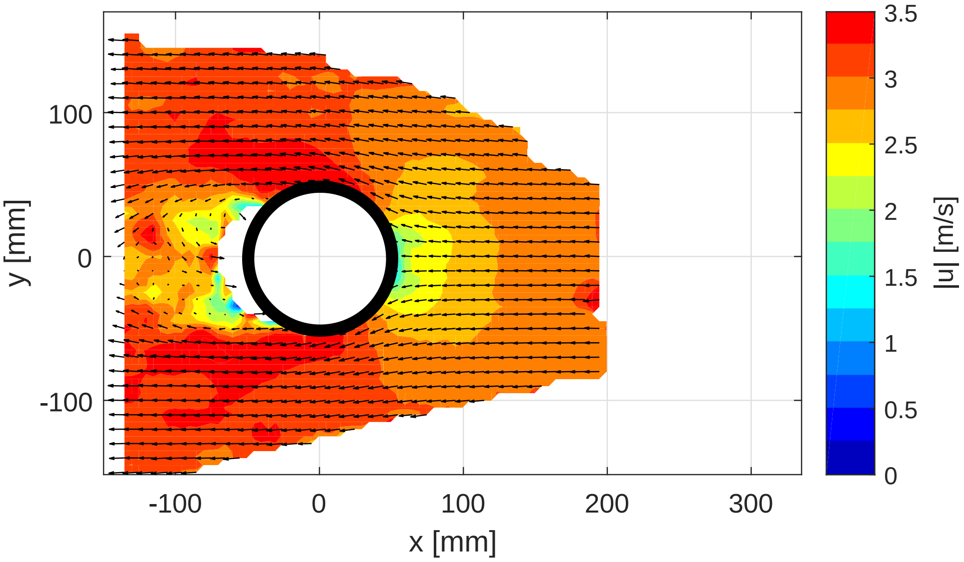

(c) Third view

Figure 4.16: Time averaged velocity fields for the flow around a sphere in the centre plane, corresponding to the viewing directions indicated in Figure 4.15(a).

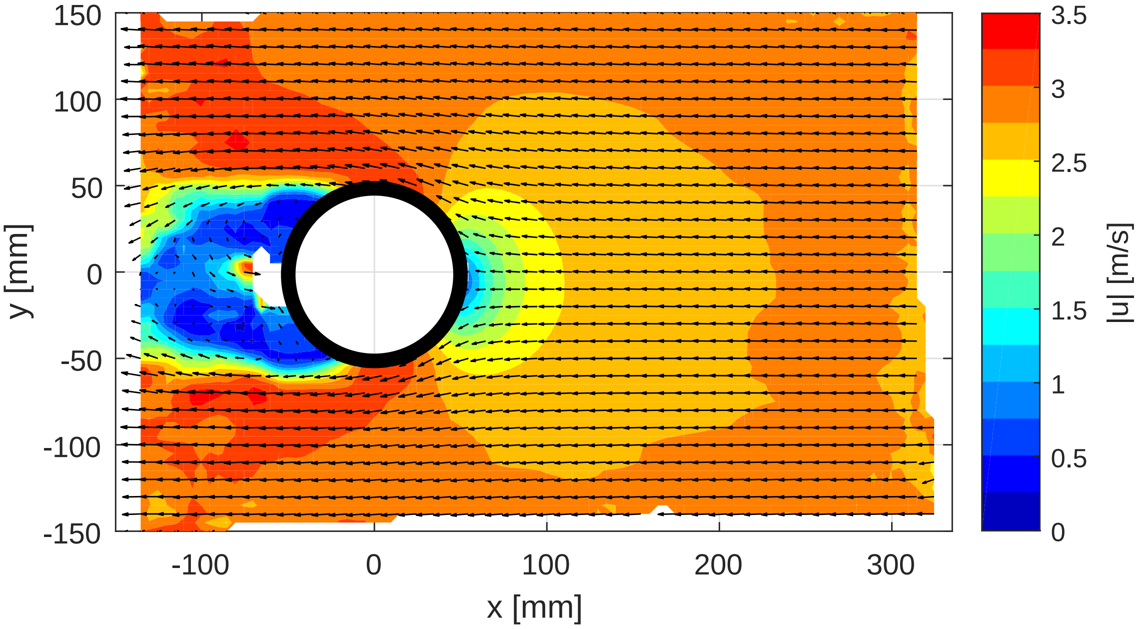

Figure 4.17: Contour of velocity magnitude in the sphere centre plane, resulting from the merged dataset of three individual measurements as indicated in Figure 4.15(a). Cubic grid cells of 8 cm^3 with 75% overlap. Vector field sub-sampled by a factor 2.

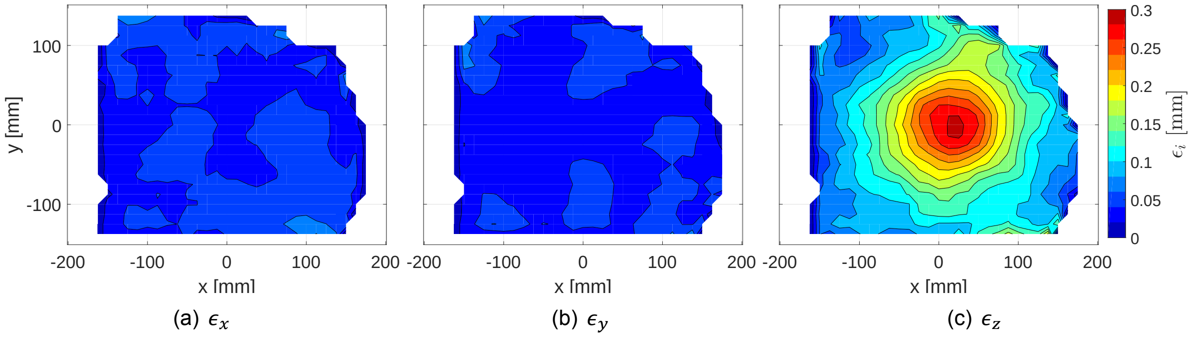

(a) ϵ_x (b) ϵ_y (c) ϵ_z

Figure 4.18: Positional uncertainties along axis directions for a free stream measurement at 3.0 m/s using Shake the Box particle tracking and the setup of the sphere flow experiment.

the peak error in the image centre for the depth direction is not as sharp as in the case of the Shake the Box particle tracking. Still, the maximum error is in the centre.

Independent of the error shape, it must be stressed that the uncertainties following the conventional MART reconstructions are more than three times higher than in the equivalent case based on Lagrangian particle tracking. Thus, the chosen STB algorithm does not only process the PIV images more quickly, but it also yields more accurate results.

So far the discussed uncertainties refer to an arbitrarily selected plane of reference. Due to the unique feature of the coaxial volumetric PIV approach, the measurement depth is on the same order of magnitude as its width and height. Thus, the variation of the uncertainty along the depth direction is also of interest. To evaluate the latter, an interrogation window of 50×50 mm^2 is positioned in the image centre and the uncertainty inside this interrogation window is tracked in depth. The resulting trends for the three uncertainty components are shown in Figure 4.20 for the STB processing strategy.

The in-plane uncertainties are seen to stay consistently low across the measurement depth. The uncertainty in depth however, is observed to increase with object distance. Once more the illustration in Figure 4.3 supports this observation. A point at a far distance is imaged with lower tomographic aperture β as compared to a point close to the cameras. Following the relation in Equation (4.1), the depth of the reconstructed particle shape is longer and therefore the uncertainty is higher.

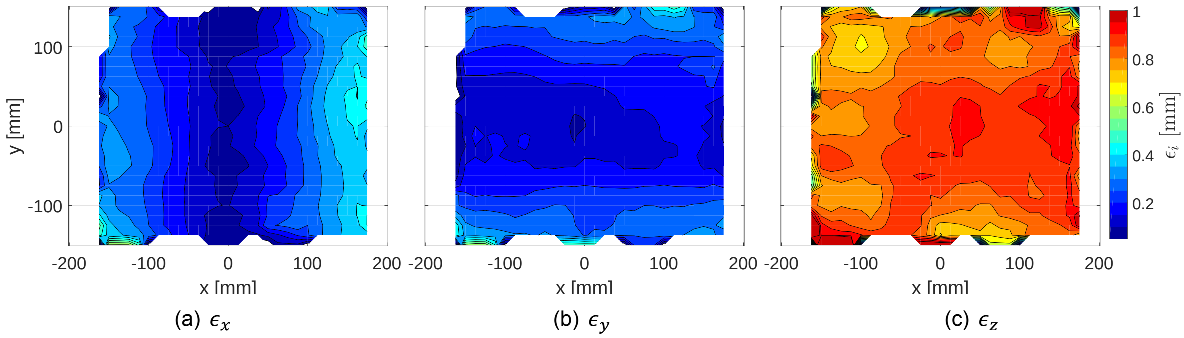

(a) ϵ_x (b) ϵ_y (c) ϵ_z

Figure 4.19: Positional uncertainties along axis directions for a free stream measurement at 3.0 m/s using MART reconstructions and nearest neighbour particle tracking on the same data as shown in Figure 4.18.

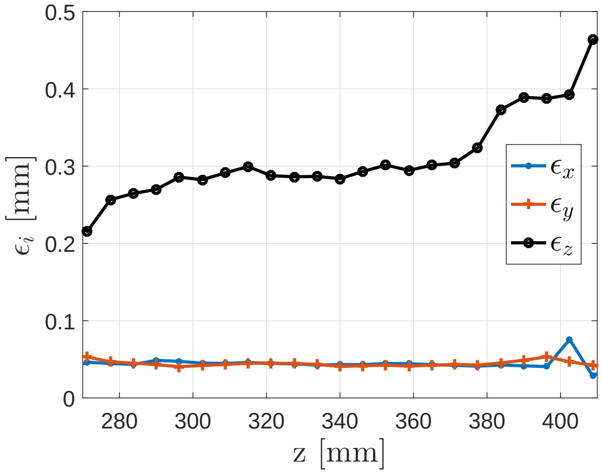

Figure 4.20: Variation of uncertainty in particle position with measurement depth.

It is shown that the proposed coaxial volumetric velocimetry system obeys original imaging characteristics which affect the positional uncertainty of particle reconstructions. Overall it is concluded that the uncertainties are in an acceptable range, providing confidence to apply the measurement technique in a large scale demonstration experiment. Prior to the presentation of the demonstration experiment, a chapter is dedicated to the data reduction techniques.

5

Data Analysis and Reduction Techniques

In a first instance any PIV or PTV system is recording images of some tracer particles embedded in a fluid flow. The experimentalist employing the measurement tool is eventually interested in the aerodynamic characteristics of the flow, may this be the mean velocity field or the vorticity skeleton around an object of interest to name two examples. The path from the raw image recordings to the flow field representation is by no means trivial, and various strategies are available to evaluate the recorded data. This chapter focuses on the data reduction techniques and analysis tools that are applied to the experimental data. A more general theoretical background on tomographic imaging and particle tracking techniques tailored to coaxial velocimetry can instead be found in Chapter 4.

The chapter starts with a discussion of the pre-processing strategies employed on the raw image data, see Section 5.1. Image pre-processing can be of great importance given that remaining image noise can yield incorrect particle tracks, respectively velocity vectors in the case of correlation based PIV, and therefore, effective image pre-processing can enhance reliability and thereby quality of the resulting velocity field. The actual particle tracking algorithm and its specific settings are discussed subsequently in Section 5.2. Section 5.3 focuses on the processing of the particle track data instead. Key topics are outlier removal as well as the grid conversion of the randomly distributed particle tracks onto a uniform data structure. The structured data is then analysed by means of different flow analysis techniques. The latter are discussed in Section 5.4.

5.1. Image Pre-Processing

For fast and reliable processing high image quality is preferable as image noise can promote reconstruction of ghost particles. Naturally, PIV images contain background noise resulting from object reflections. If a reflection saturates a pixel on the sensor, any tracer passing and imaged on the same pixel cannot be resolved. Such reflections should be avoided at all times if possible. Less strong reflections and other image noise can still be filtered to a large extent using image pre-processing.

For the presented experimental data of the large-scale demonstration experiment, two lines of image pre-processing strategies are applied: a moderate filtering for nominal acquisitions, next to a more aggressive pre-processing for recordings with unsteady background noise. The latter distinguishes further for the degree of noise influence. The procedures for the two cases are discussed in the subsequent sections.

5.1.1. Nominal Recordings

Figure 5.1(b) shows a nominal data recording for the presented measurement campaign. Both, the bicycle and the mannequin as shown in Figure 5.1(a), cause a clearly visible background in the image. Despite small vibrations of the test object, the background noise can be considered steady and thus, the images are classified as nominal.

For noise elimination the Butterworth filter, which is a high pass frequency filter, as first presented by Sciacchitano and Scarano (2014) is found to be effective without being too erosive on the true signal

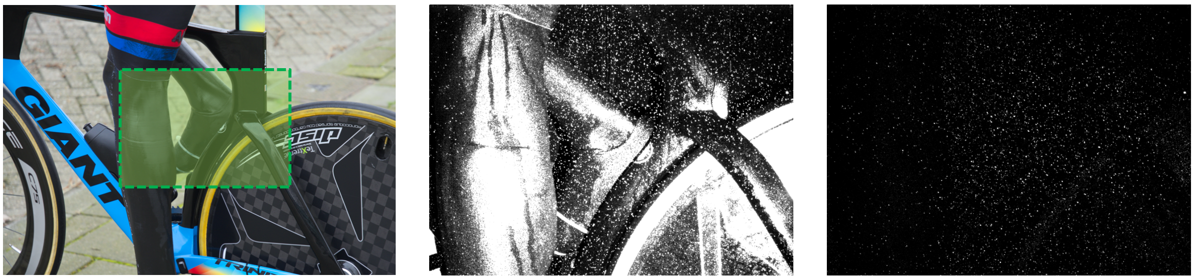

(a) FOV indication

(b) Raw image. Intensity scale $0-64$ counts black to white.

(c) Pre-processed with Butterworth filter, seven images filter length. Intensity scale $0-64$ counts black to white.

Figure 5.1: Sample of a nominal image recording prior and after image pre-processing using a Butterworth filter.

from the tracer particles. The resulting pre-processed image after filtering with a filter length of seven images for the sample shown here is presented in Figure 5.1(c). The gradient in image seeding density from left to right is explained by the presence of the leg, which shadows any particles between the shank and the bicycle frame. Despite the rather bright reflection on the calf, particles are still visible in this region on the pre-processed image. Similarly, it is appreciated that the bright side-wall of the rear tire is successfully removed while retaining particle intensities in the same area. The quality of the resulting image seen in Figure 5.1(c) is considered desirable.

5.1.2. Noise Affected Recordings

For a significant share of the acquisitions, unsteady background noise aggravates the image processing. For the presented data a very case specific observation is made: to minimise aerodynamic drag, time trial suits for cyclists tend to be rather tight. Consequently, most of the fabric is under tension when fitted to the mannequin. In combination with any concave shape on the body, as present due to the well defined muscular structure, some regions of the suit are not in direct contact with the mannequin. The airflow passing these regions does then cause the fabric to be excited locally. Due to the reflective character of the textile, this yields a relatively strong and unsteady background noise. The unsteadiness of the reflection reduces the effectiveness of the Butterworth filter described in Section 5.1.1, and thus, excessive noise is left in the images, requiring alternative pre-processing prior to particle tracking.

An extreme sample is shown in Figure 5.2 with a large area along the thigh's side suffering the previously described suit vibration. While this phenomenon cannot be appreciated from the stationary raw image in Figure 5.2(b), following the standard processing procedure described in Section 5.1.1 yields an image with a significant portion of background noise remaining exactly in the location where the fabric vibration is observed, which can well be seen in the left-hand side of Figure 5.2(d).

An alternative filtering approach is sought to handle the unsteady image noise. Attempting a Proper Orthogonal Decomposition (POD) as suggested by Mendez et al. (2017) with a subtraction of the first forty modes weighted by the time coefficient as shown in Figure 5.2(e) does however not yield a significant improvement.

An effective and yet computationally affordable approach features an initial spatial smoothing using a Gaussian Smoothing operator with a 5×5 pixel kernel. This reduces the extent of the noise fluctuations as they are distributed over more pixels and therefore, the subsequent application of the high pass frequency filter is more effective. Still, for the extreme case presented here there is some noise content remaining as can be seen in the top left of Figure 5.2(f).

For a small share of measurements the smoothing operation described is still not sufficient. An effective, yet also erosive approach is an increase of the intensity threshold for particle detection, as discussed in Section 5.2. A smarter, though slightly more expensive method to further treat the images is based on the unsteadiness of the light intensities: the standard deviation of intensity is high in the noise affected areas (see Figure 5.2(c)) and therefore, subtracting the root-mean-square of the recording sequences, smoothed over a large 9×9 pixel kernel and scaled by a factor $1/12$, proves to be an effective, local noise filter resulting in the image shown in Figure 5.2(g). The scaling factor is however case dependent. This filter is only applied to a fraction of measurements, as any filtering step adds to the data erosion on the images.

(a) FOV indication

(b) Raw image

(c) Root mean square of intensity. Color code varying from black (0 counts) to red (128 counts).

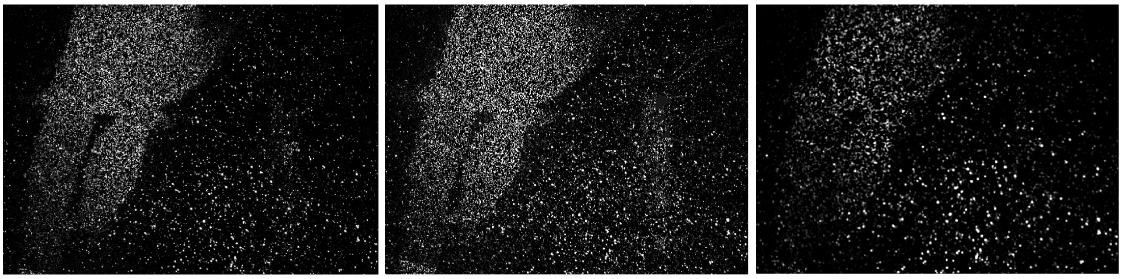

(d) Butterworth filter, seven images filter length.

(e) POD filter, 40 modes removed.

(f) 5×5 kernel Gaussian smoothing followed by Butterworth filtering, seven images filter length.

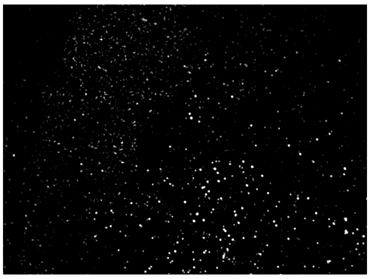

(g) Figure 5.2(c) smoothed (9×9 kernel) and scaled ($\times 1/12$), subtracted from Figure 5.2(f) to suppress unsteady noise.

Figure 5.2: Sample of a noisy image recording prior and after image pre-processing using various filtering approaches. The raw data image in Figure 5.2(b) obeys a wider intensity scale from $0 - 512$ counts instead of $0 - 64$ counts from black to white in the pre-processed images in Figures 5.2(d) to 5.2(f).

Table 5.1 indicates the percentage of nominal, noisy and abnormal runs for the presented experimental campaign. While the relative share of nominal runs may appear low, it should be understood that this is rather particular issue to the nature of the experiment rather than a malfunctioning of the measurement system under consideration.

Table 5.1: Share of nominal and noise affected runs distinguished by measurement location.

Location	Total	Nominal	Noisy	Abnormal	Unit
LHS	241	131	80	30	[#]
		54.4	33.2	12.4	[%]
RHS	209	147	59	3	[#]
		70.3	28.2	1.4	[%]
All	450	278	139	33	[#]
		61.8	30.8	7.3	[%]

The observed noise effects in the presented measurement campaign appear to be very specific to the test object. Oscillatory background noise is however well imaginable in various other applications. This could for instance be spinning rotors passing through the FOV periodically, rotating wheels of vehicles or reflections in a rolling floor wind tunnel to name a few examples.

5.2. Particle Tracking - Shake the Box

The acquired data is analysed using Lagrangian particle tracking. Specifically, the Shake the Box algorithm as proposed by Schanz et al. (2016a) and implemented in `DaVis 8.4.0` is employed. The key principles of the particle tracking technique are outlined in Chapter 4, whereas this section focuses on the specific settings used to process the acquired data in the presented experimental campaign. The STB input parameters are summarised in Table 5.2.

Details on the various parameters in Table 5.2 can be found in the literature on the tracking algorithm (Schanz et al., 2016a) and the `DaVis 8.4.0` manual (LaVision GmbH, 2016). A selection of key parameters is briefly discussed in the following. The general idea is to provide tight limits for particle detection and tracking such that the process can run fast, while setting the bounds sufficiently large for all physical flow features to be captured.

Despite STB being a particle based rather than a voxel based tracking algorithm, displacement limits are still specified in voxel units. For the present test case a voxel unit equates to 0.27 mm in length. A particle at 14 m/s free stream velocity moves 18.5 mm between two frames, meaning that the corresponding voxel displacement results to 69 vox per image. A displacement limit of 80 vox therefore, allows for 16% of acceleration beyond the free stream velocity while limiting the search radius for particle pairing to a reasonable size.

Due to the deep measurement volume of the CVV system the particle displacement in pixel units is varying significantly with object distance. Close to the probe, the field of view is small, therefore the expected free-stream particle displacement of 18.5 mm results in a significant pixel displacement of up to 78 px at 20 cm object distance. At a typical object distance of 40 cm the pixel displacements reduces to 39 px, while at a far object distance of 60 cm the displacement only spans 25 px.

The particle acceleration is further limited in a relative and absolute sense, which helps eliminating spurious tracks resulting from image noise. A statistical analysis of the wake flow downstream of the left calf, which is seen to be amongst the most turbulent flow regions around the cyclist, shows that median particle accelerations stay within 1200 m/s^2 which corresponds to $\Delta_{\Delta_p,rel} = 10\%$ of the allowed maximum particle displacement. Figure 5.3 indicates the range of accelerations measured across the shank wake. Thus, the previously indicated acceleration limit of 16% is considered reasonable.

For slowly moving particles, the acceleration limit is instead specified in an absolute sense. The limit is set to $\Delta_{\Delta_p,abs} = 3$ vox. The less critical limiter is applied to any particle displacement.

A result of the large particle displacements is a small number of recordings of any individual particle. A particle moving at free stream velocity in the x-direction of the camera reference frame, passes a field of view of approximately 15 cm when being close $(20$ cm$)$ to the camera. Thus, the particular particle will appear in only eight time instances in the recordings. Consequently, the resulting particle tracks are

Table 5.2: Standard Shake the Box settings for nominal recordings LHS calibration.

Category	Parameter	Symbol	Value	Unit
Volume settings[*]	X	x_{min}	-130.4	[mm]
		x_{max}	$+133.6$	[mm]
	Y	y_{min}	-87.4	[mm]
		y_{max}	$+104.9$	[mm]
	Z	z_{min}	-400.1	[mm]
		z_{max}	$+150.8$	[mm]
	Voxel size	l_{vox}	0.27	[mm]
Particle detection	2D intensity threshold	I_{min}	20	[counts]
	Max. triangulation error	ϵ_{Δ}	1	[px]
	Weak intensity removal, abs.	$f_{I_{abs}}$	0.1	[−]
	Weak intensity removal, rel.	$f_{I_{rel}}$	0.1	[−]
	Close distance removal	r_{vox}	3	[vox]
Optical transfer function	OTF size factor	$f_{r_{OTF}}$	1.5	[−]
	OTF intensity factor	$f_{I_{OTF}}$	3.0	[−]
	Initial intensity radius	r_0	0	[px]
	Later intensity radius	r_1	0	[px]
	Residuum OTF radius	r_{res}	2	[px]
Iteration settings	Shake delta	δ_S	0.2	[vox]
	Add particle iterations	m_{add}	4	[−]
	Refine iterations	m_{ref}	4	[−]
Displacement limits	Max. search radius	Δ_p	80	[vox]
	Max. change in Δ_p, abs.	$\Delta_{\Delta_p abs}$	3	[vox]
	Max. change in Δ_p, rel.	$\Delta_{\Delta_p rel}$	15	[%]
Track settings	Min. track length	l_{min}	5	[−]
	Polynomial fit order	m	2	[−]
	Polynomial fit length	n	7	[−]
	Polynomial data weighting	w_n	uniform	[−]

relatively short. Therefore, the minimum track length is also kept short with five points only. A longer minimum track length is deemed favourable as it reduces chances of noise being tracked.

Processing one dataset with the input specified in Table 5.2 yields a cone of particles whose boundaries in x and y are limited by the overlapping FOV of the four high speed cameras, assuming there is no object in the image. In depth, the limits are determined by the minimum distance to the velocimetry probe as specified by the user through z_{max} and the scattered light intensity of particles at a far distance. Figure 5.4 shows a sample result for the flow passing between the riders face and fore arms.

For a nominal measurement with full seeding, the reconstructed particles span a cone of $13 \times 8\,\text{cm}^2$ at $20\,\text{cm}$ distance to the camera housing, which expands to $40 \times 25\,\text{cm}^2$ at $60\,\text{cm}$ distance. If seeding is available, the measurement depth $(z_{max} - z_{min})$ can exceed $50\,\text{cm}$. The maximum measurement volume observed during the large-scale demonstration (see Chapter 6) equals approximately $25\,\text{l}$. On average each measurement contains about 500 particles per frame. Normalising by the maximum measurable volume yields a seeding concentration of $0.02\,\text{particles/cm}^3$.

For each reconstructed particle the position (x, y, z), the velocity (u, v, w), and the acceleration (a_x, a_y, a_z) are specified in the camera reference frame together with information on the time step, the track ID and the particle light intensity.

As indicated in Sections 5.1 and 6.4.1, different pre-processing strategies and varying calibrations

---

[*] Note that the specified in-plane limits (x & y) are referenced to the z_0-level of the calibration. Thus, the actual measurement domain may exceed those limits at object distances beyond the z_0-plane. The indicated values allow for the full images to be analysed without restricting the reconstruction volume in x or y. Further, the z-axis in the processing software is pointing towards the velocimeter, such that the interpretation of z_{min} and z_{max} is opposite to the interpretation given earlier in Chapter 4.

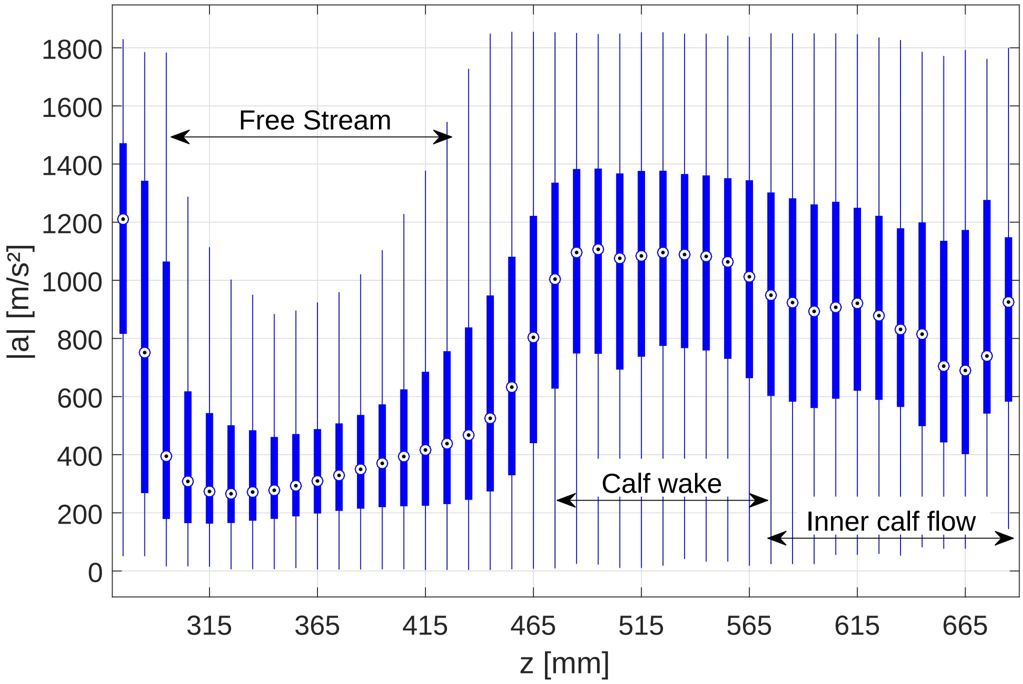

Figure 5.3: Statistical distribution of particle accelerations across the shank wake, used to estimate the highest particle accelerations to be expected around the cyclist. Boxplot shows particle accelerations resulting from STB as function of measurement distance z on intervals of $\Delta z = 10$ mm. Median indicated by circular marker on solid bar indicating upper and lower quartiles.

are used, during the experimental campaign. This affects some of the STB parameters specified in Table 5.2. As such, Table 5.3 highlights the changes in the input parameters for the Shake the Box algorithm. Due to the calibration difference, the voxel size changes which affects the displacement limits. Further, the intensity threshold for particle detection is lowered for the recordings pre-processed with the Gaussian smoothing operator as the light intensity is distributed over a larger kernel.

Table 5.3: Changes in Shake the Box settings for RHS calibration and noisy recordings.

Category	Parameter	Symbol	LHS	RHS	Gauss	Unit
Volume settings	X	x_{min}	−130.4	−140.0	–	[mm]
		x_{max}	+133.6	+143.3	–	[mm]
	Y	y_{min}	−87.4	−97.7	–	[mm]
		y_{max}	+104.9	+114.6	–	[mm]
	Z	z_{min}	−400.1	−400.1	–	[mm]
		z_{max}	+150.8	+150.1	–	[mm]
	Voxel size	l_{vox}	0.27	0.74	–	[mm]
Particle detection	2D intensity threshold	I_{min}	20	–	7	[counts]
Displacement limits	Max. search radius	Δ_p	80	30	–	[vox]

5.3. Track Data Post-Processing

Despite the vast advances in particle tracking reliability realised by the Shake the Box algorithm, identification and removal of incorrect particle tracks remains a key exercise in the processing chain. The processing strategies and parameters employed on the particle track data in the presented measurement campaign are discussed in this section.

First, the filtering strategies to identify incorrect particle tracks are presented in Section 5.3.1. This is followed by a discussion on the grid conversion of the data in Section 5.3.2. Lastly, statistical data convergence is studied in Section 5.3.3.

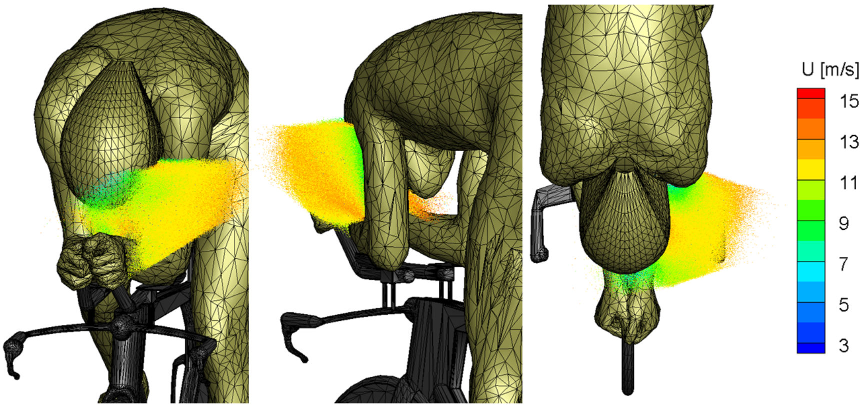

Figure 5.4: Particle cone resulting from Shake the Box processing on a single dataset of $5,000$ images. Region with limited optical access in between rider's face and arms.

5.3.1. Data Filtering

Identifying true measurements from spurious data remains a non-trivial task. As discussed, incorrect pairing of particles and noise sources such as background reflections can represent origins of incorrect measurements. Typically, outlier detection algorithms are based on statistical properties of the data at hand. Though, knowledge on general flow properties can also be used to filter data based on specific flow characteristics.

Velocity Range

Knowledge on the flow characteristics is used to provide margins on the particle velocities. For a free stream velocity of 14 m/s any reverse flow in the streamwise direction is expected to have a magnitude of less than 7 m/s. For the vertical velocity component v, a significant upwash is expected as the flow underneath the chest streams around the waist, whereas no comparable region of strong downwash is identified. Thus, the v-component is limited to $-10 \leq v \leq 14$ m/s. In the lateral direction the magnitude is bounded to $|w| \leq 10$ m/s.

Intensity Distribution

Due to the illumination and light scattering characteristics of the coaxial imaging approach discussed in Chapter 4, it is expected that the particle intensity recorded on the CCD decays with the fourth power of particle distance to the imaging probe. While this holds true for particle data, the intensity magnitude and distribution of tracked noise is typically much lower and it does not follow the same trend. An example is shown in Figure 5.5. This knowledge can be leveraged to filter noise in the particle data sets. In particular, low intensity particles close to the imaging probe are searched for.

As shown in Figure 5.5 the particle intensity data is spatially averaged on intervals of 10 mm in depth (z). The resulting mean intensity distribution is expected to be monotonically decreasing with object distance z. This is indeed observed in the nominal case presented in Figure 5.5(a). If instead noise is reconstructed close to the probe, the intensity distribution includes a low for small values of z, which rises quickly when true particles are tracked. An example of such a case is given in Figure 5.5(b). To filter the low intensity tracks close to the CVV probe, the locally averaged mean intensity data is scanned for a positive gradient $\frac{dI}{dz}$ close to the velocimeter. If a minimum threshold is exceeded, a cut-off value is defined eliminating data close to the velocimeter.

Beyond the selected cut-off, noise affected data will still be present in the dataset. Assuming that in the well seeded region the relative share of true particles is greater, these ghost tracks can be detected by the statistical data filters discussed hereafter.

Confidence Interval Filter

Perhaps the most straight forward filtering strategy is the definition of the confidence interval, usually defined by a mean quantity and a range specified by the standard deviation. Filtering exemplary by the velocity, u_i, each measurement can be decomposed into a mean $\overline{u}_i$ and a fluctuating component u_i',

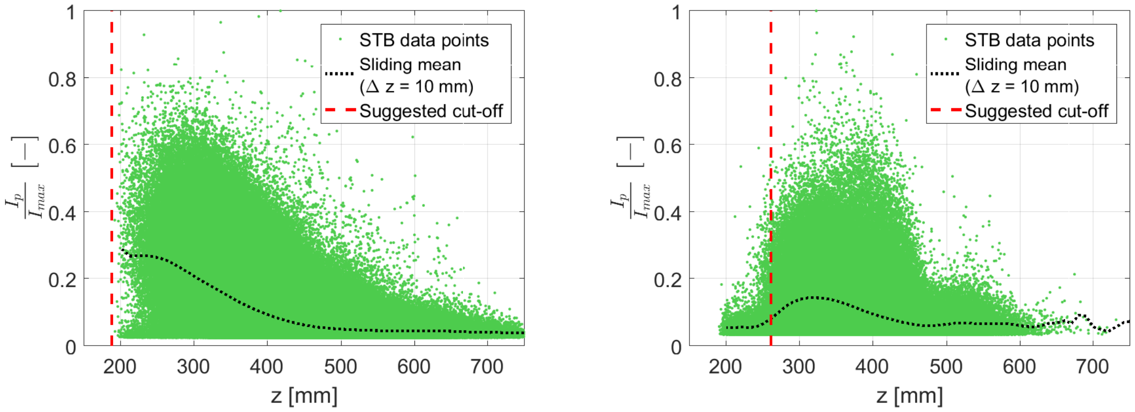

(a) Nominal dataset

(b) Noisy dataset

Figure 5.5: Particle intensity distribution in depth. Probe located at $z = 0$ mm.

$$u_i = \overline{u}_i + u_i' \tag{5.1}$$

Where the mean is defined by,

$$\overline{u}_i = \frac{1}{N} \sum_{n=1}^{N} (u_i)_n \tag{5.2}$$

Similarly, the standard deviation σ_u, known as the square root of the second central statistical moment, the variance is defined as,

$$\sigma_u = \sqrt{\frac{1}{N-1} \sum_{n=1}^{N} (u_i - \overline{u}_i)_n^2} \tag{5.3}$$

The standard deviation indicates the degree of dispersion of the data around its mean, and thus, it functions as an indicator for the turbulence level present in a flow.

Assuming the measured quantity is normally distributed, known confidence intervals can be defined based on statistical knowledge. For instance, the 67 % confidence interval is established by the $\pm\sigma_u$ interval around the mean. Employing the confidence interval filter is straight forward and computationally inexpensive. Yet, it will be biased by the relative amount of outliers contained within a certain dataset.

Universal Outlier Detection

Instead of the standard deviation based confidence interval filter, Westerweel and Scarano (2005) introduced a median based filter, specifically dedicated to PIV data. Instead of the mean, this filter considers the median as a reference quantity. It attains a universal character by normalisation of the residuals with the median residual, universality implying the filter works equally well in highly turbulent and in laminar flow regions.

$$r_0^* = \frac{|u_i - u_{i_m}|}{r_m + \epsilon} \tag{5.4}$$

The nominator in Equation (5.4) describes the definition of the velocity residual r_i based on velocity median u_{i_m}, and r_m in the denominator represents its median value. The additional parameter ϵ specifies a minimum acceptable fluctuation level in the measurement data.

Originally the median based outlier detection was dedicated to vector fields. It may however also be used for ensemble data sets instead. For the presented data in Chapters 6 and 7, it can for instance be applied for the particle data within each grid volume.

Comparison

The first two data filters, namely the velocity range and the close-distance intensity filter, are applied to all datasets. For the latter two filters, namely the confidence interval filter and the universal outlier detection, a choice is to be made. As described earlier, the filters shall remove noise efficiently, without eroding the dataset. To benchmark the two candidates, the flow downstream of the left calf is analysed.

Three cases are considered: first, the unfiltered dataset. Second, the application of the confidence interval filter with two passes and an acceptance level of 3σ around the mean. Third, two passes of the universal outlier detector with a threshold level of $r_{thr} = 2.5$ and an acceptable fluctuation level of 0.2. The two filters are applied during the ensemble averaging process inside a fluid cell of $20 \times 20 \times 20$ mm^3. The averaging process is detailed in Section 5.3.2. The comparison of the three cases is shown in Figure 5.6.

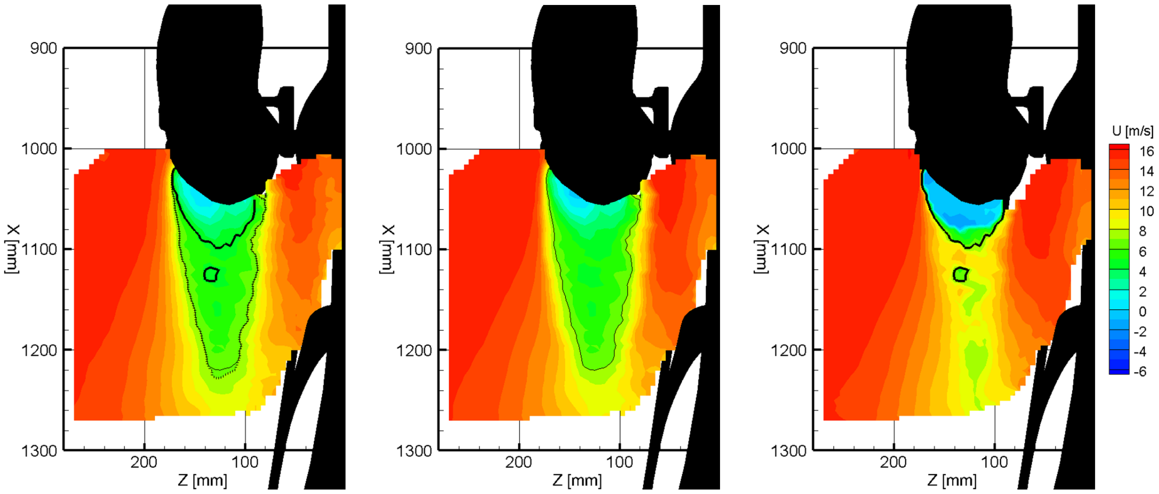

(a) Unfiltered. (b) Mean-σ filter. ($\pm 3\sigma$) (c) Median filter. ($\epsilon = 0.2$, $r_{thr} = 2.5$)

Figure 5.6: Comparison of data filters for particle track data. Sample case shows time-averaged flow past the shank of the stretched left leg evaluated from $5{,}000$ observations. Black contour lines show iso-contours of $u = 7$ m/s. Dotted contour corresponds to unfiltered data, thin solid line refers to mean-σ filter and thick solid line is representative of the median filter. Both filters contain two passes.

The raw data in Figure 5.6(a) shows a clear wake region with a velocity deficit downstream of the calf, a high velocity region outboard, and a fast stream inside of the calf close to the bike. The last of these three regions includes a minor degree of noise.

Applying the confidence interval filter with the specified parameters, the noise near the bike is slightly reduced, and the wake shape is maintained. Comparing the iso-contour of $u = 7$ m/s, it is seen that the wake is shortened by a fraction.

A peculiar behaviour of the median filter can be observed in Figure 5.6(c). A shrinkage of the wake region is observed, underpredicting the velocity deficit. It can be argued that the filter parameters are set too tight, and consequently, a relaxation of those will result in a less severe alteration of the flow features. There is however another explanation for the observed wake reduction: the calf wake is comparable to a two-dimensional cylinder wake. At the present Reynolds number, a periodic vortex shedding is expected to occur at the calf. Therefore, the velocity distribution of the wake's shear layer features a bimodal shape with a strong velocity deficit and a high value near the free stream velocity. In the convergence analysis in Section 5.3.3 it is highlighted, that more tracers are reconstructed in the laminar flow regions as compared to the turbulent domains. Thus, the median value in the velocity distribution of the oscillating wake is biased towards the higher velocities. As a consequence, the wake size is underestimated. While the application of the median filter appears to be effective in removing noise, its bias is too severe and thus, the more moderate confidence interval filter is applied as an outlier detector.

5.3.2. Grid Conversion

The data resulting from Lagrangian particle tracking is unstructured. For flow field analysis it is convenient to store velocity data on a structured grid. This greatly simplifies the evaluation of spatial gradients for instance. A range of averaging and interpolation techniques is available to structure the scattered particle data. It is stressed that for the present study a computationally efficient mapping technique is sought, enabling fast handling of large data sets. In other applications the computational demands may be less relevant, but high spatial resolution may be of greater importance, yielding a different conclusion on the conversion method of choice.

A recent work on different ensemble averaging techniques dedicated to 3D PTV data is published by Agüera et al. (2016). The reference technique in this work is the so called 'top-hat' filter, a strict averaging of an ensemble dataset. The advantage of such a filter is its simplicity and the resulting computational efficiency. For the top-hat filter the ensemble average is evaluated by,

$$\overline{u}_a = \frac{1}{N}\sum_{i=1}^{N} u_i \tag{5.5}$$

with $\overline{u}_a$ being the approximated mean velocity of N instantaneous measurements u_i in a fluid cell a. The fluid cell can be of arbitrary shape. The most simple solution may be a cubic cell of characteristic length l_V. If high spatial resolution is desired in a specific direction, anisotropic cells may be preferred. Other shapes can be spherical cells, which have the favourable characteristic of strictly limiting the maximum distance of a data point to the cell centre.

The finite cell size implies a spatial averaging of the scattered particle data. To avoid spatial modulation of measurement data, the cell size must be sufficiently small. Reducing the cell size results however in less data samples per cell, N. The number of samples per cell is driving the uncertainty ϵ_u.

$$\epsilon_u = \frac{k\sigma_{\overline{u}}}{\sqrt{N}} \tag{5.6}$$

k represents the coverage factor of a normally distributed quantity, in this case the velocity u with standard deviation $\sigma_{\overline{u}}$ and N number of uncorrelated samples. It must be stressed that the number of uncorrelated samples for time-resolved PTV data does not correspond to the number of acquired images. First of all, there is no guarantee that there is a tracer particle inside a fluid cell at every time instance, even for densely seeded flows. Secondly, for unsteady flows with a certain characteristic time scale, flow samples are correlated in space and time. To this end the integral time scale T_I of the flow of interest can be estimated. The number of uncorrelated observations N_{eff} may subsequently be estimated as the fraction of the acquisition period T_a over the integral time scale.

$$N_{eff} = \frac{T_a}{T_I} \tag{5.7}$$

For a desired uncertainty level ϵ_u and a known fluctuation level $\sigma_{\overline{u}}$ of the measurement quantity a minimum number of samples within a cell, respectively a minimum number of uncorrelated images can be defined. Assuming a cubic shape of the fluid cell, and a homogeneous seeding concentration C, the cell length may be no smaller than,

$$l_V = \sqrt[3]{\frac{N_{min}}{N_{eff} \cdot C}} \tag{5.8}$$

The cell length provides insight on the time-averaged dynamic spatial range, which is estimated by,

$$DSR = \frac{L}{l_V} = L\left(\frac{N_{eff} \cdot C}{N_{min}}\right)^{\frac{1}{3}} \tag{5.9}$$

Where L is the longest dimension of the global measurement domain.

The top-hat filter describes the most simple averaging approach. A more accurate average can be obtained when using a Gaussian weighting function which weighs the contribution of a data point to the cell average based on its distance to the cell centre. The method is only marginally more expensive as it requires the evaluation of the cell centre point distance and the weighting coefficients.

Assuming a sufficient number of available samples, the scattered measurement data inside a fluid cell can be approximated by the fit of a polynomial function as suggested by Agüera et al. (2016). In the three dimensional case this yields a surface of e.g. the velocity u as function of the coordinates (x, y, z). In the case of a second order polynomial fit, ten polynomial coefficients a_i need to be evaluated:

$$\overline{u}_a = a_0 + a_1\Delta x_i + a_2\Delta y_i + a_3\Delta z_i + a_4\Delta x_i^2 + a_5\Delta x_i\Delta y_i + a_6\Delta y_i^2 + a_7\Delta x_i\Delta z_i + a_8\Delta y_i\Delta z_i + a_9\Delta z_i^2 \quad (5.10)$$

The resulting system of equations can be solved for the coefficients a_i. Such an approximation of the average cell velocity may be even more accurate as it possesses the ability of modelling spatial gradients within a fluid cell. Yet, it requires the evaluation of a linear system of equations for every cell and thus, it makes the averaging procedure more expensive.

For the present study, the ensemble average filter is preferred due to its simplicity and efficiency in the processing of large data sets. For detailed analysis of flow features the use of the presented Gaussian and polynomial fit is expected to yield slightly more accurate results.

5.3.3. Data Convergence

The flow measurements described in the present report all target the evaluation of the time averaged velocity field. Given the complex and turbulent character of the measured flow, it is essential to know at which point the mean velocity measurements can be considered statistically converged. While insufficiently long measurement sequences may result in a biased velocity field, excessive data recording yields unnecessarily big data sets and consequently extensive processing times.

Several parameters can be identified which affect the convergence of the time averaged velocity components. First and foremost, the nature of the flow is anticipated to be decisive for convergence speeds. While in a laminar flow region with low fluctuation levels, measurement data may converge rapidly, the same quantity will converge considerably slower in a turbulent wake region with high velocity standard deviation. Perhaps even more intriguing, the velocity measurement near the shear layer of an oscillating wake (vortex shedding) may keep oscillating, given that laminar, high streamwise flow velocities will alternate with low speed, turbulent periods in time. Therefore, the subsequent convergence analysis will focus on these three characteristic regions: laminar flow regions, turbulent wake areas, and the boundaries of the two zones.

The sample of the calf wake is used once more as a test case for the convergence analysis. Three ‘probes’ are placed in the respective flow regions as indicated in Figure 5.7.

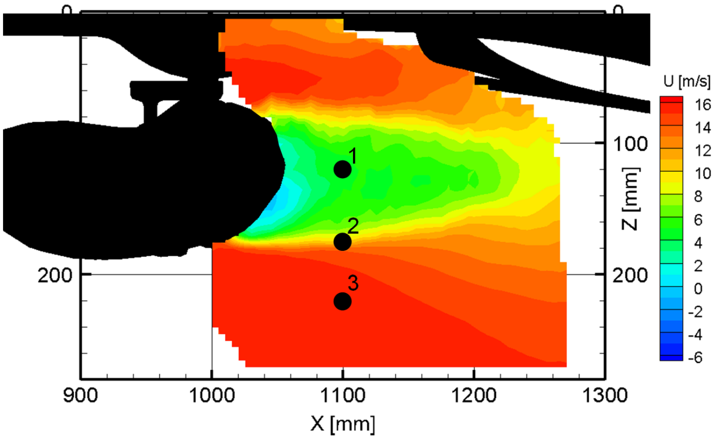

Figure 5.7: Contour plot of time-averaged streamwise velocity u in LHS shank wake, including virtual probe locations to assess statistical convergence of mean velocity components.

Secondly, the number of available data samples is expected to play an important role. The more data is available, in the particular case the more images are processed, the faster the mean quantities are expected to converge. Given the spacial averaging strategy outlined in Section 5.3.2, the data set that is averaged in a fluid volume can be adjusted by the selection of the cell size. However, small fluid volumes are desired to limit the extent of spatial averaging and to obtain a dense velocity vector field. Still, enlargement of the cell elements may be a parameter of choice to drive the convergence speed forward. Vice versa, if computational time is spare, one may process more of the available data to allow for a finer grid resolution.

To complicate the analysis, there is a link between the nature of the flow and the observed seeding density which can be appreciated from Figure 5.8. The figure shows the accumulated and the normalised seeding concentration in the three indicated probe locations, for a range of cell sizes. It can be seen that the seeding density is greater in laminar flow regions, whereas turbulent flow domains experience lower tracer particle concentration. For the shown example there is one order of magnitude difference in the number of data points in the laminar probe location as compared to the probe inside the wake region.

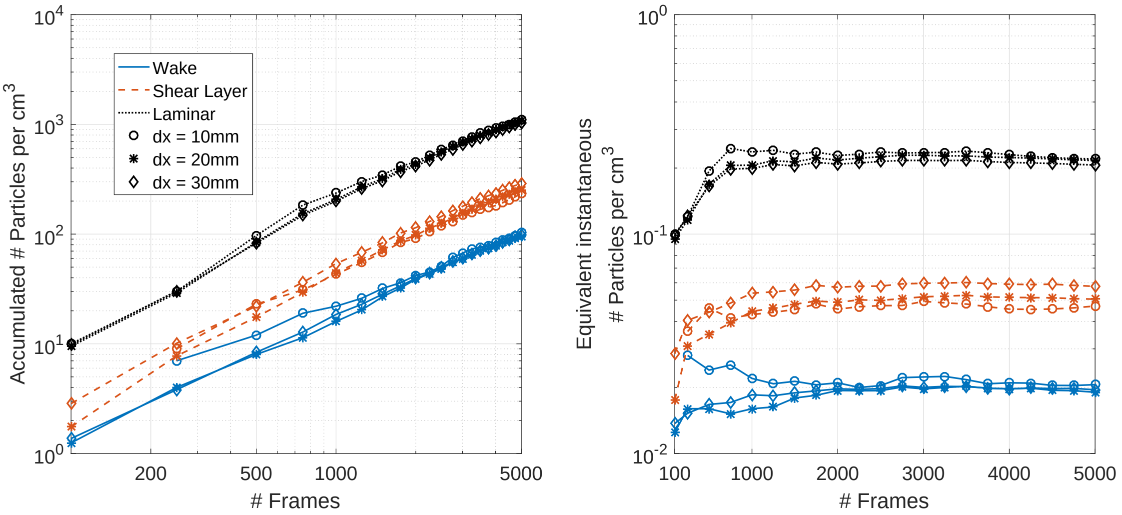

(a) Accumulated concentration (b) Normalised concentration

Figure 5.8: Accumulated and normalised seeding concentration for the probe locations indicated in Figure 5.7.

To assess the effects of the identified parameters on the statistical convergence of the mean velocity components, the following analysis is carried out: the flow around the cyclist's shank of the stretched (LHS) leg is considered as a representative sample, given that a clear wake flow with significant turbulence level can be identified, neighboured by a high-speed, laminar flow region as shown in Figure 5.7. Three 'probes', in the form of individual fluid volumes are placed in the flow, such that there is one probe each in the laminar, the turbulent and the transitional region.

The sizes of the probes are varied, with the characteristic length of the square fluid volume ranging from 10 up to $30\,\mathrm{mm}$ in uniform steps of $10\,\mathrm{mm}$. The mean velocity components are sampled every 250^{th} time step, which is equivalent to increments of 250 images.

Figure 5.9 shows the convergence trends of the streamwise mean velocity component for the three probe locations and sizes. In the freestream region the data converges rapidly. The estimated streamwise velocity after $1,000$ images is within 1% of the estimated value after analysing $5,000$ frames. There is no appreciable difference between the cell sizes, given that the spatial velocity gradient is relatively small for this probe.

In the wake region, the convergence is seen to be slower. For the two larger cells the data is considered stable beyond $3,000$ frames, while for the smallest $1\,\mathrm{cm}^3$ cell, the estimated value keeps oscillating around the slightly negative mean.

A peculiar trend is observed when considering the probe in the shear layer. For the three considered cell sizes, the mean velocity appears to stabilise rapidly ($\geq 2,000$ images). However, each cell size converges to a different velocity. The spatial gradient in the seeding concentration across the calf wake established in Figure 5.8 indicates that there is more data in the high-speed, laminar flow regions. Therefore, enlarging the fluid cell size will enclose a larger share of fast tracers as compared to slow particles closer to the wake flow. Thus, a bias towards higher velocities is observed as the fluid cell size is enlarged.

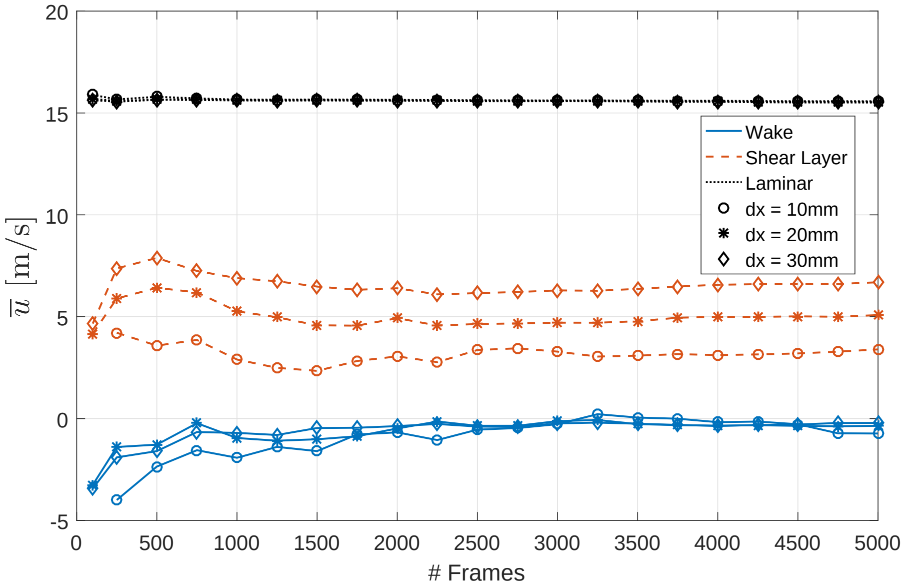

Figure 5.9: Convergence plots for the three probes illustrated in Figure 5.7 for the streamwise velocity component and the indicated probe sizes.

The comparison of the probes inside the wake and in the shear layer highlights that the fluid cell size cannot be too small, as too much data is required to reach a converged mean velocity. Yet, increasing the cell size results in a spatial modulation of the data as seen in the probe at the shear layer. For the large-scale demonstration presented in Chapters 6 and 7, a grid element size of $20 \times 20 \times 20\,\text{mm}^3$ is seen to be sufficiently large to provide reliable time-averaged velocity data in regions with low seeding concentration while limiting the spatial modulation of the data to a minimum.

To evaluate the resulting uncertainty of the mean-velocity measurement for the selected cell size, the integral time-scale of the described wake flow is estimated. A first analytical estimate of the vortex shedding frequency of the presented calf wake is based on the expected Strouhal number, the shank diameter and the freestream velocity. For the present Reynolds number regime, a Strouhal number of $St \approx 0.2$ is anticipated. The shank is approximately $d_{shank} = 10\,\text{cm}$ wide. Thus, the characteristic frequency is expected to be given by,

$$f_I = \frac{St \cdot U_0}{d_{shank}} = \frac{0.2 \cdot 14.0\,\text{m/s}}{0.1\,\text{m}} = 28.0\,\text{Hz} \tag{5.11}$$

The inverse of the observed shedding frequency can then be used as an estimate of the integral time scale of the flow. Instead, one can make an autocorrelation analysis of the measured velocity signal to estimate the integral time scale. The autocorrelation coefficient is defined as,

$$\rho(\tau) = \frac{\overline{u'(t)\,u'(t+\tau)}}{\overline{u'^2}} \tag{5.12}$$

The autocorrelation coefficient is evaluated for the streamwise velocity component measured by the probe inside the wake as shown in Figure 5.10.

The autocorrelation coefficient in Figure 5.10 provides an indication of the integral time scale of the velocity signal. Assuming the measurements are uncorrelated for a value of $\rho < 0.2$, the corresponding integral time scale equates to $T_I = 0.02\,\text{s}$ and thus, a frequency of $50\,\text{Hz}$. This frequency is higher than the anticipated frequency of $28\,\text{Hz}$ based on the expected Strouhal number. The difference is caused by the arbitrary selection of the threshold on ρ. Other parameters which may influence the shedding frequency are the actual shape of the leg and the proximity to the bicycle.

In the specific measurement $5,000$ samples are acquired at $758\,\text{Hz}$ equating to an acquisition period of $T_a = 6.6\,\text{s}$. Assuming a characteristic frequency of $50\,\text{Hz}$ in the wake region as evaluated above, $N_{eff} = 330$ uncorrelated samples are taken during one acquisition. Therefore, the uncertainty defined in Equation (5.6) scales with $330^{-0.5} \approx 5.5\%$ for the mean flow component in the turbulent wake region for an isolated measurement. It is noted that there is a considerable amount of overlap present

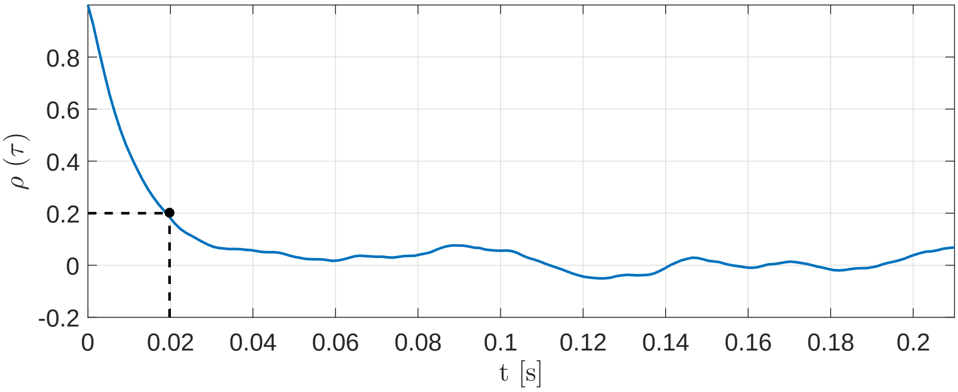

Figure 5.10: Autocorrelation coefficient evaluated on the streamwise velocity component measured in the shank wake (Probe ‘1’ in Figure 5.7). Point marker of $\rho = 0.2$ given as indication for integral time scale.

between two adjacent sub-volume measurements, given that the displacement of a subsequent measurement position is limited by the smallest cross section of the conical measurement domain, close to the velocimeter (see discussion in Section 5.2, respectively illustration of measurement domain in Figure 4.13). Consequently, on the interior domain where turbulent flow regions are present, the overlap of measurement volumes will benefit the measurement uncertainty as more uncorrelated samples are obtained.

5.4. Flow Analysis Techniques

Following the sequence of image pre-processing (Section 5.1), particle tracking (Section 5.2) and post-processing (Section 5.3) a structured set of time-averaged velocity data is obtained. Different means of flow field visualisations are chosen to present the conducted measurements in the results section in Chapter 7. In the following, the selected analysis techniques are defined briefly.

It is stressed that only the time-averaged velocity is investigated, and the analysis of the instantaneous measurements in the sub-volumes is omitted. Therefore, the following discussion may not necessarily apply to instantaneous flow fields.

5.4.1. Streamlines

Flow field visualisations are not trivial. Whereas contour plots provide insight on the magnitude of a certain variable, streamlines provide a means to indicate the direction of a fluid flow. By definition, a streamline is tangent to the flow direction in any point. That is,

$$\frac{w}{v} = \frac{dz}{dy} \tag{5.13a}$$

$$\frac{u}{w} = \frac{dx}{dz} \tag{5.13b}$$

$$\frac{v}{u} = \frac{dy}{du} \tag{5.13c}$$

For steady flows streamlines are the exact representation of pathlines. Equation (5.13) contains the definition of the true streamline in 3D space. Selecting any of the three equations in Equations (5.13a) to (5.13c), surface-streamlines are obtained in the plane of interest, describing the tangent flow direction in the selected plane. Likewise, the tangent velocity component can be evaluated on any other oriented surface, resulting in surface-streamlines on any body of interest.

5.4.2. Velocity Gradient

The evaluation of streamlines as detailed above requires the determination of spatial velocity gradients. For the structured, discrete velocity data, finite difference schemes provide approximations of the spatial gradients. Foucaut and Stanislas (2002) present a study on the accuracy of a series of finite difference schemes in the evaluation of derivatives in PIV data. The study concludes that the second-order central difference scheme provides satisfactory accuracy of derivatives and that higher order schemes do not yield significant improvements of the accuracy of the computed derivatives.

The second order central difference scheme can be formulated as,

$$\frac{du}{dx_j} \approx \frac{u_{i+1} - u_{i-1}}{2\Delta x_j} \tag{5.14}$$

Gradients are not only used for computation of streamlines but also for evaluation of vorticity terms as detailed in the following.

5.4.3. Vorticity

Vorticity is defined as the curl of the velocity vector field and as such the vorticity vector contains information of the fluid circulation. Mathematically, the vorticity $\vec{\omega}$ is defined by,

$$\vec{\omega} = \nabla \times \vec{u} = \begin{Bmatrix} \frac{\partial w}{\partial y} - \frac{\partial v}{\partial z} \\ \frac{\partial u}{\partial z} - \frac{\partial w}{\partial x} \\ \frac{\partial v}{\partial x} - \frac{\partial u}{\partial y} \end{Bmatrix} \tag{5.15}$$

The circulation of the velocity field can indicate presence of vortices. The definition of vorticity in Equation (5.15) purely based on velocity gradients cannot distinguish shear layers from vortices. For characterisation of vortices, other criteria such as the *Q-criterion* and the λ_2-definition are more suitable.

5.4.4. Q-Criterion

The Q-criterion as well as the λ_2 criterion presented hereafter both utilise the velocity gradient tensor D_{ij}, which can be decomposed into a symmetric tensor S_{ij} and a skew-symmetric tensor Ω_{ij}.

$$D_{ij} = \frac{\partial u_i}{\partial x_j} = S_{ij} + \Omega_{ij} \tag{5.16}$$

The symmetric and skew-symmetric tensors are defined as follows,

$$S_{ij} = \frac{1}{2}\left(\frac{\partial u_i}{\partial x_y} + \frac{\partial u_j}{\partial x_i}\right) \tag{5.17a}$$

$$\Omega_{ij} = \frac{1}{2}\left(\frac{\partial u_i}{\partial x_y} - \frac{\partial u_j}{\partial x_i}\right) \tag{5.17b}$$

The Q-criterion is based on the second invariant of the velocity gradient tensor, labelled as Q. The latter can be expressed through the symmetric and skew-symmetric tensors S_{ij} and Ω_{ij}.

$$Q = \frac{1}{2}\left(||\Omega_{ij}||^2 - ||S_{ij}||^2\right) \tag{5.18}$$

The second invariant Q describes the local balance of vorticity magnitude and shear strain rate. For positive values of Q, the circulation is stronger than the shear and vice versa. Thus, a positive value of Q indicates the presence of a vortex, whereas negative values of Q indicate presence of shear layers.

5.4.5. λ_2-Criterion

The λ_2-criterion is based on the eigenvalues of $\left(S_{ij}^2 + \Omega_{ij}^2\right)$. While it is very similar to the Q-criterion, the λ_2-criterion is expected to be more suitable in the prediction of vortices with a strong external strain (Jeong and Hussain, 1995). Ordering the three eigenvalues of $\left(S_{ij}^2 + \Omega_{ij}^2\right)$ by $\lambda_1 \leq \lambda_2 \leq \lambda_3$, a negative value of the second eigenvalue λ_2 is indicative of a local pressure minimum entailing a vortex.

6

Experimental Apparatus and Procedures

The working principles of Coaxial Volumetric Velocimetry are presented in Chapter 4. The discussion in Chapter 4 further contains results of the first two validation experiments which are carried out. The experimental apparatus and the corresponding measurement procedures presented here in Chapter 6 solely consider the final large-scale demonstration experiment. In this experimental campaign the near flow field around a time-trialling cycling mannequin is analysed. The test model, which is a full-scale representation of Dutch Olympic silver medallist and winner of the 100th edition of the Giro d'Italia, Tom Dumoulin, is introduced in Section 6.1. The measurements are conducted at the Open Jet Facility[1] of TU Delft, see Section 6.2. The experimental setup with details on the various subsystems is shown in Section 6.3. The actual acquisition procedure, including details on calibration of both, imaging system and robotic arm, is explained in Section 6.4. The discussion of the experimental apparatus and procedures in this chapter provides the necessary information to study the flow measurements in Chapter 7.

6.1. Test Object

For the purpose of test repeatability a rigid mannequin is placed in the test section of the Open Jet Facility. The use of a full-scale replica instead of human athletes further relaxes the safety requirements for testing with laser illumination and Helium Filled Soap Bubbles. The mannequin was additively manufactured ('3D-printed') from a thermoplastic polyester, following a 3D-scan of Olympic silver medallist Tom Dumoulin[2]. The mannequin is in time-trial position, with a fixed asymmetric leg position. That is, the left leg is pointing down with a $75°$ crank angle θ, as indicated in Figure 6.1(b). The characteristic dimensions of the mannequin are summarised in Table 6.1.

Table 6.1: Characteristic mannequin dimensions (Terra et al., 2016a).

Name	Symbol	Dimension	Unit
Crank angle	θ	75	[°]
Hip width	HW	365	[mm]
Shoulder width	SW	380	[mm]
Hip location, x	hip_x	180	[mm]
Hip location, y	hip_y	850	[mm]
Lower leg length	$A-B$	475	[mm]
Upper leg length	$B-C$	460	[mm]
Torso length	$C-D$	600	[mm]
Upper arm length	$D-E$	326	[mm]
Lower arm length	$E-F$	290	[mm]

---

[1] hereafter referred to as OJF

[2] For the interested reader, there is a video documentation capturing the scanning, manufacturing and initial testing of the full scale mannequin available online: `http://tinyurl.com/y8drkxsv` (Delft University of Technology, 2016).

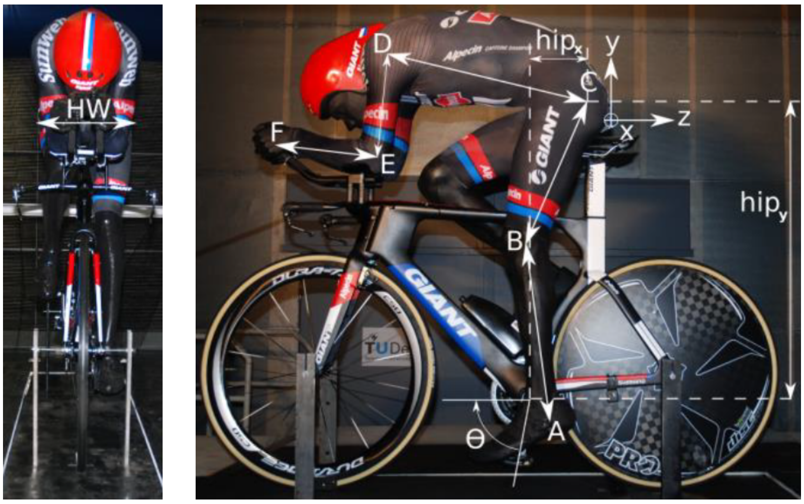

(a) Front view (b) Side view

Figure 6.1: Cyclist model and bike with characteristic dimensions. Duplicated from (Terra et al., 2016a).

Based on the cyclist's torso length, the measurements are carried out at a Reynolds number of 5.5×10^5.

The bike used is a *Giant Trinity Advanced Pro* frame, a *Shimano DuraAce C75* front and a *Pro Textreme* disc rear wheel, both equipped with 25 mm tubular tires. The bike is rigidly supported at the front and rear axles, with the supports connected to a six-component force balance. The balance is further attached to a turntable, allowing for variations in yaw angle. Though, all measurements presented in this thesis are taken at straight ahead conditions. The complete model is placed on a rigid, wooden floor, meaning that also the wheels are kept stationary during the measurements. The floor is spanning 3.02 m in width and 4.88 m in streamwise direction, being placed 20 cm above the lowest point of the contraction exit to scoop away the boundary layer developing in the wind tunnel contraction.

The mannequin is dressed with a long sleeve *Etxeondo* time trial suit along with a *Giant* time trial helmet, as used by *Team Giant Alpecin* during the 2016 season. Bright parts on suit and helmet are painted black to limit optical reflections of the high intensity laser light employed in the PTV setup.

6.2. Open Jet Facility (OJF)

To conduct the flow measurements around the full-scale cyclist, the model described in Section 6.1 is placed in the Open Jet Facility at the High Speed Laboratories of TU Delft. The room including the test section spans 13 m by 8 m in width and height, respectively (Delft University of Technology, 2017). The atmospheric closed-loop, open jet wind tunnel which is shown in Figure 6.2, provides a contraction ratio of $3{:}1$ with an octagonal exit section of $2.85 \times 2.85\,\text{m}^2$. The emanating shear layer contracts the free-stream region with a semi-angle of 4.75° in the streamwise direction (Lignarolo et al., 2014).

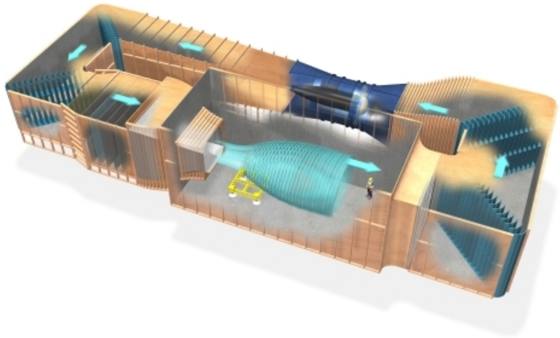

Figure 6.2: Schematic view of the *Open Jet Facility* at TU Delft (Delft University of Technology, 2017).

The fan controlling the flow speed is driven by a 500 kW electrical motor. The usable wind speed range of the tunnel reaches from 4 to 35 m/s. During the campaign the wind speed is fixed at 14 m/s. Downstream of the test section, a cooling mesh is present such that the air temperature is maintained constant and independent of the flow speed.

The turbulence intensity of the free stream is reported with 0.5% by Lignarolo et al. (2014). Though, this does not consider the placement of the seeding generator which is expected to raise the turbulence intensity as discussed in Section 6.3.1.

6.3. Measurement System

Section 6.1 describes the experimental model whose flow is studied, whereas Section 6.2 focuses on the wind tunnel facility. In this section the installation of the coaxial velocimetry system introduced in Chapter 4 is discussed. Key components of the complete PTV system contain the seeding rake for tracer particle generation, the light source for illumination, the actual imaging system, namely the compact velocimeter, as well as the robotic arm which supports and controls the position and orientation of the camera system. The arrangement and the influence of these components, which can all be seen in Figure 6.3, on the flow measurements is discussed in the subsequent sections.

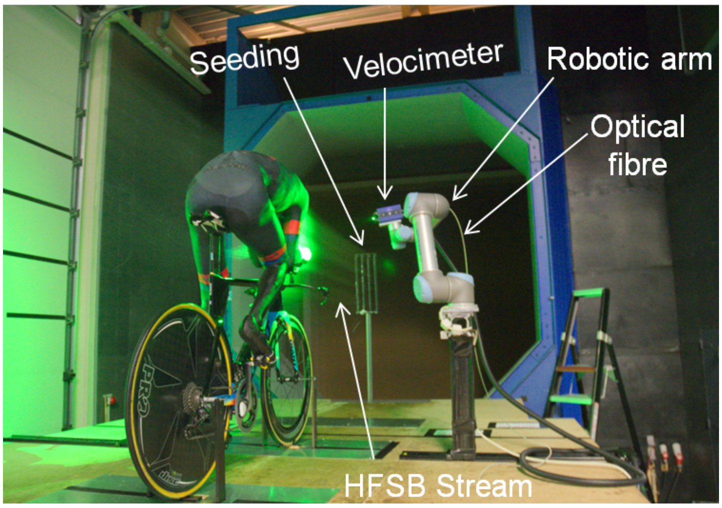

(a) Overview with components labeled

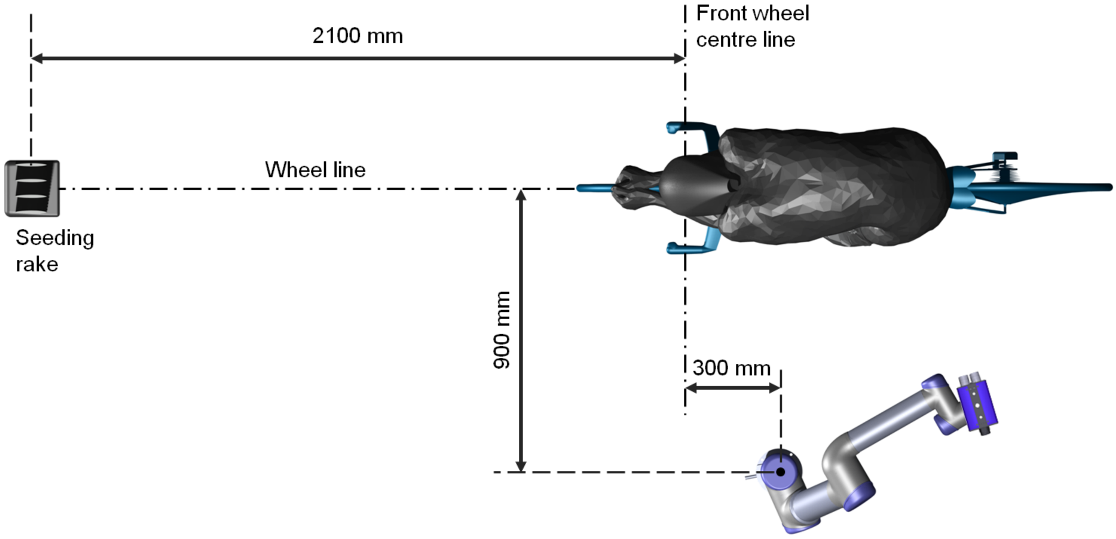

(b) Top view schematic with main dimensions

Figure 6.3: Overview of the measurement setup, including the test object described in Section 6.1, the seeding rake (Section 6.3.1) and the robotic arm with the coaxial velocimeter (Section 6.3.2). The laser head cannot be seen, as it is placed underneath the wooden table.

6.3.1. Seeding Generator

To dispense HFSB tracers in the airflow, a novel seeding rake is installed at the exit of the wind tunnel contraction, approximately 2.1 m ahead of the front wheel centre line as shown in Figure 6.3. The rake contains 80 nozzles, distributed over four wings with each nozzle producing $25,000$ tracers per second at nominal working conditions resulting in a total production rate of 2×10^6 bubbles/s. The nozzle pitch is 5 cm in lateral, and 2.5 cm in vertical direction, yielding a wing system of 15×47.5 cm^2 cross section. The bubble generation is controlled by a digital Fluid Supply Unit (FSU) provided by *LaVision*. Stable tracer production is observed at pressures of 1.8 bar for Helium, 3.0 bar for air and 2.7 bar for soap.

With the specified settings, a particle image density of $1.0 - 1.5\%$ ppp is attained for a free field of view of the CVV probe. The physical particle size is not measured, but it is reported with 400 µm diameter in literature (Scarano et al., 2015). Estimating the particle image size at a nominal object distance of 40 cm to the velocimetry probe based on Equation (4.4), it is found that the particle images are diffraction limited with a particle image diameter of $d_{diff} = 10.4$ µm and $d_{geo} = 4.1$ µm. Thus, a particle imaged at this distance spans approximately 2.3 pixels in diameter.

Given the properties of the HFSB seeder, the theoretically expected seeding concentration is worked out. Assuming a single nozzle feeds a streamtube of constant cross section defined by the nozzle pitch, the seeding concentration is obtained as the fraction of tracer production $\dot{N}$, over volume flow rate $\dot{V}$. That is,

$$A_n = d_{z_n} \times d_{y_n} = 5\,\text{cm} \times 2.5\,\text{cm} = 12.5\,\text{cm}^2 \tag{6.1a}$$

$$\dot{V} = A_n \cdot U_0 = 12.5\,\text{cm}^2 \cdot 14\,\text{m/s} = 17,500\,\text{cm}^3\text{/s} \tag{6.1b}$$

$$C_{HFSB} = \frac{\dot{N}}{\dot{V}} = \frac{25,000}{17,500} \frac{\text{bubbles/s}}{\text{cm}^3\text{/s}} = 1.43\,\text{bubbles/cm}^3 \tag{6.1c}$$

The seeding rake is supported on a two-axes traversing system, which allows for lateral translations of up to one meter, as well as vertical translations of up to 1.2 m. The rake is supported from below by an aerodynamic fairing which houses the supply and return hoses for air, helium and soap which connect to the FSU.

The flow interaction of the seeding rake is quantified by means of a free stream measurement 2.0 m downstream of the wind tunnel contraction exit. The CVV probe is positioned perpendicular to the flow direction, which is seen to be the least intrusive condition, as analysed in Chapter 4. Evaluating the freestream measurement at 0.5 m distance to the probe indicates a turbulence intensity level of 1.9%. This measured turbulence level is approximately four times higher than the quoted reference level of the ‘clean’ OJF tunnel (Lignarolo et al., 2014).

6.3.2. Imaging and Robotic Control Unit

The velocimetry probe and the robotic arm are introduced in Section 4.2 already. The brief discussion here thus focuses only on installation and operation parameters of the robotic PIV system.

Imaging Probe

The technical specifications of the CVV probe are detailed in Table 4.1. For the demonstration experiment at 14 m/s freestream velocity, the active sensor size is reduced to 640×475 px^2 to accelerate the acquisition frequency up to 758 Hz. The probe’s cameras are controlled through `DaVis 8.4.0`, where the exposure time is set to 100 µs. The lens aperture is maintained at $f_\# = 8$.

Illumination

The illumination system for all experimental campaigns is introduced in Section 4.2.2. For the particular campaign, the pulse energy of the Quantronix Dawrin Duo Nd:YLF laser is set to 21 mJ with both laser pulses operating simultaneously. The laser head is installed centrally underneath the measurement table supporting the bike. The 4 m long optical fibre is guided through small holes in the measurement table towards the robotic PIV system. The lens configuration of the fibre coupler is equivalent to the setup described in Section 4.2.2.

Robotic Arm

Characteristics of the *Universal Robots - UR5* robotic arm are presented in Section 4.2.3. To cover the complete flow around the cyclist replica, the robotic arm is installed in two symmetric base positions, one on the left- and the other on the right-hand-side of the athlete. The base positions are chosen at a height of 65 cm, 90 cm lateral distance to the wheel line and 30 cm downstream of the front wheel centre line. The positioning and installation of the robotic arm on a short pole can be appreciated from Figure 6.3.

6.4. Acquisition Procedure

The usage of the presented measurement system is non-trivial, involving processes such as the geometrical calibration of the imaging system up to the positioning of the probe to minimise intrusiveness and/or light reflections in the images. Figure 6.4 presents an overview of the several steps which are involved in the acquisition procedure.

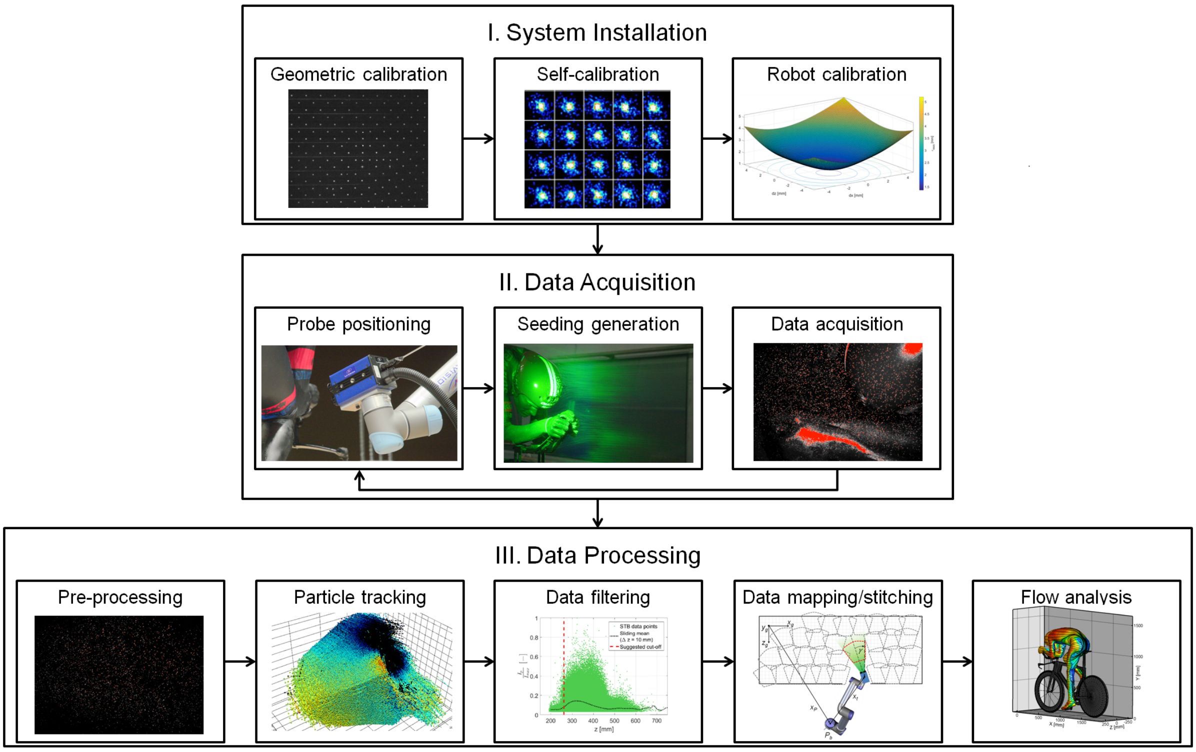

Figure 6.4: Flow chart of data acquisition process during experimental campaign. System installation and calibration at start of campaign only. Data acquisition is repetitive for the proposed robotic PIV approach. Processing is specific to the presented experiment.

The first group of activities in Figure 6.4 involves the system installation and calibration. Calibration procedures for the CVV probe and the robotic arm are detailed in Sections 6.4.1 and 6.4.2, respectively. Whereas the geometrical calibration of the velocimetry probe follows the well known pinhole calibration model (Soloff et al., 1997), the calibration of the robotic arm is specific to the proposed robotic measurement approach and the selected hardware components.

The novelty of the proposed robotic PIV approach is appreciated in the sequential acquisition procedure indicated in the second group of activities in Figure 6.4. The data recording strategy is defined in Section 6.4.3. It is important to realise that the indicated process is sequential and can be repeated hundreds of times without revisiting the preluding calibration stage.

The acquired data eventually requires customary data processing. The specific data reduction techniques are discussed in Chapter 5.

6.4.1. Optical Calibration

As outlined in the theoretical contents (Chapter 3) volumetric velocimetry systems relying on optical data require accurate calibration. Thus, a conventional pinhole-model calibration (Soloff et al., 1997) is typically followed by a further volume self-calibration as introduced by Wieneke (2008).

For the geometrical calibration, a *LaVision - Type 30* reference plate is used. A right-hand-side coordinate system is defined with the x- & y-direction corresponding to the horizontal and vertical component of the calibration plate plane. Consequently, the z-axis is defined perpendicular to the calibration plate. Using the *UR5* robotic arm, the imaging probe is placed centred in the xy-plane and parallel to the z-axis. The zero plane is defined at $z \approx 350$ mm distance measured from the camera housing. The exact offset is determined at a subsequent stage (Section 6.4.2) as it is a necessary quantity to achieve an accurate data mapping onto a global reference frame as described in Section 4.3.2. Additional calibration images are taken at ± 200 mm in z with respect to the zero-plane, where the camera translations are controlled using the robotic arm. Following the geometrical calibration, evaluation of disparity maps show maximum errors of 1.0 px at 40 cm distance from the camera.

To further improve the calibration accuracy, a volume self-calibration is performed. The maximum error in the resulting disparity map is reduced to 0.3 px at 40 cm distance to the camera.

On the corrected calibration, an Optical Transfer Function[3] is calculated which allows for particle reprojections from 3D-space to 2D-image coordinates (Schanz et al., 2012). The OTF is a key ingredient for the Shake-the-Box algorithm, and thus, a high quality transfer function is desirable.

6.4.2. Centre of Rotation Calibration

For a correct data mapping from the camera reference frame, as established in the geometrical calibration described in Section 6.4.1, to the desired global reference frame the offset between the centre of rotation of the *UR5* tool-head, as configured in the *UR5* software interface, and the origin of the camera reference frame needs to be known. As this distance is difficult to measure physically, an iterative procedure is chosen to estimate the relative position of the two points of reference. In the definition of the reference frames and the data mapping procedure in Section 4.3.2 the relative distance between the two axes systems is referred to as $\vec{x}_{cor}$.

A small number of reference points are placed on a reference surface. In the particular case seven stickers with the longest dimension within 1 mm are glued to a black, non-reflective plate as shown in Figure 6.5(a). The markers shall be sufficiently far apart, but can be randomly distributed.

Next, short image sequences of the reference plate are taken with the camera system from different positions and orientations. It proves useful to isolate rotations at first to eliminate one degree of freedom in the estimation of the vector $\vec{x}_{cor}$. That is, when applying for instance a pure yaw rotation, any vertical offset in the y-component of $\vec{x}_{cor}$ does not affect the transformation of the reconstructed points from camera to desired global reference frame. Thus, only two instead of three parameters need to be iterated which enhances the speed of the initial approximation of $\vec{x}_{cor}$. Similar reasoning applies to the pitch and roll rotations. More complex, combined rotations can subsequently be used to validate the findings for $\vec{x}_{cor}$.

As indicated, the reference points are reconstructed in the camera reference frame for all positions considered. It is chosen to apply Shake-the-Box tracking of the stationary markers, given that the same reconstruction method is used to follow the actual tracer particles in the flow measurements. This yields tracks of the reference points within the positional reconstruction uncertainty. A sample reconstruction of reference points is presented in Figure 6.5(b). The tracks are finally reduced to mean particle positions for each marker.

The mean particle positions are then transformed back to a desired reference frame, using the methodology outlined in Section 4.3.2 for a range of rotation offsets $\vec{x}_{cor}$. Using the isolated rotations yields a fast initial estimation of $\vec{x}_{cor}$ which is subsequently fine-tuned, iterating all three degrees of freedom. An error surface for a two degree of freedom iteration is illustrated in Figure 6.5(c). The location of the global minimum of the error surface provides the best estimation of $\vec{x}_{cor}$.

In the particular case, an accuracy level within 2.4 mm, measured in terms of standard deviation of 3D particle positions, is achieved. Considering the in-plane accuracy only, the positions are matched even better with 1.0 mm uncertainty. However, the out-of plane accuracy is lower, which can be attributed to the low tomographic aperture angle of the imaging system.

---

[3] hereafter referred to as OTF

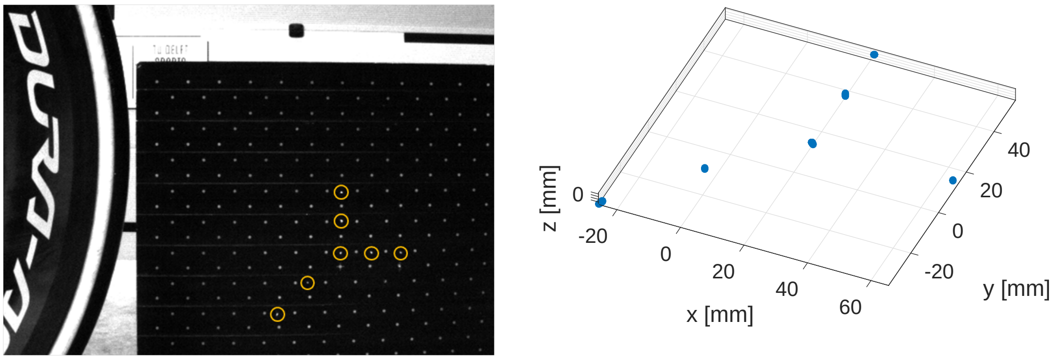

(a) Raw image with reference markers encircled. Note that calibration plate points are larger, resulting in increased in-depth uncertainty of point reconstructions.

(b) Marker tracks post STB reconstruction in camera reference frame.

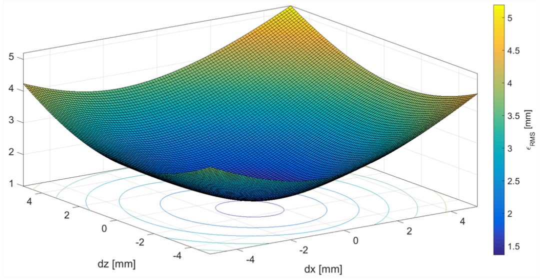

(c) 2D iteration for $\vec{x}_{COR}$

Figure 6.5: Stages and components of the centre of rotation calibration which is required for a correct coordinate transformation from camera- to global reference frame.

The outlined approach focuses on translational offsets only. Thus, it is assumed that there are no angular offsets in the tool alignment. Better results may be observed when correcting rotational misalignments as well. This will however yield three additional degrees of freedom, adding to the complexity and the time requirements of the calibration procedure. The accuracy obtained by consideration of the translational offsets only is deemed sufficient for the gross measurement scale of the full-scale cyclist flow measurement.

The iterated value for the relative distance $\vec{x}_{cor}$ is tabulated together with the positional uncertainties of the seven marker points in Table 6.2.

Table 6.2: Robotic arm - calibration mapping results. Two specifications are given for either measurement side, since an additional calibration error of 1.0 px, requiring a new geometrical calibration, was observed in camera four after movement of the measurement system to the right-hand-side of the cyclist.

Location	Name	Symbol	x	y	z	$\|\vec{x}\|$	Unit
LHS	Offset vector	$\vec{x}_{COR}$	0.0	18.5	411.5	411.9	[mm]
	Positional error	$\vec{\epsilon}$	0.53	0.82	2.14	2.35	[mm]
RHS	Offset vector	$\vec{x}_{COR}$	0.0	18.0	439.0	439.4	[mm]
	Positional error	$\vec{\epsilon}$	0.29	0.50	1.56	1.67	[mm]

6.4.3. Data Recording

During data acquisition all systems described in Sections 6.1 to 6.3 are to be controlled. In case of soap accumulation on the model, it needs to be cleaned to avoid reflections. The wind tunnel is to be maintained at the desired measurement speed. The actual measurement system as discussed in

Section 6.3 is the key system to be controlled during data acquisition. The sequential data recording procedure after calibration is as follows:

1. **Probe Positioning**
   The velocimeter is driven to its desired position using the *UR5* control panel or manual, collaborative probe placement.
2. **Field of View Validation**
   Snapshots are taken using full laser illumination to check the field of view for potential light reflections. If strong reflections are found, the probe positioning is reconsidered and a better viewing direction is iterated to minimise background noise, keeping in mind the aerodynamic interference of the measurement probe. Often, a small pitch and/or yaw rotation is found to improve image quality significantly as the resulting illumination is more oblique to the model surface.
3. **Position Recording**
   Once the probe is positioned, the tool position and orientation as provided on the *UR5* panel are recorded in a digital spread sheet.
4. **HFSB Generation**
   The tracer particle generation is initiated via the FSU. Sufficient quality and stability of the seeding stream are assessed by visual inspection.
5. **Data Acquisition**
   Image recording is initiated when the seeding quality is deemed satisfactory. $5,000$ images are recorded at a frequency of $758\,$Hz.
6. **Data Storing & Seeding Stop**
   The recorded images are stored after another visual inspection for image quality and seeding density. If the data quality is satisfactory, the seeding generation is paused. Otherwise, data acquisition is repeated.

The outlined process yields a repetition frequency of $2 - 3$ minutes between two subsequent measurements when operating with a single user and manual probe placement. A discussion on the streamlining of the data acquisition process to make it more suitable for industrial applications can be found in the recommendations presented in Chapter 8.

6.4.4. Data Processing

The recorded image data is processed as discussed in Chapter 5. The key elements of the processing chain are visualised in Figure 6.4 in the introduction to Section 6.4.

The raw particle images are pre-processed using a high-pass frequency filter, as described in Section 5.1. The filtered images are subsequently analysed by the Lagrangian particle tracking algorithm Shake-the-Box. Specific details on the parameters used for the particle tracking algorithm are given in Section 5.2.

Despite the robustness of the STB algorithm, the track data may still contain spurious tracks. Additional filtering techniques are applied to the particle track data as discussed in Section 5.3.

The particle tracking algorithm is evaluated in the reference frame of the velocimetry probe. The scattered particle tracks are subsequently mapped onto the global reference frame which is aligned with the freestream direction. Details on the data mapping and the definition of the reference frames are given in Section 4.3. The data of all measurement positions is first mapped to the global frame of reference. Subsequently, the complete scattered dataset is treated with the ensemble averaging approach discussed in Section 5.3.2 to evaluate the time-averaged velocity field on a structured grid. The grid features cubic cells of $20 \times 20 \times 20\,\text{mm}^3$ with an overlap of 75% yielding a velocity vector spacing of $5\,$mm for the time averaged flow field.

The observed mean flow field is then analysed with the tools presented in Section 5.4.

7

Results and Discussion

Results of the large-scale demonstration experiment are presented in this chapter. For more details on the data processing and the experimental setup Chapters 5 and 6, respectively can be conducted. The discussion of the results starts from the basic flow quantities such as the time-averaged velocity contours. The complexity is sequentially increased introducing streamline contours, vorticity fields and specific vorticity criteria such as the Q-criterion. The concluding discussion in Section 7.6 focuses on data in the wake where references from other studies are available in literature.

7.1. Time-Averaged Velocity Field

A representation of the time-averaged velocity field is presented in Figure 7.1. The visualisation shows a contour plane of streamwise velocity u in the centre plane ($z = 0$ mm). Surface streamlines in the centre plane are illustrated to provide insight on the mean flow direction. Lastly, an iso-surface of $u = 7$ m/s is included, indicating regions of decelerated flow.

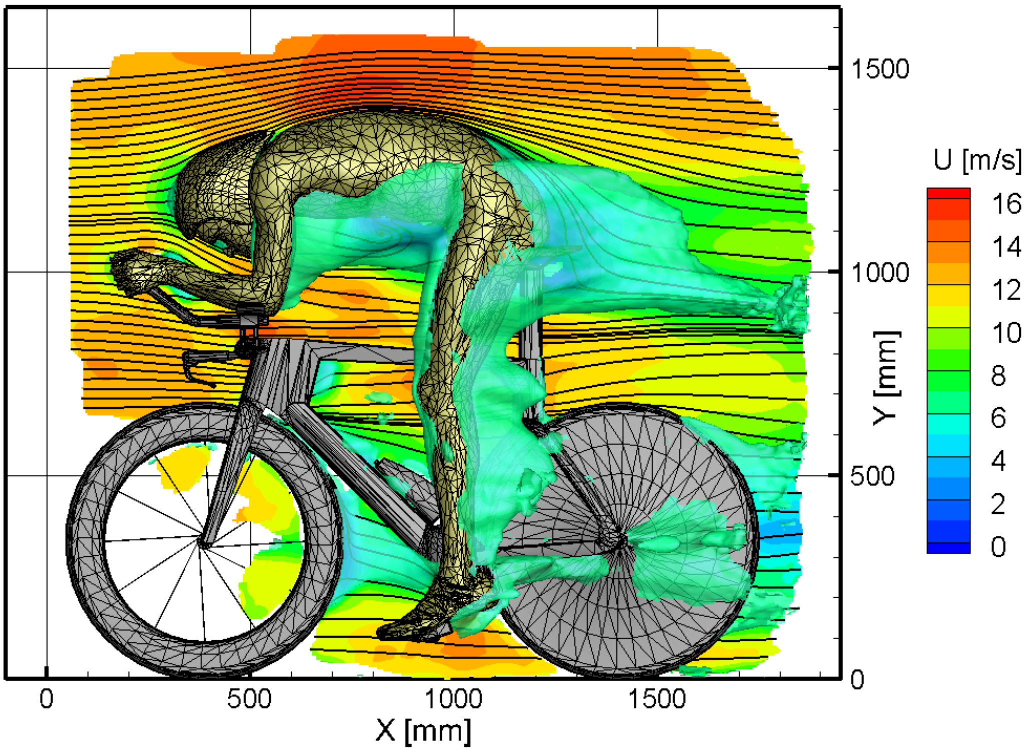

Figure 7.1: Streamwise velocity plotted in the centre plane ($z = 0$ mm) alongside surface streamlines and an iso-surface of $u = 7$ m/s. Cyclist at a freestream of $U_0 = 14$ m/s.

Some flow features can clearly be identified in the velocity contour plane in Figure 7.1. Starting furthest upstream, a distinct stagnation region is recognised at the helmet surface. A similar flow deceleration can be appreciated from the iso-surface just upstream of the stretched leg. The flow passing over the back of the cyclist instead features an acceleration induced by the curvature of the cyclist's back. The latter can also be appreciated from the reduced distance between the streamlines.

Downstream of bluff body parts, such as the upper arms, the stretched leg and the lower back, clear wake regions are identifiable. These areas of decelerated flow are visualised well by the iso-surface, but also in the centre plane the velocity deficit in the rider's wake is well captured. Likewise wake structures can be observed downstream of the front wheel stretching up to the frame's down tube as well as downstream of the rear wheel.

7.2. Streamlines

A set of randomly scattered 3D streamlines, coloured by the streamwise velocity component is displayed in Figure 7.2. The streamline illustration highlights the scale of the measurement domain and the presence of data all around the cyclist.

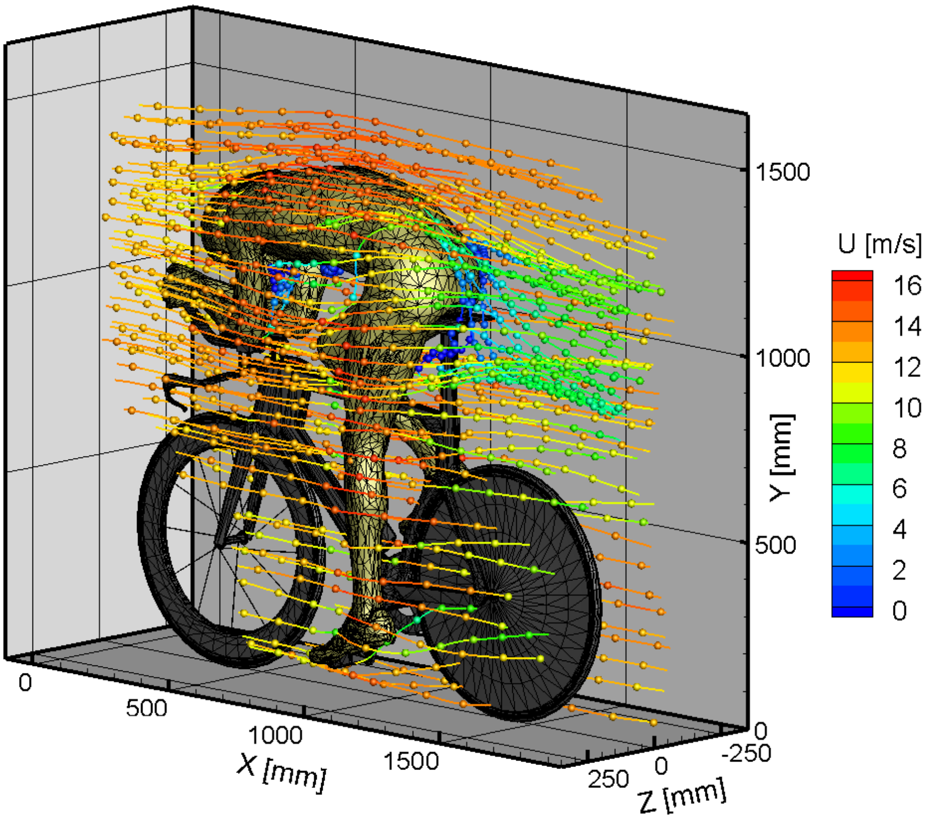

Figure 7.2: Streamline contours around the full-scale cyclist at $U_0 = 14$ m/s coloured by the streamwise velocity component u.

While the interpretation of the scattered streamline data is ambiguous to a certain extent, similar structures as discovered in the analysis in Section 7.1 are seen. These include a deceleration respectively stagnation upstream of the blunt model parts such as the helmet and the stretched leg. Likewise, the acceleration over the back is observed. The slow flow underneath the chest is seen to pass around the rider's waist with a strong upwash component. The flow just downstream of the lower back and the upper part of the stretched leg indicate a region of recirculating flow and thus, flow separation.

7.3. Friction Lines

An approximation of surface friction lines is presented in Figure 7.3. It is stressed that the velocity contour and the corresponding friction lines are evaluated on a surface offset by 5 mm to the rider's body and thus, the visualisation does not conflict with the no-slip condition.

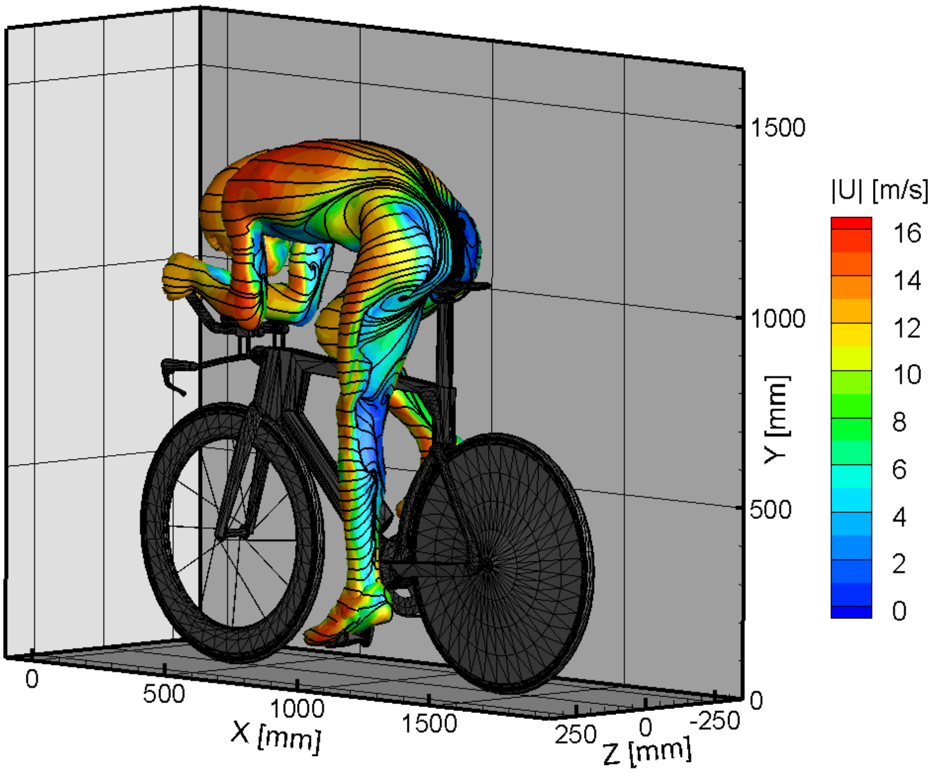

(a) Downstream view

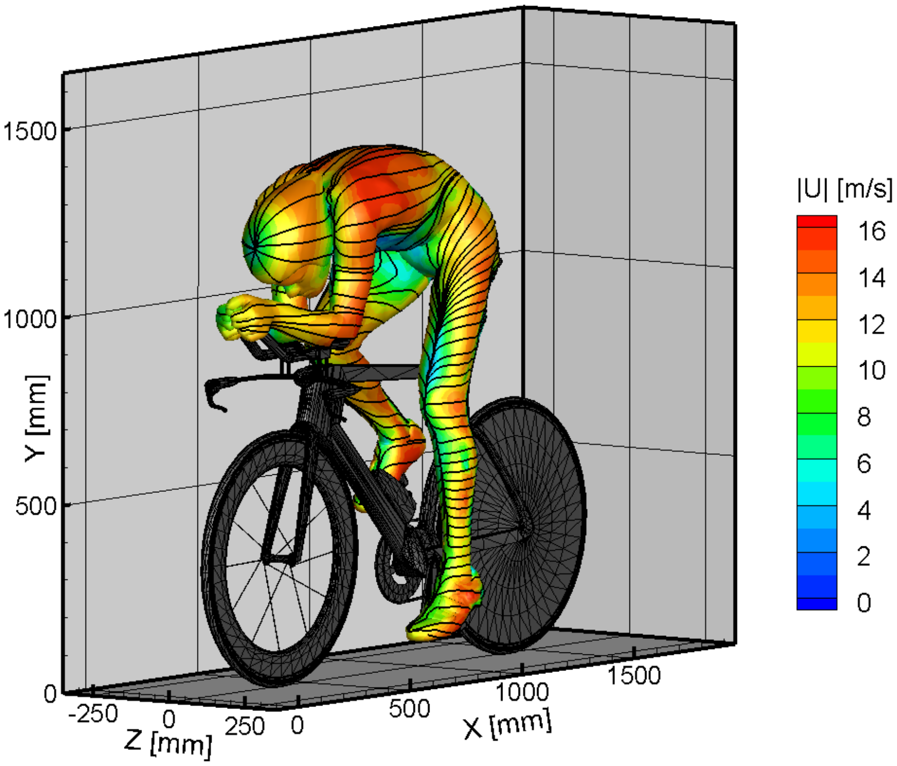

(b) Upstream view

Figure 7.3: Contour of velocity magnitude $|\vec{u}|$ at 5 mm distance to the athlete's body. Surface streamlines evaluated on the offset surface present approximation of surface friction lines.

The velocity magnitude contours are another tool that highlight flow accelerations and decelerations near the cyclist. As such, the forward and upper part of the back feature high velocities, similar to the outer faces of arms and legs. Instead on front and rear faces of the same body parts, strong velocity deficits are indicated, resulting from flow stagnation respectively separation. Comparing to the streamlines shown earlier in Figure 7.2, the flow escaping from the chest region around the rider's waist onto the lower back is seen even more clearly. The friction lines further indicate a strong inwash on the lower back.

The friction lines provide an indication of separation and reattachment lines on the body's surface. The left leg in Figure 7.3(a) is a good example for both cases. Alongside the outer side of the left thigh an abrupt change in direction of the friction lines is observed, from near horizontal to near vertical paths. The path of the latter can be interpreted as a separation line.

On the lower leg the streamlines are seen to continue much further around the shank, meaning that the flow stays attached for longer around the thinner shank and ankle. Here the near vertical streamlines on the lower calf may instead be interpreted as a reattachment line.

Figure 7.3(b) shows the friction lines viewed from upstream. A distinct stagnation point is appreciated on the helmet. Similarly, stagnation lines are visible on the upper arms and the left leg.

7.4. Vorticity Field

A visualisation of the flow topology by means of the streamwise vorticity ω_x is presented in Figure 7.4. The figure shows iso-surfaces of $\omega_x = \pm 100\,\mathrm{s}^{-1}$ alongside a contour surface of streamwise vorticity near the centre plane.

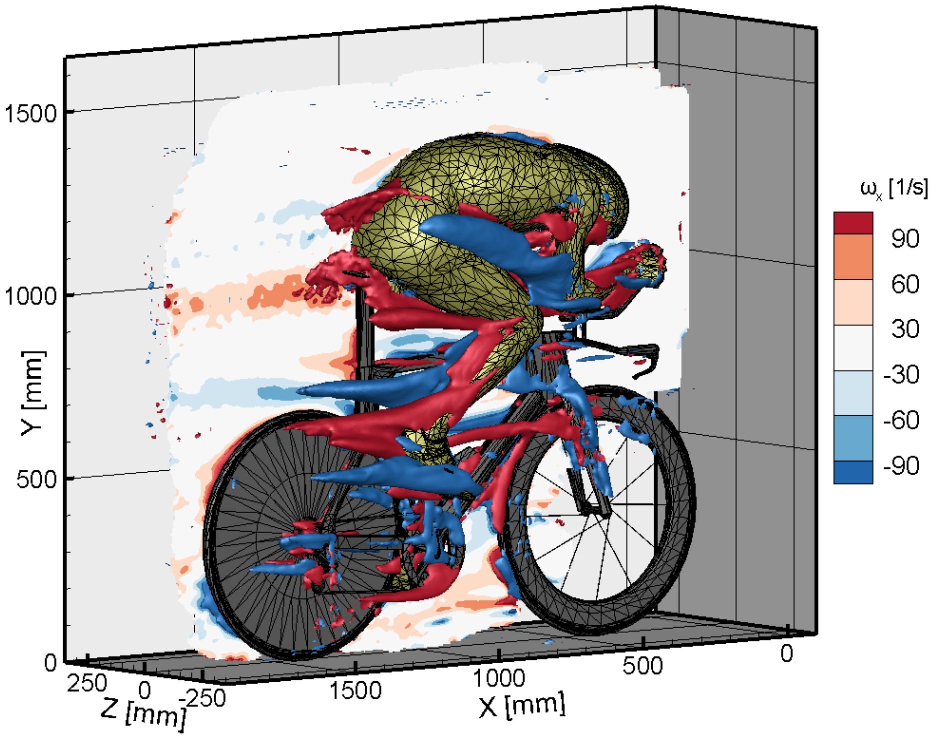

Figure 7.4: Iso-surfaces of streamwise vorticity $\omega_x = \pm 100\,\mathrm{s}^{-1}$ together with ω_x-contour at $z = 10\,\mathrm{mm}$.

Some clear vortical structures are identified in Figure 7.4. A large counter-clockwise rotating (blue) vortex is emanating from the right elbow. The vortex passes upwards alongside the right thigh towards the rider's hip. The vortex can therefore be labelled as the 'elbow/hip-vortex'.

On the inside of the thigh, the iso-surface indicates a vortical structure with positive, clockwise rotational sense.

Three distinct regions of vorticity are observed to originate from the lower leg and the foot. The lowest of these structures which is emanating from the athlete's foot is again of negative (counter-clockwise) rotational sense. A vortex of opposite rotational direction emanating from the lower shank respectively the ankle is separating the foot vortex from another blue vortex forming at the inside of the shank.

7.5. Q-Criterion

The findings from Figure 7.4 are compared to an evaluation of the Q-criterion in a local analysis on the right leg. Iso-surfaces of Q-criterion coloured by ω_x are shown in Figure 7.5.

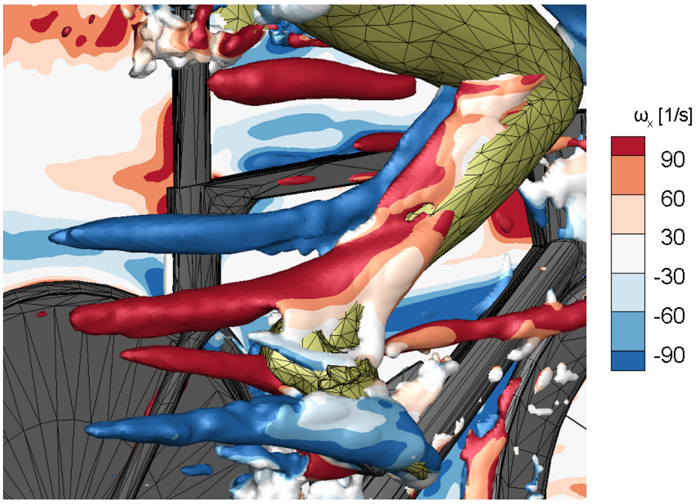

Figure 7.5: Iso-surfaces of Q-criterion coloured by ω_x on the right leg.

The analysis by the Q-criterion confirms the presence of the inner thigh vortex. Furthermore, it is seen that two counter-rotating vortex pairs emerge from the lower leg, respectively the foot. The outer blue vortex emanating from the right foot compares well with the structure identified earlier in Figure 7.4. However, Figure 7.5 suggests that there is a counter-rotating vortex emanating from the inside of the foot as well. The latter vortex follows a converging path towards the outer shank vortex which has the same rotational sense. These two vortices, which are seen to merge further downstream (see Section 7.6), separate the inner shank and the outer foot vortex.

7.6. Wake Planes

Some analysis is carried out in a plane half a torso length downstream of the rider's lower back (Figure 7.6), given that the prominent references of published research in experimental cycling aerodynamics focus on wake measurements. For the specific case the studies by Crouch et al. (2014) and Terra et al. (2016a) are found to compare well.

The velocity contour in Figure 7.6(a) visualises the asymmetry of the wake, with the left hand side of the stretched leg featuring a more pronounced velocity deficit as compared to the right hand side. The velocity vectors indicate downwash downstream of the lower back. Part of the downwash is expected to stem from the curvature of the riders back. The vorticity contours in Figure 7.6(b) indicate that the thigh vortices induce a further downwashing flow component near the centre plane.

The weak vortical structures above the thigh vortices are seen to originate as far upstream as on the rider's arms. Figure 7.4 suggests that the vortex emanating from the right elbow passes around the athlete's hip and is still visible in the plane shown in Figure 7.6(b). Below the thigh vortices, it is seen that on the right-hand-side the outer shank vortex is merged with the inner foot vortex, separating the inner shank and the outer foot vortex. On the stretched left leg, a small degree of vorticity is visible at the height of the knee. Further, two counter-rotating vortex sheets are present downstream of the left foot.

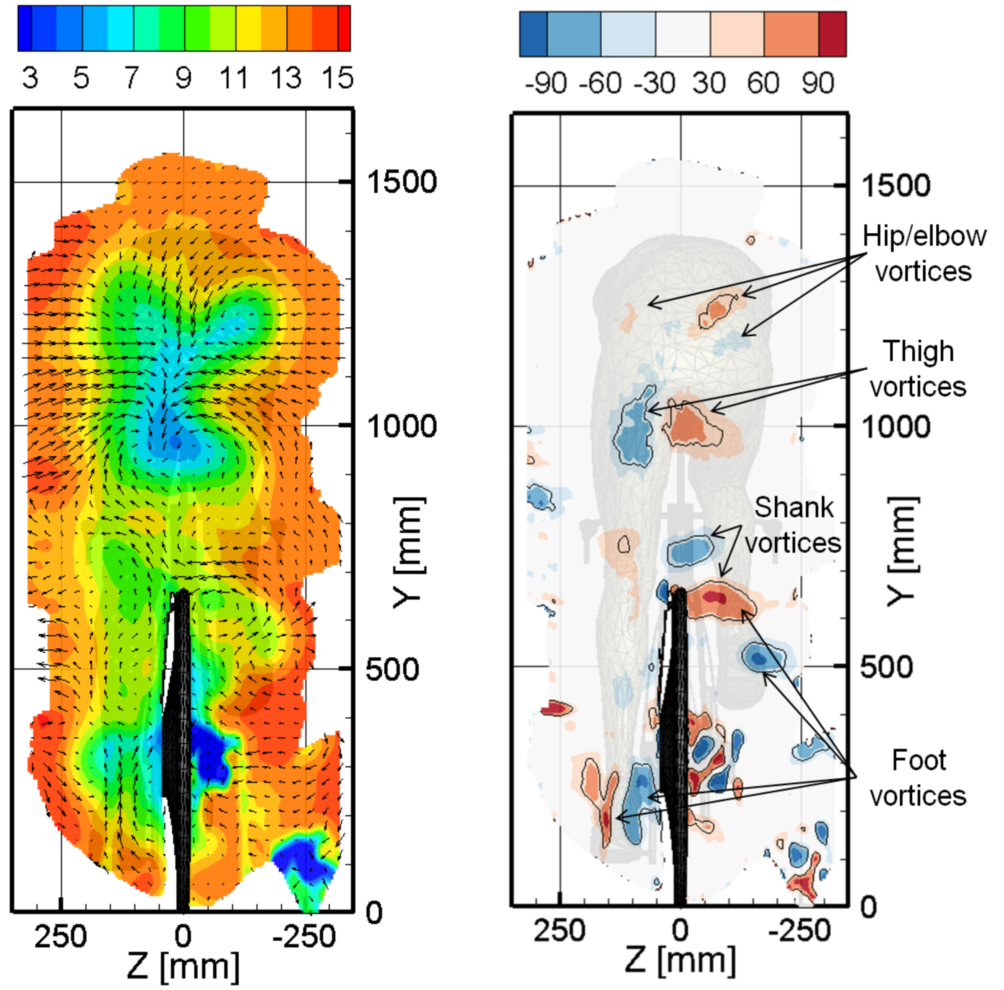

(a) Streamwise velocity contour (u [m/s]) with in-plane velocity vectors.

(b) Streamwise vorticity contour (ω_x [s^{-1}]) with iso-lines of $\omega_x = \pm 50\,\mathrm{s}^{-1}$

Figure 7.6: Streamwise velocity and vorticity contours in the cyclist's wake at $x = 1,500$ mm.

8

Conclusions and Recommendations

A novel PIV method has been proposed to increase the measurable fluid domains in volumetric PIV applications towards the cubic meter scales. The proposed robotic PIV approach leverages the advantages of a newly introduced coaxial volumetric velocimetry probe. The compactness of the measurement probe offers excellent optical access as well as outstanding handling characteristics, allowing for movement of the measurement probe without the need for re-calibration. The system's versatility is exploited by introduction of a collaborative robotic arm, yielding a robotic PIV system which can rapidly partition fluid domains of cubic meter scale into multiple adjacent sub-volume measurements.

The proposed system is studied experimentally, and its potential is demonstrated in the measurement of the near flow field around a full-scale replica of professional cyclist Tom Dumoulin. Section 8.1 draws conclusions on the conducted work, followed by recommendations for future research and development in Section 8.2. Finally, an outlook is given how the proposed system may benefit studies in wind engineering applications in the future.

8.1. Conclusions

A literature survey of industrial PIV studies suggests an apparent preference for planar and stereoscopic PIV measurements instead of a three dimensional approach. A large share of the referenced studies repeat multiple planar measurements however, either to extend the field of view in plane or to gather information in the out-of-plane direction by slicing a 3D volume, indicating that there is a wish for large-scale and full volumetric measurements. Two main reasons are identified supporting the apparent preference for multiple planar measurements in industry applications: first, the size of measurement volumes which can be realised by state-of-the-art tomographic PIV is still fairly constrained. The system complexity of a conventional tomographic PIV configuration presents a second limitation which makes its deployment in industrial facilities unlikely.

The first mentioned constrained is mitigated by the introduction of Helium Filled Soap Bubbles for wind tunnel applications. The light scattering efficient HFSB tracers enabled tomographic PIV measurements on the order of $\mathcal{O}(50\,\mathrm{l})$ (Caridi et al., 2015; Schanz et al., 2016b; Terra et al., 2016a). In applications where larger measurement domains are desired, partitioning of the domain is a viable approach. Yet, domain partitioning by tomographic PIV is extremely challenging due to the setup complexity with three or more cameras at large tomographic aperture and strict calibration requirements.

Instead compact PIV systems present superior handling characteristics. Single camera, volumetric PIV techniques developed in the past include holographic, astigmatic and plenoptic PIV. While the compactness of those techniques presents theoretically superior handling characteristics and thus, the ability to partition larger domains, the proposed methods are seen to suffer from other limitations, such as constrained optical access, high uncertainties in the depth direction or limited spatial resolution, preventing a breakthrough towards large-scale volumetric PIV measurements.

The coaxial volumetric velocimetry approach proposed in this thesis relies on the working principles of tomographic PIV as introduced by Elsinga et al. (2006). Alignment of imaging and illumination axes with four high speed cameras in a compact body at significantly lower aperture yields a versatile PIV probe that is suitable for robotic manipulation. The proposed system is thus a prime candidate for partitioning of large fluid domains, which is manifested in the thesis objective:

> *“Assess the feasibility of quantitative, industrial scale, volumetric flow measurements, by characterising a robotic PIV approach based on a compact coaxial velocimetry system in a wind tunnel environment.”*

To fulfil the research objective, the characteristics of the coaxial volumetric velocimetry approach are studied theoretically and experimentally. The alignment of imaging and illumination axes allows for measurement volumes spanning more than 0.5 m in depth and capturing beyond 20 l of fluid domain in a single measurement. The depth is limited by the particle scattering intensity which is seen to decay with the fourth order of object distance.

First wind tunnel measurements with the robotic PIV system are conducted, studying the flow around a 10 cm diameter sphere at $U_0 = 3.0$ m/s. The measurements are used to validate the developed data mapping routine to stitch acquisitions from different observation positions to a global domain. The low tomographic aperture results in a high in-depth uncertainty which is overcome by the utilisation of temporal information in the Lagrangian particle tracking algorithm ‘Shake the Box’ (Schanz et al., 2016a). It is observed that the resulting uncertainty of particle positioning in depth is highest in the imaging centre whereas it is improved along the imaging edges.

The potential of the proposed robotic PIV system is demonstrated in a full-scale PIV study on a replica of time-trialling cyclist Tom Dumoulin at 14.0 m/s. Time-resolved PIV data is acquired in 450 measurement positions, composing the time-averaged flow field around the athlete on a 2 m^3 domain. Following a simple ensemble averaging approach of the scattered particle data on $20 \times 20 \times 20$ mm^3 fluid cells yields a structured dataset with a velocity vector every 5 mm. The observed flow topology, evaluated in terms of velocity and vorticity fields, compares well to wake measurement available in literature (Crouch et al., 2014; Terra et al., 2016a). The gathered data further allows for approximation of skin friction lines, providing insight on locations of stagnation, separation and reattachment lines.

The measurement results from the large-scale demonstration experiment prove the feasibility of the desired industrial scale, volumetric flow field measurements by robotic PIV and thus, they provide a positive answer to the thesis objective. Despite the successful measurements which are considered unparalleled to the best of the author’s knowledge, potential improvements of the system can be identified which are discussed further in the following section.

8.2. Recommendations

Although the practicality of the robotic PIV system is proven, improvements in the acquisition process and the system hardware can be realised in future developments.

A limiting factor in the data acquisition is the present number of interfaces the user of the robotic PIV system is dealing with. All subsystems, namely the seeding generator, the robotic arm and the velocimetry probe, rely on individual user interfaces. Combining those in a dedicated user interface which ideally automates the read-out and storage of the probe position through the robotic arm controller is expected to significantly accelerate the acquisition period. In the presented work, two subsequent acquisitions are separated at best by two minutes. It is believed that this time can be reduced well below one minute when following the suggested system integration.

Instead of simply reducing the amount of control interfaces, more advanced acquisition procedures can be thought of. Whereas in the current campaign the probe placement is done manually in an attempt to balance the minimum amount of overlap of adjacent sub-volumes, the aerodynamic interference of probe and robotic arm and the minimisation of light reflections, smart algorithms can be imagined which automate the selection of measurement positions. This may yield coverage of a desired measurement domain with less individual measurements, while the automated placement of the probe is expected to be faster than the manual placement in any case. An intermediate step towards such a measurement approach can be a pre-programmed set of manually determine acquisition positions. These positions can then be acquired automatically by the robotic PIV system in a fast manner.

Moreover, it is believed that the calibration procedure of the CVV system prior to data acquisition can be streamlined further. In fact, all experiments presented in this thesis could have been carried out with the same camera parameters, referring to camera focus and aperture settings. If those settings are permanently fixed, the CVV probe can be operated using a universal ‘once-in-a-lifetime’ calibration. The same argumentation applies to the calibration of the robot head rotation axis with respect to the CVV probe reference frame. Assuming the camera calibration is permanent, then the robotic PIV system, namely the combination of robotic arm and CVV probe, should be operational with a universal calibration throughout its lifetime. This would present a dramatic advancement in the ease of use of the robotic PIV system when compared to a conventional tomographic PIV apparatus.

The potential of a universal calibration gives rise to the application of the volumetric PIV system by inexperienced users. This can be advantageous in industry as well as in academia, given that the user can advance quickly towards the flow analysis without requiring to study details of volumetric PIV systems, including for instance accurate volume illumination, camera alignment (potentially involving adjustment of Scheimpflug adapters) and system calibration.

Following data acquisition, smarter averaging procedures for the scattered particle data can be thought of. Whereas the simplicity and efficiency of the chosen ensemble averaging approach is well suited for the large data set presented in this thesis, other approaches as suggested by Agüera et al. (2016) for instance anticipate more accurate results and a potential enhancement of spatial resolution when applying more advanced averaging techniques.

Lastly the hardware components are addressed. Focusing on the CVV probe, it is noticed that for the presented cyclist experiment at $U_0 = 14.0$ m/s the active sensor size of the high speed cameras had to be reduced in order to guarantee a reasonable acquisition frequency for the time resolved measurements. Higher flow velocities are likely to be observed in other applications. A simple solution to the problem can be faster cameras. Alternatively, smart acquisition approaches can be imagined for instance using progressively increasing time-steps in multi-exposure images, starting with a small time separation between two exposures to evaluate a predictor for the tracer particle motion followed by a larger time separation that can be dealt with by the imaging system. The relevance of such tracking algorithms is shown in the recent work of Novara et al. (2016) which features a particle tracking algorithm based on two double-exposed PIV images.

A remaining point of attention is the aerodynamic interference of the robotic PIV system with the flow of interest. Options to reduce the interference can be a more aerodynamically shaped camera housing for instance. Alternatively, the optics can be adjusted to acquire data at a greater distance to the velcoimeter. The later approach is however likely to require a larger tomographic aperture given the increasing reconstruction uncertainty with object distance. A greater tomographic aperture inevitably yields an increased distance between individual cameras and thus, a larger probe housing. The latter can be expected to worsen the aerodynamic interference. This indicates the trade-off that has to be made here.

More recommendations can be thought of, especially if one has a specific application in mind. This may include a robotic arm with extended range for instance when considering even larger measurement domains. The recommendations presented here are instead believed to be rather universal and applicable for a wide range of applications.

8.3. Outlook: Robotic PIV in Wind Energy Applications

The relevance of particle image velocimetry across various industries, including the wind engineering field is pointed out in Section 2.2. Especially the studies referenced in Section 2.2.1 indicate that wake studies on wind turbine models are of great interest. A better understanding of the aerodynamics in a wind turbine wake provides the basis to achieve performance gains such as noise reductions or efficiency improvements to name two examples. Studying the characteristics of the wake recovery or estimations of the turbine drag by integration of the velocity deficit in the wake can be other examples thought off when applying large scale volumetric PIV to wind engineering applications.

To identify potential advantages of the proposed robotic PIV system in such applications, a selection of reference PIV studies is analysed first in Section 8.3.1. Conclusions of this survey allow for the design of a theoretical experimental campaign using the robotic PIV system introduced in this thesis as presented in Section 8.3.2. A comparison of the results from literature and the expected outcomes of the hypothetical robotic PIV study is discussed in Section 8.3.3.

8.3.1. Available PIV Studies

Three recent PIV studies on wind turbine wakes have been referenced in the literature survey in Section 2.2.1. The works of Tescione et al. (2014) and Caridi et al. (2015) focus on the analysis of a vertical axis wind turbine. The study of Tescione et al. (2014) merges a multitude of phase locked planar PIV measurements in the mid-plane (spanwise) of the H-shaped 1.0 m span and 1.0 m diameter rotor. Doing so, the time averaged velocity field in the wake plane is captured on a domain ranging from one diameter upstream to 2.2 diameters downstream of the VAWT, which spans up to 1.5 diameters in width. Additionally, measurements are conducted by stereoscopic PIV in vertical planes aligned with the free stream to capture the wake characteristics in the vertical component as well. To realise the multitude of measurements the group of Tescione et al. (2014) makes use of a two-axis traversing system which allows for automated changes in the field of view.

The study of Caridi et al. (2015) instead focuses on the tip vortex dynamics of the rotor model used by Tescione et al. (2014). For the highly three dimensional flow at the blade tips, tomographic PIV in conjunction with HFSB tracers is selected as a method of choice. The complexity of the tomographic PIV setup prevents an extension of the $40 \times 20 \times 20$ cm^3 measurement domain. The 3D measurement volume however allows for time-resolved analysis of the tip vortex.

The third study that is referenced in Section 2.2.1 employs a similar stereoscopic PIV system as described by Tescione et al. (2014). The group of Lignarolo et al. (2014) acquires velocity field measurements in the wake of a horizontal axis wind turbine of 0.6 m diameter however. Again a traversing system is used to capture the turbine wake up to 3.0 m downstream of the model with a stereoscopic PIV system in a horizontal plane through the turbine hub. Analysis is carried out on the streamwise evolution of the wake topology, including studies of instability mechanisms.

The study of Lignarolo et al. (2014) is considered as a benchmark result for the recent comparison of several numerical models attempting to simulate the turbine wake dynamics in a joint project of a TU Delft and the Technical University of Denmark amongst others (Lignarolo et al., 2016). The validation of the numerical models with experimental data is still necessary given that most industrially applied simulation codes in wind turbine applications rely on largely simplified physical models. Therefore, model parameters have to be verified ideally with respect to some experimental studies. The validation study of Lignarolo et al. (2016) focuses on the time-averaged velocity field in the wake as well as on the turbulence intensity levels in the turbine wake.

Near wake studies as presented by the groups of both, Tescione et al. (2014) and Lignarolo et al. (2014), are particularly relevant for the studies in wind farm applications, where the distance between two wind turbines may be in the range of $3.3 - 7.0$ rotor diameters (Lignarolo et al., 2016). Thus, knowledge on characteristics of the wake recovery, turbulence intensity and similar are of great interest when predicting the power production of a wind turbine farm for instance.

8.3.2. Robotic PIV in a Wind Turbine Wake Study

The robotic PIV system presented in this thesis can be utilised for studies in other applications by modifications of the measurement setup presented for the large-scale demonstration experiment in Chapters 6 and 7. In the conducted experimental campaign a fluid domain of $2.0 \times 1.6 \times 0.7$ m^3 is studied by means of robotic PIV. The measurement can be further extended by various means: one option is the selection of more base positions for the robotic arm. This approach may however be costly in terms of time. Instead, the robotic arm can be installed on a sliding traverse, significantly extending the measurement domain along the axis of the traversing system. Another simple, yet expensive solution, is the consideration of a robotic arm with a greater range.

Likewise to the setup presented in Figure 6.3 in Section 6.3, the robotic arm can be installed downstream of the wind turbine model of interest. Considering the 0.6 m diameter HAWT model of Lignarolo et al. (2014), installing the robotic arm at hub height would allow to scan the complete vertical extent of the rotor wake, given the range of selected *UR5* robot. The position of the installation can be adjusted for the purpose of the experiment of course. When interested in the development of the tip vortex structures of a VAWT model as studied by Caridi et al. (2015) for instance, the robotic PIV system may be placed lower in order to capture the blade tips well. A schematic system arrangement for measurements on a VAWT is illustrated in Figure 8.1.

A point of consideration needs to be paid to the seeding generator. In the study on the cyclist, the seeding rake is placed at the exit of the wind tunnel contraction. While this maximises the total seeded area, it can cause flow interactions and perturbations when placed close to the model. Installing the

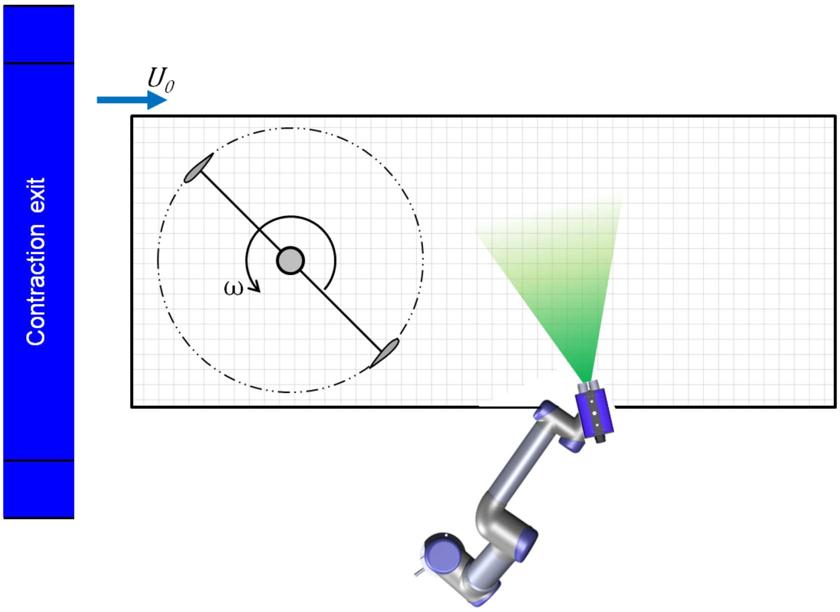

Figure 8.1: Schematic setup of the robotic PIV system for wake measurements on a vertical axis wind turbine.

system in the settling chamber instead, maximises the relative seeding concentration and it mitigates the degree of flow interaction at the measurement location. However, the total seeded area is reduced. For studies on large wind turbine models, therefore a larger seeding system or a practical traversing system for the seeder can be beneficial.

8.3.3. Anticipated Value of Robotic PIV

Applying the robotic PIV system as proposed in the previous section can add significant value to the experimental data. Figure 8.2 indicates a direct comparison of the tomographic PIV study carried out by Caridi et al. (2015) to the proposed setup using the coaxial volumetric velocimeter on a robotic arm. While the dimensions in Figure 8.2 may not be to scale, the illustration highlights how the measurement domain can easily be extended as compared to the tomographic PIV setup. The advantage of the robotic PIV apparatus is that it does not require a lengthy recalibration of the imaging system after repositioning of the probe. This way, the tip vortex path of the VAWT blade can be followed up downstream. Consequently, the measurement volume can rapidly be increased by some order of magnitude towards the cubic meter scale.

A disadvantage of the proposed method is that the adjacent sub-volume measurements are uncorrelated in time. Thus, the instantaneous velocity field is only available within the individual measurement domains, whereas the composed large-scale domain may feature time-averaged data only. Nonetheless, the singular measurement volumes are of equivalent size when compared to the indicated tomographic PIV measurement domain.

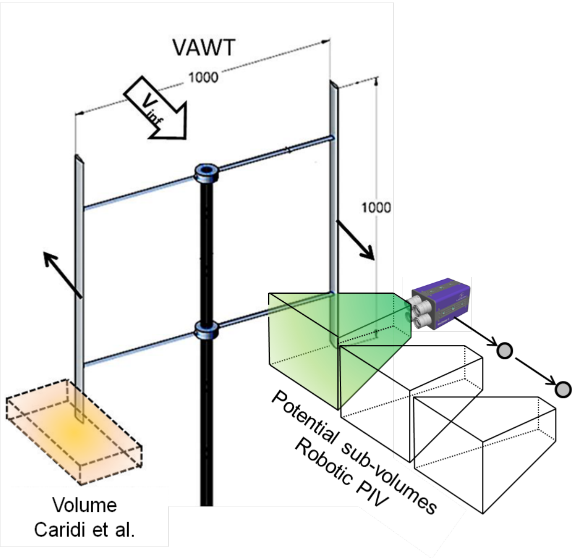

Figure 8.2: Illustration of measurement domains in a tip vortex study on a VAWT model, comparing a tomographic PIV setup as presented by Caridi et al. (2015) to the proposed robotic PIV approach. VAWT model duplicated from Caridi et al. (2015). Drawing not to scale.

The sketch provided in Figure 8.2 could easily be extended by addition of further measurement cones displaced in the vertical and/or lateral direction. Doing so, would allow for 3D3C flow field studies for instance along the turbine wake boundary. The high levels of vorticity along the wake extremities and the highly turbulent character of the wake call for volumetric measurements. Thus, it is believed that a volumetric PIV system as proposed provides better insight to the flow characteristics as compared to stereoscopic measurements. The ability to measure in a full volume further relaxes the requirements on positioning of the measurement domain with respect to the flow features of interest. If for instance the exact location of the flow feature of interest is not well defined a priori, capturing it with a planar measurement can be challenging. The coaxial velocimetry approach on the other hand features an even measurement domain which is more likely to contain a flow feature of interest. Should one still miss the desired flow structure, the probe is rapidly reoriented and therefore, it provides great flexibility during an experimental campaign.

Assuming the suggested approach is utilised to cover the full wind turbine wake by three dimensional PIV measurements, the velocity data in the wake can be used to integrate the observed velocity deficit. This way, the total turbine drag can be calculated from the PIV data. The concept of drag analysis from PIV measurements has been proven in other applications by Terra et al. (2016b).

Bibliography

Deepak Adhikari, Donald R Webster, and Jeannette Yen. Portable tomographic piv measurements of swimming shelled antarctic pteropods. *Experiments in Fluids*, 57(12):180, 2016.

Ronald J Adrian. Scattering particle characteristics and their effect on pulsed laser measurements of fluid flow: speckle velocimetry vs particle image velocimetry. *Applied optics*, 23(11):1690–1691, 1984.

Ronald J. Adrian. Image shifting technique to resolve directional ambiguity in double-pulsed velocimetry. *Appl. Opt.*, 25(21):3855–3858, Nov 1986. doi: 10.1364/AO.25.003855.

Ronald J Adrian. Particle-imaging techniques for experimental fluid mechanics. *Annual review of fluid mechanics*, 23(1):261–304, 1991.

Ronald J Adrian. Twenty years of particle image velocimetry. *Experiments in fluids*, 39(2):159–169, 2005.

Nereida Agüera, Gioacchino Cafiero, Tommaso Astarita, and Stefano Discetti. Ensemble 3d ptv for high resolution turbulent statistics. *Measurement Science and Technology*, 27(12):124011, 2016.

M Arroyo and Klaus Hinsch. Recent developments of piv towards 3d measurements. *Particle image velocimetry*, pages 127–154, 2008.

MP Arroyo and CA Greated. Stereoscopic particle image velocimetry. *Measurement science and technology*, 2(12):1181, 1991.

Callum Atkinson and Julio Soria. An efficient simultaneous reconstruction technique for tomographic particle image velocimetry. *Experiments in Fluids*, 47(4-5):553, 2009.

DB Barker and ME Fourney. Measuring fluid velocities with speckle patterns. *Optics letters*, 1(4): 135–137, 1977.

N Barry, D Burton, J Sheridan, and NAT Brown. Flow interactions between two inline cyclists. In *19 th Australian Fluid Mechanics Conference*, 2014.

Johannes Bosbach, Matthias Kühn, and Claus Wagner. Large scale particle image velocimetry with helium filled soap bubbles. *Experiments in fluids*, 46(3):539–547, 2009.

Ch Brücker. Digital-particle-image-velocimetry (dpiv) in a scanning light-sheet: 3d starting flow around a short cylinder. *Experiments in Fluids*, 19(4):255–263, 1995.

Nicolas A Buchmann, Christian E Willert, and Julio Soria. Pulsed, high-power led illumination for tomographic particle image velocimetry. *Experiments in fluids*, 53(5):1545–1560, 2012.

S Burgmann, Ch Brücker, and W Schröder. Scanning piv measurements of a laminar separation bubble. *Experiments in Fluids*, 41(2):319–326, 2006.

Davide Cardano, Giuseppe Carlino, and Antonello Cogotti. *PIV in the Car Industry: State-of-the-Artand Future Perspectives*, pages 363–376. Springer Berlin Heidelberg, Berlin, Heidelberg, 2008. ISBN 978-3-540-73528-1. doi: 10.1007/978-3-540-73528-1_19.

Giuseppe Carlo Alp Caridi, Daniele Ragni, Andrea Sciacchitano, and Fulvio Scarano. A seeding system for large-scale tomographic piv in aerodynamics. In *11th international symposium on particle image velocimetry, Santa Barbara, USA*, pages 14–16, 2015.

M. Casper, C. Lemke, and U. Dierksheide. Piv in large wind tunnel by hfsb and stb, November 2016. URL `https://www.researchgate.net/profile/Uwe_Dierksheide/project/large-scale-particle-image-velocimetry/attachment/58383d5d08aef5af880027a2/AS:432304083476480@1480080733308/download/HFSB+in+large+windtunnel+2016-11.pdf?context=projectDetails`. Accessed on: 30.03.2017.

Vincent Chabroux, Marcellin Nsi Mba, Patrick Sainton, and Daniel Favier. Wake characteristics of time trial helmets using piv-3c technique. In *15th Int. Symp. on Applications of Laser Techniques to Fluid Mechanics, Lisbon, Portugal*, volume 58, 2010.

Leonardo P Chamorro, Daniel R Troolin, Seung-Jae Lee, REA Arndt, and Fotis Sotiropoulos. Three-dimensional flow visualization in the wake of a miniature axial-flow hydrokinetic turbine. *Experiments in fluids*, 54(2):1459, 2013.

Eric Coustols, Laurent Jacquin, Frederic Moëns, and Pascal Molton. Status of onera research on wake vortex in the framework of national activities and european collaboration. *Tiré à part- Office national d'études et de recherches aerospatiales*, 2004.

TN Crouch, D Burton, NAT Brown, MC Thompson, and J Sheridan. Flow topology in the wake of a cyclist and its effect on aerodynamic drag. *Journal of Fluid Mechanics*, 748:5–35, 2014.

Aerospace Engineering Delft University of Technology. Open jet facility (hsl), 2017. URL `https://www.tudelft.nl/en/ae/organisation/departments/aerodynamics-wind-energy-flight-performance-and-propulsion/facilities/open-jet-facility/`. Accessed on: 23.03.2017.

Sports Engineering Institute Delft University of Technology. A 3d printed mannequin of tom dumoulin in the tu delft wind tunnel helps gain a competitive advantage, July 2016. URL `https://www.tudelft.nl/en/2016/tu-delft/a-3d-printed-mannequin-of-tom-dumoulin-in-the-tu-delft-wind-tunnel-helps-gain-a-competitive-advantage/`. Accessed on 24.03.2017.

TD Dudderar and PG Simpkins. Laser speckle photography in a fluid medium. *Nature*, 270(5632): 45–47, 1977.

Gerrit E Elsinga, Fulvio Scarano, Bernhard Wieneke, and Bas W van Oudheusden. Tomographic particle image velocimetry. *Experiments in fluids*, 41(6):933–947, 2006.

Timothy W Fahringer, Kyle P Lynch, and Brian S Thurow. Volumetric particle image velocimetry with a single plenoptic camera. *Measurement Science and Technology*, 26(11):115201, 2015.

Jean-Marc Foucaut and Michel Stanislas. Some considerations on the accuracy and frequency response of some derivative filters applied to particle image velocimetry vector fields. *Measurement Science and Technology*, 13(7):1058, 2002.

R Grousson and S Mallick. Study of flow pattern in a fluid by scattered laser light. *Applied Optics*, 16 (9):2334–2336, 1977.

Rainer Hain, Christian J. Kähler, and Rolf Radespiel. *Principles of a Volumetric Velocity Measurement Technique Based on Optical Aberrations*, pages 1–10. Springer Berlin Heidelberg, Berlin, Heidelberg, 2009. ISBN 978-3-642-01106-1. doi: 10.1007/978-3-642-01106-1_1. URL `http://dx.doi.org/10.1007/978-3-642-01106-1_1`.

Gabor T Herman and Arnold Lent. Iterative reconstruction algorithms. *Computers in biology and medicine*, 6(4):273–294, 1976.

David Hill, Daniel Troolin, Geoffrey Walters, Wing Lai, and Kendra Sharp. Volumetric 3-component velocimetry (v3v) measurements of the turbulent flow in stirred tank reactors. In *Proceedings of the 14th international symposium on applications of laser techniques to fluid mechanics. Lisbon, Portugal*, 2008.

Klaus D Hinsch. Holographic particle image velocimetry. *Measurement Science and Technology*, 13 (7):R61, 2002.

Klaus Hoyer, Markus Holzner, Beat Lüthi, Michele Guala, Alexander Liberzon, and Wolfgang Kinzelbach. 3d scanning particle tracking velocimetry. *Experiments in Fluids*, 39(5):923, 2005.

Intelligent Laser Applications GmbH. Piv - traversing systems - traverse units, 2017. URL `https://www.ila.de/piv/traversing-systems0.html`. Accessed on: 11.04.2017.

Luther N Jenkins, Chung-Sheng Yao, Scott M Bartram, Jerome Harris, Brian Allan, Oliver Wong, and W Derry Mace. Development of a large field-of-view piv system for rotorcraft testing in the 14-x 22-foot subsonic tunnel. May 2009.

Jinhee Jeong and Fazle Hussain. On the identification of a vortex. *Journal of fluid mechanics*, 285: 69–94, 1995.

Roderick R La Foy and Pavlos Vlachos. Multi-camera plenoptic particle image velocimetry. In *PIV13; 10th International Symposium on Particle Image Velocimetry, Delft, The Netherlands, July 1-3, 2013*. Delft University of Technology, Faculty of Mechanical, Maritime and Materials Engineering, and Faculty of Aerospace Engineering, 2013.

LaVision GmbH. Flowmaster shake-the-box (4d-ptv), product-manual, November 2016. Document name: 1010175_FlowMaster_Shake-the-Box_D83.pdf.

L.E.M. Lignarolo, D. Ragni, C. Krishnaswami, Q. Chen, C.J. Simão Ferreira, and G.J.W. van Bussel. Experimental analysis of the wake of a horizontal-axis wind-turbine model. *Renewable Energy*, 70: 31 – 46, 2014. ISSN 0960-1481. doi: http://dx.doi.org/10.1016/j.renene.2014.01.020. URL `http://www.sciencedirect.com/science/article/pii/S0960148114000494`. Special issue on aerodynamics of offshore wind energy systems and wakes.

Lorenzo EM Lignarolo, Dhruv Mehta, Richard JAM Stevens, Ali Emre Yilmaz, Gijs van Kuik, Søren J Andersen, Charles Meneveau, Carlos J Ferreira, Daniele Ragni, Johan Meyers, et al. Validation of four les and a vortex model against stereo-piv measurements in the near wake of an actuator disc and a wind turbine. *Renewable energy*, 94:510–523, 2016.

Kyle Lynch and Fulvio Scarano. A high-order time-accurate interrogation method for time-resolved piv. *Measurement Science and Technology*, 24(3):035305, 2013.

Craig J Mead, Christopher Wrighton, and Kevin Britchford. An experimental study of coaxial jets using acoustic piv and lda methods (cojen). In *21st AIAA/CEAS Aeroacoustics Conference*, page 3122, 2015.

A Melling. Tracer particles and seeding for particle image velocimetry. *Measurement Science and Technology*, 8(12):1406–1416, 1997.

M.A. Mendez, M. Raiola, A. Masullo, S. Discetti, A. Ianiro, R. Theunissen, and J.-M. Buchlin. Pod-based background removal for particle image velocimetry. *Experimental Thermal and Fluid Science*, 80:181 – 192, 2017. ISSN 0894-1777. doi: http://dx.doi.org/10.1016/j.expthermflusci.2016.08.021. URL `http://www.sciencedirect.com/science/article/pii/S0894177716302266`.

Hui Meng, Gang Pan, Ye Pu, and Scott H Woodward. Holographic particle image velocimetry: from film to digital recording. *Measurement Science and Technology*, 15(4):673, 2004.

Roland Meynart. Instantaneous velocity field measurements in unsteady gas flow by speckle velocimetry. *Applied Optics*, 22(4):535–540, 1983.

D Michaelis, M Novara, F Scarano, and B Wieneke. Comparison of volume reconstruction techniques at different particle densities. In *15th international symposium on applications of laser techniques to fluid mechanics*, pages 3–17, 2010.

Masaki Nakagawa, Frank Michaux, Stephan Kallweit, and Kazuhiro Maeda. Unsteady flow measurements in the wake behind a wind-tunnel car model by using high-speed planar piv. September 2015.

Matteo Novara, Kees Joost Batenburg, and Fulvio Scarano. Motion tracking-enhanced mart for tomographic piv. *Measurement science and technology*, 21(3):035401, 2010.

Matteo Novara, Daniel Schanz, Nico Reuther, Christian J Kähler, and Andreas Schröder. Lagrangian 3d particle tracking in high-speed flows: Shake-the-box for multi-pulse systems. *Experiments in Fluids*, 57(8):128, 2016.

M. G. Olsen and R. J. Adrian. Out-of-focus effects on particle image visibility and correlation in microscopic particle image velocimetry. *Experiments in Fluids*, 29:S166–S174, 2000. doi: `10.1007/s003480070018`.

K Pengel, JW Kooi, M Raffel, C Willert, and J Kompenhans. Application of piv in the large low speed facility of dnw. In *New Results in Numerical and Experimental Fluid Mechanics*, pages 253–258. Springer, 1997.

Markus Raffel, Hugues Richard, Klaus Ehrenfried, B Van der Wall, C Burley, P Beaumier, K McAlister, and Kurt Pengel. Recording and evaluation methods of piv investigations on a helicopter rotor model. *Experiments in Fluids*, 36(1):146–156, 2004.

Markus Raffel, Christian E. Willert, and Jürgen Wereley, Steven ans Kompenhans. *Particle Image Velocimetry - A Practical Guide*. Springer Science & Business Media, Berlin Heidelberg, second edition, 2007. ISBN 978-3-540-72308-0.

R&D Magazine. 2008 r & d 100 award winners, 2010. URL `https://www.rdmag.com/article/2010/07/2008-r-d-100-award-winners`. Accessed on: 25.06.2017.

Alberto F Rius Vidales. Air-wake flow dynamics on a simplified frigate shape: An experimental study by large-scale tomographic ptv. 2016.

Abraham Savitzky and Marcel JE Golay. Smoothing and differentiation of data by simplified least squares procedures. *Analytical chemistry*, 36(8):1627–1639, 1964.

F Scarano. Tomographic piv: principles and practice. *Measurement Science and Technology*, 24, 2013a. doi: `10.1088/0957-0233/24/1/012001`.

Fulvio Scarano. *Experimental Aerodynamics*. Delft University of Technology, 1 edition, 2013b. Course reader, Flow Measurement Techniques (AE4-180).

Fulvio Scarano, Sina Ghaemi, Giuseppe Carlo Alp Caridi, Johannes Bosbach, Uwe Dierksheide, and Andrea Sciacchitano. On the use of helium-filled soap bubbles for large-scale tomographic piv in wind tunnel experiments. *Experiments in Fluids*, 56(2):42, 2015. ISSN 1432-1114. doi: `10.1007/s00348-015-1909-7`. URL `http://dx.doi.org/10.1007/s00348-015-1909-7`.

Daniel Schanz, Sebastian Gesemann, Andreas Schröder, Bernhard Wieneke, and Matteo Novara. Non-uniform optical transfer functions in particle imaging: calibration and application to tomographic reconstruction. *Measurement Science and Technology*, 24(2):024009, 2012.

Daniel Schanz, Sebastian Gesemann, and Andreas Schröder. Shake-the-box: Lagrangian particle tracking at high particle image densities. *Experiments in fluids*, 57(5):1–27, 2016a.

Daniel Schanz, Florian Huhn, Sebastian Gesemann, Uwe Dierksheide, Remko van de Meerendonk, Peter Manovski, and Andreas Schröder. Towards high-resolution 3d flow field measurements at the cubic meter scale. July 2016b.

Andrea Sciacchitano and Fulvio Scarano. Elimination of piv light reflections via a temporal high pass filter. *Measurement Science and Technology*, 25(8):084009, 2014.

Steven M Soloff, Ronald J Adrian, and Zi-Chao Liu. Distortion compensation for generalized stereoscopic particle image velocimetry. *Measurement science and technology*, 8(12):1441, 1997.

Christoph Strangfeld, Dirk Wieser, Hanns-Joachim Schmidt, Rene Woszidlo, Christian Nayeri, and Christian Paschereit. Experimental study of baseline flow characteristics for the realistic car model drivaer. Technical report, SAE Technical Paper, 2013.

W. Terra, A. Sciacchitano, and F. Scarano. Evaluation of aerodynamic drag of a full-scale cyclist model by large-scale tomographic-piv. 2016a.

W Terra, A Sciacchitano, and F Scarano. Drag analysis from piv data in speed sports. *Procedia Engineering*, 147:50–55, 2016b.

G Tescione, D Ragni, C He, CJ Simão Ferreira, and GJW Van Bussel. Near wake flow analysis of a vertical axis wind turbine by stereoscopic particle image velocimetry. *Renewable Energy*, 70:47–61, 2014.

Brian S Thurow and Timothy Fahringer. Recent development of volumetric piv with a plenoptic camera. In *PIV13; 10th International Symposium on Particle Image Velocimetry, Delft, The Netherlands, July 1-3, 2013*. Delft University of Technology, Faculty of Mechanical, Maritime and Materials Engineering, and Faculty of Aerospace Engineering, 2013.

Toyota Motorsport GmbH. Toyota motorsport wind tunnel helps automotive engineers design faster high-performance cars with sophisticated built-in piv system, 2017. URL `https://www.toyota-motorsport.com/media/tmg/Tecplot_PIV.pdf`. Accessed on: 27.04.2017.

HM Tritico, AJ Cotel, and JN Clarke. Development, testing and demonstration of a portable submersible miniature particle imaging velocimetry device. *Measurement Science and Technology*, 18(8):2555, 2007.

Daniel R Troolin and Ellen K Longmire. Volumetric velocity measurements of vortex rings from inclined exits. *Experiments in fluids*, 48(3):409–420, 2010.

TSI Incorporated. The extensive capabilities of instantaneous truly volumetric velocimetry, 2012. URL `http://www.tsi.com/uploadedFiles/_Site_Root/Products/Literature/Brochures/V3V_5001281_RevB_Brochure.pdf`. Accessed on: 14.06.2017.

A/S Universal Robots. Technical specifications - ur5, 2017. URL `https://www.universal-robots.com/media/1514597/101081_199901_ur5_technical_details_web_a4_art03_rls_eng.pdf`. Accessed on 27.03.2017.

V Wendt and M Fürll. Flow field measurements around a car using particle image velocimetry. In *4 th International Symposium on Particle Image Velocimetry(PIV'01)*, pages 1–6, 2001.

Jerry Westerweel. Analysis of piv interrogation with low-pixel resolution. In *SPIE's 1993 International Symposium on Optics, Imaging, and Instrumentation*, pages 624–635. International Society for Optics and Photonics, 1993.

Jerry Westerweel and Fulvio Scarano. Universal outlier detection for piv data. *Experiments in fluids*, 39(6):1096–1100, 2005.

B Wieneke. Volume self-calibration for 3d particle image velocimetry. *Experiments in fluids*, 45(4): 549–556, 2008.

Bernhard Wieneke. Iterative reconstruction of volumetric particle distribution. *Measurement Science and Technology*, 24(2):024008, 2012.

Christian E Willert and Morteza Gharib. Digital particle image velocimetry. *Experiments in fluids*, 10(4): 181–193, 1991.

NA Worth and TB Nickels. Acceleration of tomo-piv by estimating the initial volume intensity distribution. *Experiments in Fluids*, 45(5):847, 2008.


TU Delft